

AD609492

AFFDL-TR-64-163

MONITORING OF ROCKET ENGINE
PERFORMANCE BY SPECTROSCOPIC TECHNIQUES

TECHNICAL REPORT NO. AFFDL-TR-64-163

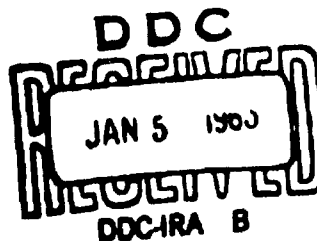
Robert F. Strauss
Astrosystems International, Inc.

October 1964

| | |
|-------------|---------|
| COPY 2 OF 3 | HR |
| HARD COPY | \$ 4.00 |
| MICROFICHE | \$ 1.00 |

Air Force Flight Dynamics Laboratory
Research and Technology Division
Air Force Systems Command
Wright-Patterson Air Force Base, Ohio

148 P



ARCHIVE COPY

Best Available Copy

NOTICES

When Government drawings, specifications, or other data are used for any purpose other than in connection with a definitely related Government procurement operation, the United States Government thereby incurs no responsibility nor any obligation whatsoever; and the fact that the Government may have formulated, furnished, or in any way supplied the said drawings, specifications, or other data, is not to be regarded by implication or otherwise as in any manner licensing the holder or any other person or corporation, or conveying any rights or permission to manufacture, use, or sell any patented invention that may in any way be related thereto.

Qualified requesters may obtain copies of this report from the Defense Documentation Center (DDC), (formerly ASTIA), Cameron Station, Bldg. 5, 5010 Duke Street, Alexandria, Virginia, 22314.

This report has been released to the Office of Technical Services, U. S. Department of Commerce, Washington 25, D. C., for sale to the general public.

Copies of this report should not be returned to the Research and Technology Division, Wright-Patterson Air Force Base, Ohio, unless return is required by security considerations, contractual obligations, or notice on a specific document.

AFFDL-TR-64-163

**MONITORING OF ROCKET ENGINE
PERFORMANCE BY SPECTROSCOPIC TECHNIQUES**

TECHNICAL REPORT NO. AFFDL-TR-64-163

**Robert P. Strauss
Astrosystems International, Inc.**

October 1964

**Air Force Flight Dynamics Laboratory
Research and Technology Division
Air Force Systems Command
Wright-Patterson Air Force Base, Ohio**

FOREWORD

This report was prepared for the Air Force Flight Dynamics Laboratory of the Research and Technology Division, Air Force Systems Command, Wright-Patterson Air Force Base, Ohio by Astrosystems International, Inc., Fairfield, New Jersey under Contract No. AF 33(615)-1614; Project 8224, "Propulsion and Auxiliary Systems Instrumentation for Flight Control Purposes"; Task 822405, "Propulsion Parameter Measurement Technology". The work was administered by the Flight Dynamics Laboratory; Mr. D. A. Shumway was Project Engineer. The manuscript was released by the author 10 October 1964 for publication as an R & D Technical Report.

These studies were made by the Research Division of Astrosystems International, Inc. under the direction of Robert F. Strauss, Director. The major contributors to this study and their fields of competency were:

| | |
|-----------------|--------------------|
| John Gordon | - Thermochemistry |
| Marvin Hauptman | - Spectroscopy |
| Charles Sage | - Systems Analysis |
| Allen Schwalb | - Gas Dynamics |

This report summarizes all work conducted during the period 10 April to 10 August 1964. The contractor's report number is TR 64001F.

ABSTRACT


An analytical investigation was conducted to study the emission spectra of the exhaust stream of selected rocket engine liquid propellant combinations to determine the feasibility of detecting exhaust species spectra as a measure of various propulsion system characteristics.

The propellants selected for analysis were oxygen/hydrogen, oxygen/ RF-1 and nitrogen tetroxide/unsymmetrical dimethylhydrazine as being most representative. A rocket engine for test was designed having a chamber pressure of 50-100 psia and a flow rate of 0.1 gm/sec. Calculations of signal strength with mixture ratio were made and the species OH, NH, CO and NO found to be of most interest.

It was determined that mixture ratio variations and flow rate variations could be separately detected. A system for detecting incipient burnout by monitoring metallic oxide emissions and instability by intensity frequency pattern variations was presented. A flight weight system was shown to be feasible.

Recommendations were made to conduct an experimental program using N_2O_4 /UDMH propellants to study the variation of the OH, CH, CHO, CN, C_2 , H_2O and CO_2 species with mixture ratio at constant flow and with total flow at constant mixture ratio. Burnout and instability tests were also recommended as well as a prototype detector design based upon the recommended experimental studies.

This technical report has been reviewed and is approved.


W. A. SLOAN, JR.
Colonel, USAF

Chief, Flight Control Division

TABLE OF CONTENTS

| | PAGE |
|---|------|
| 1. Introduction | 1 |
| 2. Propellants Analysis | 3 |
| 3. Signal Analysis | 19 |
| 4. Rocket Engine Analysis | 35 |
| 5. Mixture Ratio Analysis | 73 |
| 6. Exit Plane Gas Temperature Analysis | 100 |
| 7. Malfunction Monitoring | 110 |
| 8. Flight System Analysis | 118 |
| 9. Conclusions and Recommendations | 122 |
| References | 124 |
| Bibliography | 126 |
| Appendix A Sample Calculation from Thermochemical Program | 129 |
| Appendix B Computer Programs for UV and IR Radiance Calculations. | 132 |
| Appendix C Past and Current Radiation Simulation Programs at Astrosystems | 137 |

ILLUSTRATIONS

| FIGURE | | PAGE |
|--------|---|------|
| 1. | O ₂ /H ₂ (Frozen Flow - 60 psia - P _c) Mole Fraction of Exhaust Gases vs Mixture Ratio | 10 |
| 2. | Oxygen/RP-1 (Frozen Flow - 50 psia - P _c) Mole Fraction of Exhaust Gases vs Mixture Ratio | 11 |
| 3. | N ₂ O ₄ /UDMH (Frozen Flow, 60 psia - P _c) Mole Fraction of Exhaust Gases vs Mixture Ratio | 12 |
| 4. | Oxygen-Hydrogen Exhaust Gas Temperature as a Function of Expansion Ratio and Mixture Ratio | 13 |
| 5. | Oxygen - RP-1 Exhaust Gas Temperature as a Function of Expansion Ratio and Mixture Ratio | 14 |
| 6. | N ₂ O ₄ - UDMH Exhaust Gas Temperature as a Function of Expansion Ratio and Mixture Ratio | 15 |
| 7. | View of Dynamic Vacuum Facility No. 2 | 35a |
| 8. | View of Dynamic Vacuum Facility No. 2 | 35a |
| 9. | Dynamic Vacuum Facility - Front Elevation | 36 |
| 10. | Dynamic Vacuum Facility - Side View | 37 |
| 11. | Dynamic Vacuum Facility - Plan View | 38 |
| 12. | Rocket Engine Exhaust Gas Temperature vs Diffusion Pump Inlets Static Gas Temperature (After Cooling) | 42 |
| 13. | Vapor Pressure of Some Exhaust Gas Constituents vs Temperature | 43 |
| 14. | Oxygen-Hydrogen Gas Load on Vacuum System as a Function of Expansion Ratio and Mixture Ratio | 46 |
| 15. | Oxygen - RP-1 Gas Load on Vacuum System as a Function of Expansion Ratio and Mixture Ratio | 51 |
| 16. | N ₂ O ₄ - UDMH Gas Load on Vacuum System as a Function of Expansion Ratio and Mixture Ratio | 52 |
| 17. | Capacity of Astrosystems' Large Dynamic Vacuum Facility . . . | 54 |
| 18. | Schematic Rocket Engine - Vacuum System | 61 |
| 19. | Research Rocket Engine (Axial Premixer) | 62 |

ILLUSTRATIONS (continued)

| FIGURE | | PAGE |
|--------|--|------|
| 20. | Initial Plume Boundary Angle for Titan II Missile vs Altitude | 69 |
| 21. | Sonic Nozzle Convergence Half Angle Required to Simulate Initial Plume Boundary Angle vs Altitude | 70 |
| 22. | Radius of Jet Boundary for $\gamma=1.4$ | 72 |
| 23. | Theoretical Intensity of CH 4315.3Å vs Mixture Ratio for $N_2O_4/UDMH$ | 74 |
| 24. | Theoretical Intensity of CH 3889.2Å vs Mixture Ratio for $N_2O_4/UDMH$ | 75 |
| 25. | Theoretical Intensity of CH 3145.4Å vs Mixture Ratio for $N_2O_4/UDMH$ | 76 |
| 26. | Theoretical Intensity of NH 3358.8Å vs Mixture Ratio for $N_2O_4/UDMH$ | 78 |
| 27. | Theoretical Intensity of CO Bands vs Mixture Ratio for $N_2O_4/UDMH$ | 79 |
| 28. | Theoretical Intensity of CHO Bands vs Mixture Ratio for $N_2O_4/UDMH$ | 80 |
| 29. | Theoretical Intensity of CN Bands vs Mixture Ratio for $N_2O_4/UDMH$ | 81 |
| 30. | Theoretical Intensity of NO Bands vs Mixture Ratio for $N_2O_4/UDMH$ | 82 |
| 31. | Theoretical Blackbody Radiant Intensity of OH Bands vs Mixture Ratio for $N_2O_4/UDMH$ | 84 |
| 32. | Theoretical Intensity of OH Bands vs Mixture Ratio for $N_2O_4/UDMH$ | 85 |
| 33. | O_2/FP Plume Radiant Intensity at 2811Å vs Mixture Ratio (215,000 ft Altitude) | 87 |
| 34. | O_2/FP Plume Radiant Intensity at 1000-5000Å vs Mixture Ratio (110,000 ft Altitude) | 88 |
| 35. | O_2/NH_3 Plume Radiant Intensity Compilation (2811Å Band) vs Mixture Ratio at Three Altitudes | 89 |

ILLUSTRATIONS (continued)

| FIGURE | | PAGE |
|--------|---|------|
| 36. | Absolute Intensity of 3100\AA OH vs O/F Ratio for Three Altitudes | 90 |
| 37. | Absolute Intensity of 4300\AA CH vs O/F Ratio for Three Altitudes | 91 |
| 38. | Absolute Intensity of 4700\AA C ₂ vs O/F Ratio for Three Altitudes | 92 |
| 39. | O ₂ /H ₂ Plume Radiant Intensity (3075\AA) vs Mixture Ratio (Altitude - 30,000 ft) | 93 |
| 40. | O ₂ /H ₂ Plume Radiant Intensity (3075\AA) vs Mixture Ratio (Altitude 80,000 ft) | 94 |
| 41. | O ₂ /H ₂ Plume Radiant Intensity (3075\AA) vs Mixture Ratio (Altitude 136,000 ft) | 95 |
| 42. | Comparison of O ₂ /NH ₃ and O ₂ /RP Plume Radiant Intensity (7811\AA vs Mixture Ratio at 215,000 ft Altitude | 96 |
| 43. | Oxygen-Hydrogen Exhaust Gas Temp. as a Function of Mixture Ratio for an Expansion Ratio of $\epsilon=40$, $P_c=60$ psia | 101 |
| 44. | Oxygen - RP-1 Exhaust Gas Temperature as a Function of Mixture Ratio for an Expansion Ratio of $\epsilon=40$, $P_c=50$ psia | 102 |
| 45. | N ₂ O ₄ -UDMH Exhaust Gas Temperature as a Function of Mixture Ratio for an Expansion Ratio of $\epsilon=40$, $P_c=60$ psia | 103 |
| 46. | Mixture Ratio vs Flow Rate | 107 |
| 47. | Mixture Ratio vs Flow Rate | 108 |
| 48. | Mixture Ratio vs Flow Rate | 109 |
| 49. | Rocket Engine Flow rate and Chamber Pressure vs Nozzle Reynolds Number | 111 |
| 50. | Chamber, Rocket Engine (Gas/Gas) | 115 |
| 51. | Schematic Arrangement of a No. 5652 Phototube and Selective Filters | 119 |
| 52. | Typical Response of Phototube Cathodes and Selective Filters. | 120 |

TABLES

| TABLE | PAGE |
|---|------|
| 1. Theoretical Performance of Oxygen/Hydrogen | 5 |
| 2. Theoretical Performance of Oxygen/RP-1 | 6 |
| 3. Theoretical Performance of N_2O_4 /UDMH | 9 |
| 4. Emission Known to Arise from Combustion (Persistent Band Heads Only) | 16 |
| 5. Absorption Spectra of Combustion Species (Primarily Persistent Band Heads) | 18 |
| 6. UV-Visible Primary Radiation Intensity at the Mach Cone. | 28 |
| 7. UV-Visible Secondary Radiation Intensity at the Mach Cone. | 29 |
| 8. IR Radiation Intensity at the Mach Cone. | 30 |
| 8A. Oxygen-Hydrogen Gas Load on Vacuum Systems as a Function of Mixture Ratio and Expansion Ratio | 44 |
| 9. Oxygen-RP-1 Gas Load on Vacuum Systems as a Function of Mixture Ratio and Expansion Ratio | 47 |
| 10. N_2O_4 -UDMH Gas Load on Vacuum Systems as a Function of Mixture Ratio and Expansion Ratio. | 49 |
| 11. Capability of Vacuum System for Oxygen-Hydrogen Gas as a Function of Mixture Ratio and Expansion Ratio | 55 |
| 12. Capability of Vacuum System for Oxygen-RP-1 Gas as a Function of Mixture Ratio and Expansion Ratio | 56 |
| 13. Capability of Vacuum System for N_2O_4 -UDMH Gas as a Function of Mixture Ratio and Expansion Ratio | 57 |
| 14. Signal-to-Noise Ratio, UV-Visible Region | 59 |
| 15. Summary of Nozzle and Plume Parameters for the Sonic Nozzle. | 65 |
| 16. Summary of N_2O_4 /UDMH Species Radiant Intensities vs Mixture Ratio | 86 |
| 17. Effect of Mixture Ratio Variation on Radiation Intensity Experimental Results | 97 |
| 18. Typical Band Spectra of Reacted Rocket Combustion Chamber Structural Constituents | 116 |

SECTION 1

INTRODUCTION

This report presents the results of an analytical investigation of the emission spectra of the exhaust stream of selected rocket engine liquid propellant combinations to determine the feasibility of detecting these spectra as a measure of various propulsion system performance characteristics. The goals of this analysis were as follows:

- A. Problem Definition, including: need, background information and potential.
- B. Propellants Analysis, including: selection of combinations to be studied and theoretical emission wavelengths of selected systems.
- C. Signal Analysis, including: theoretical emission intensity of selected wavelengths and sensitivity of detecting instrumentation.
- D. Rocket Engine Analysis, including: design of engine to provide signal strength compatible with volumetric capacity of vacuum facility to be used for testing and calculation of instrumentation response to anticipated emission intensity.
- E. Mixture Ratio Analysis, including: calculation of the relationship between mixture ratio and plume emission and applicability of seeding.
- F. Exit Plane Gas Temperature Analysis, including: calculation of the relationship between nozzle exit plane gas temperature and plume emission and the relationship between mixture ratio and temperature.
- G. Malfunction Analysis, including: the feasibility of detecting metals and oxides quantitatively, applicability of "signal" coatings and the feasibility of detecting combustion instability.
- H. Flight Systems Analysis, including: possible configuration and parameters best monitored as determined from preliminary analysis.

The need for new methods of measuring chemical rocket engine operating parameters, as opposed to the force reaction measurements made during ground test, is apparent for in-flight monitoring and control of space vehicle propulsion systems. Past studies utilizing probes and similar devices inserted into the exhaust gas stream have distorted the gas flow causing uncharacteristic stream property measurements. But if accurate rocket engine performance measurements are to be made which do not rely on the assumption of constant throat area or thrust coefficient, or upon heavy liquid flow meters or ground designed devices, performance observations must be based upon exhaust stream properties.

One of the most promising methods of obtaining stream properties without

the use of a gas stream disturbing device is by spectroscopic analysis of the rocket exhaust stream constituents. Past experience by Astrosystems in the conduct of high altitude rocket plume studies in the ultraviolet, visible and infrared wavelengths, has revealed that a definite relationship exists between: propellants mixture ratio and exhaust constituents emission-band intensity, combustion temperature and exhaust constituents emission-band intensity, and incipient chamber wall oxidation and trace metal oxide contaminants in the exhaust gas composition.

Based upon the analysis presented herein, and the above-mentioned data, it seems highly probable that essential conditions of rocket engine performance can be determined spectrally thereby permitting an accurate computation to be made of overall engine efficiency. This would appear to be especially valuable for example, in pulsed engine operation in rendezvous or inter-orbital transfer where conventional instrumentation suffers from lack of rapid response. In addition, analysis by the subject means can serve very effectively in the prevention of major malfunctions through the immediate detection of combustion component failure. If automatic shutdown is initiated by spectral signals, then it should be possible to repair the rocket engine and make it useful again before it causes major destruction which may abort the mission.

It was the purpose of this program to illustrate the feasibility of obtaining propellant mixture ratio and combustion temperature by spectroscopic techniques, as well as providing a means for the detection of combustion chamber oxidation and/or combustion instabilities.

SECTION 2

PROPELLANTS ANALYSIS

It is the purpose of this program to illustrate the feasibility of obtaining rocket engine propellant mixture ratio and combustion temperature by spectroscopic analysis of the combustion stream properties, and to provide a means for the detection of combustion chamber oxidation and/or combustion instability.

In order to initiate this analysis propellant combinations were selected based on their probable applicability to the subject technique. These propellants were then theoretically analyzed to determine their thermodynamic characteristics and the molecular makeup of their combustion gases. In some cases the required thermodynamic data was not available in the open literature, primarily because a thorough mixture ratio analysis suitable to the purposes of this program had not been previously conducted. The thermodynamic information was then used as a basis for selecting the emission that could be expected from these gases in the ultraviolet, visible and infrared wavelength regions.

A. SELECTION

A number of space propulsion systems were reviewed to determine the propellants generally being considered for application and their probably operating combustion pressure. Reference (1), a general survey of propulsion requirements for future space missions, indicated a preference for liquid oxygen (LO_2)/liquid hydrogen (LH_2) at chamber pressures of 20 to 200 psia and nitrogen tetroxide (N_2O_4)/50% unsymmetrical dimethylhydrazine (UDMH)-50% hydrazine (50-50) at the same chamber pressures. A later study² considered the same two propellant combinations as those most likely to be used in space vehicles, but narrowed the probable operating chamber pressures to 50 psia for LO_2/LH_2 and 80 to 110 psia for $\text{N}_2\text{O}_4/50-50$.

Regarding systems currently under development, the "Surveyor" vernier propulsion engine operates on 90% N_2O_4 -10% nitrous oxide/monomethylhydrazine at 170 psia chamber pressure³; the Maneuvering Satellite propulsion systems currently under development at Bell Aerosystems for Edwards AFB operates on $\text{N}_2\text{O}_4/50-50$ at a mixture ratio of 2.1:1 and a chamber pressure of 65 psia. Testing at reduced chamber pressures (to 45 psia) however show little degradation in performance⁴. The Gemini Lunar Excursion Module reaction control system under development for NASA Manned Spaceflight Center operates on the same propellants at a mixture ratio of 2:1 and a chamber pressure somewhat less than 100 psia. Practical considerations to date have prevented the attainment of higher chamber pressure at near optimum mixture ratio.

Based upon the above, it was decided to select LO_2/LH_2 , $\text{N}_2\text{O}_4/\text{UDMH}$ (as chemically and spectroscopically representative of all the various hydrazine blends) and $\text{LO}_2/\text{RP-1}$ which is representative of most booster rocket systems. From a practical viewpoint it appears that chamber pressure values for most

space propulsion systems will be less than 100 psia. Hence, thermochemical analyses of the selected propellants were made at reduced chamber pressures.

B. METHOD OF ANALYSIS

In order to conduct thermodynamic analyses of the selected propellant combinations a determination must first be made as to the probable condition of the exhaust gases in the rocket nozzle; i.e., does the chemical reaction condition most nearly approach equilibrium, or does the reaction cease and the composition remain frozen? This question has never been answered analytically for flows of more than one chemical system, because as explained in Reference 5:

"There is a very serious shortage of the chemical kinetic data which is essential for the solution of non-equilibrium nozzle flow problems. Accurate data is completely lacking for the majority of reactions which are likely to occur, and resort must be made to order-of-magnitude guesses and extrapolations over large temperature ranges".

Actual testing of space application engines shows, however, that the typically large area ratios and low chamber pressures of these engines results in performance much closer to theoretical frozen than theoretical equilibrium⁶. Internal NASA documents⁷ support this view. It was, therefore, decided to conduct frozen analyses as being most representative of actual current conditions.

The requisite thermochemical calculations were then obtained employing existing computer programs. Species and temperature calculations for LO_2/LH_2 as detailed in Table 1 (following) were taken from the reference cited thereon (NASA Memo 5-21-59E). These calculations were conducted on an IBM 7090 computer, and the program employed for these thermochemical calculations is described in Huff, Gordon & Morrell NACA Report 1037 (1951). The $\text{LO}_2/\text{RP-1}$ data (Table 2) was calculated for Astrosystems in October 1961 under company sponsorship by the IBM Service Bureau using an IBM 7090. The program employed is described in G. S. Bahn, "Kinetics Equilibrium and Performance of High Temperature Systems", 2nd Conf., 1962, Gordon & Breach Pub., 1963, pp. 261-270.

The thermochemical calculations for $\text{N}_2\text{O}_4/\text{UDMH}$ applicable to this program were not available in the literature and were, therefore, calculated during the course of the work reported herein. These calculations were conducted at Thiokol Chemical Corporation using a CDC Bendix G-20 computer. No report reference exists for this particular program but the approach and equations solved are essentially the same as referenced above (Huff et al). The only input data required for a calculation were the assigned chamber and exhaust pressures, the elemental composition of each propellant ingredient, its heat of formation and mass used; a selection of either frozen or equilibrium expansion; and rough guesses for the chamber and exhaust temperatures. A sample calculation as printed by this computer is shown in Appendix A. It is possible to iteratively converge toward a desired nozzle expansion area ratio with this program, but this procedure is laborious. It is usually more

TABLE 1
THEORETICAL PERFORMANCE OF OXYGEN/HYDROGEN
(Frozen Flow, Pc = 60 Psia)

| Mixture Ratio | Molecu- lar Wt. | Major Exhaust Gas Constituents | | | | | |
|------------------|--------------------|--------------------------------|------------------|-----------------|------------------|-----------------|-------------------|
| | | \bar{M} | $\frac{H_2O}{H}$ | $\frac{H}{H_2}$ | $\frac{OH}{H_2}$ | $\frac{O}{H_2}$ | $\frac{O_2}{H_2}$ |
| 1.190 | 4.416 | | 0.15 | - | - | - | - |
| 1.587 | 5.216 | | .20000 | .00001 | - | - | - |
| 1.984 | 6.015 | | .24997 | .00017 | - | - | - |
| 2.381 | 6.812 | | .29975 | .00120 | .00005 | - | - |
| 2.778 | 7.597 | | .34873 | .00446 | .00041 | - | - |
| 3.175 | 8.363 | | .39584 | .01092 | .00161 | .00002 | .00001 |
| 3.571 | 9.102 | | .43989 | .02018 | .00435 | .00010 | .00003 |
| 3.968 | 9.811 | | .47996 | .03077 | .00915 | .00036 | .00015 |
| 4.762 | 11.142 | | .54591 | .04998 | .02520 | .00202 | .00119 |
| 5.556 | 12.360 | | .59195 | .06095 | .04705 | .00590 | .00488 |
| 6.349 | 13.470 | | .62032 | .06315 | .06925 | .01163 | .01305 |
| 7.143 | 14.479 | | .63534 | .05966 | .08775 | .01787 | .02642 |
| 7.937 | 15.399 | | .64117 | .05353 | .10118 | .02347 | .04445 |
| 11.905 | 18.987 | | .61197 | .02428 | .11322 | .03338 | .16807 |
| 15.873 | 21.453 | | .55950 | .01009 | .09071 | .02669 | .29223 |

REFERENCE: NASA Memo 5/21/59E "Theoretical Performance of Liquid Hydrogen with Liquid Oxygen as a Rocket Propellant", S. Gordon & B. J. McBride, June 1959.

TABLE 2

THEORETICAL PERFORMANCE OF OXYGEN/RP-1

(Frozen Flow, $P_c = 50$ Psia)

| Mixture Ratio (O/F) | 1.80 | 2.00 | 2.20 | 2.35 | 2.50 | 2.65 |
|-----------------------------|-------|-------|-------|-------|-------|-------|
| Molecular Wt. (\bar{M}) | 19.23 | 20.16 | 20.97 | 21.50 | 22.00 | 22.45 |

Major Exhaust Gas Constituents

| | | | | | | |
|------------------|--------|--------|--------|--------|--------|--------|
| CHO | .00004 | .00004 | .00003 | .00003 | .00003 | .00002 |
| CO | .43686 | .40622 | .37496 | .35251 | .33134 | .31153 |
| CO ₂ | .05383 | .07400 | .09323 | .10619 | .11776 | .12601 |
| H | .03874 | .05310 | .05910 | .05968 | .05839 | .05607 |
| H ₂ | .24298 | .18343 | .14154 | .11899 | .10169 | .08813 |
| H ₂ O | .21445 | .24860 | .26684 | .27384 | .27733 | .27857 |
| O | .00111 | .00467 | .01097 | .01659 | .02229 | .02768 |
| O ₂ | .00039 | .00254 | .00828 | .01526 | .02427 | .03491 |
| OH | .01159 | .02741 | .04504 | .05690 | .06691 | .07506 |

Minor Exhaust Gas Constituents

| | | | | | | |
|-------------------------------|-------------------|-------------------|-------------------|-------------------|-------------------|-------------------|
| C | 10 ⁻⁸ | 10 ⁻⁹ | 10 ⁻⁹ | 10 ⁻⁹ | 10 ⁻⁹ | 10 ⁻⁹ |
| C ₂ | 10 ⁻¹⁴ | 10 ⁻¹⁴ | 10 ⁻¹⁴ | 10 ⁻¹⁴ | 10 ⁻¹⁴ | 10 ⁻¹⁴ |
| C ₃ | 10 ⁻¹⁶ | 10 ⁻¹⁸ | 10 ⁻¹⁹ | 10 ⁻¹⁹ | 10 ⁻¹⁹ | 10 ⁻²⁰ |
| C ₄ | 10 ⁻²⁶ | 10 ⁻²⁶ | 10 ⁻²⁶ | 10 ⁻²⁷ | 10 ⁻²⁷ | 10 ⁻²⁷ |
| C ₅ | 10 ⁻³⁰ | 10 ⁻³¹ | 10 ⁻³² | 10 ⁻³² | 10 ⁻³³ | 10 ⁻³³ |
| CH | 10 ⁻⁸ | 10 ⁻⁹ | 10 ⁻⁹ | 10 ⁻⁹ | 10 ⁻⁹ | 10 ⁻¹⁰ |
| CH ₂ | 10 ⁻⁸ | 10 ⁻⁸ | 10 ⁻⁸ | 10 ⁻⁸ | 10 ⁻⁸ | 10 ⁻⁸ |
| CH ₃ | 10 ⁻⁸ | 10 ⁻⁸ | 10 ⁻⁸ | 10 ⁻¹⁰ | 10 ⁻¹⁰ | 10 ⁻¹⁰ |
| CH ₄ | 10 ⁻⁹ | 10 ⁻¹⁰ | 10 ⁻¹⁰ | 10 ⁻¹⁰ | 10 ⁻¹¹ | 10 ⁻¹¹ |
| C ₂ H ₂ | 10 ⁻¹¹ | 10 ⁻¹¹ | 10 ⁻¹² | 10 ⁻¹² | 10 ⁻¹² | 10 ⁻¹³ |

TABLE 2
Minor Exhaust Gas Constituents (continued)

| Mixture Ratio (O/F) | 1.80 | 2.00 | 2.20 | 2.35 | 2.50 | 2.65 |
|---------------------------------|-------------------|-------------------|-------------------|-------------------|-------------------|-------------------|
| C ₂ H ₄ | 10 ⁻¹⁵ | 10 ⁻¹⁵ | 10 ⁻¹⁶ | 10 ⁻¹⁶ | 10 ⁻¹⁷ | 10 ⁻¹⁷ |
| CH ₂ O | 10 ⁻⁶ | 10 ⁻⁶ | 10 ⁻⁶ | 10 ⁻⁶ | 10 ⁻⁶ | 10 ⁻⁷ |
| C ₂ H ₄ O | 10 ⁻¹⁸ | 10 ⁻¹⁸ | 10 ⁻¹⁸ | 10 ⁻²⁰ | 10 ⁻²⁰ | 10 ⁻²⁰ |
| C ₃ O ₂ | 10 ⁻¹⁵ | 10 ⁻¹⁵ | 10 ⁻¹⁵ | 10 ⁻¹⁵ | 10 ⁻¹⁵ | 10 ⁻¹⁵ |
| H ₂ O ₂ | 10 ⁻⁶ | 10 ⁻⁶ | 10 ⁻⁶ | 10 ⁻⁵ | 10 ⁻⁵ | 10 ⁻⁵ |
| O ₃ | 10 ⁻¹⁰ | 10 ⁻⁹ | 10 ⁻⁸ | 10 ⁻⁸ | 10 ⁻⁷ | 10 ⁻⁷ |

worthwhile to obtain answers at three to five assigned exhaust pressures for a given chamber condition and present the results in graphical form.

C. THERMODYNAMIC PROPERTIES

Table 1 presents the results of thermodynamic calculations for the LO_2/LH_2 system as conducted by the NASA Lewis Research Center at 60 psia chamber pressure and frozen flow conditions using the program described in the preceding section. Similar data is presented for $\text{LO}_2/\text{RP-1}$ and $\text{N}_2\text{O}_4/\text{UDMH}$ in Tables 2 and 3 as computed by this corporation in the manner previously explained. Figures 1-3 describe the variation in concentration of combustion species as a function of mixture ratio for the three propellant combinations. These plots are based upon the data presented in Tables 1-3.

It can be noted in Figure 1 that for LO_2/LH_2 both OH and O_2 increase significantly in the normal operating range of 4 to 6:1 while H_2O shows a 25% increase in concentration. Since temperature is also rising sharply in this region, it can be expected that emission intensity at the shorter wavelengths will show a significant increase with increasing mixture ratio (several orders of magnitude).

The major constituents of $\text{LO}_2/\text{RP-1}$ are plotted vs O/F in Figure 2. Of these species O_2 and OH again show considerable increase as a function of mixture ratio indicating that sharp emission changes can be expected in the UV region. The H_2O content shows a slowly rising concentration and CO a slowly declining concentration. Also of interest is the CO_2 content which increases about 50% with increasing mixture ratio and CHO which decays with mixture ratio.

The $\text{N}_2\text{O}_4/\text{UDMH}$ system displays the same major constituent variations as LO_2/LH_2 and $\text{LO}_2/\text{RP-1}$ but with some additions (see Figure 3). Both OH and O_2 show very marked increases with mixture ratio (in the O_2 case over four orders of magnitude); in addition NO, a good UV emitter, is also present in varying quantity. In this case CO_2 increases over an order of magnitude with increasing mixture ratio, but H_2O peaks at a maximum temperature.

In order to provide pertinent information for the analysis of plume intensity and simulated altitude test conditions, it was necessary to know the rocket engine exit temperature as a function of nozzle expansion ratio. Figures 4-6 were, therefore, prepared based upon the previously conducted thermodynamic analyses to provide that information for each propellant combination as a function of various mixture ratios. This analysis is, again, based on frozen flow considerations.

D. EMISSION WAVELENGTHS

Table 4 summarizes the emission characteristics of all species of interest from each of the three propellant combinations considered. It should be noted, however, that complete spectroscopic data for molecular fragments which often exist in rocket exhaust gases are far from complete.

TABLE 3
THEORETICAL PERFORMANCE OF $N_2O_4/UDMH$

| Mixture Ratio (O/F) Molecular Wt. (\bar{M}) | (Frozen Flow, Pc = 60 Psia) | | | | | |
|--|-----------------------------|-------|-------|-------|-------|-------|
| | 1.5 | 2.0 | 2.3 | 2.5 | 2.75 | 4.5 |
| | 18.68 | 21.00 | 22.08 | 22.70 | 23.38 | 26.46 |

Major Exhaust Gas Constituents

| | | | | | | | | |
|------------------|--------|--------|--------|--------|--------|--------|--------|--------|
| CO | .22296 | .18256 | .15636 | .13997 | .12129 | .07732 | .05667 | .04081 |
| CO ₂ | .02572 | .05037 | .06630 | .07584 | .08617 | .10743 | .11505 | .11930 |
| H | .01277 | .03092 | .03192 | .02992 | .02638 | .01614 | .01100 | .00757 |
| H ₂ | .27957 | .14595 | .09906 | .07820 | .05967 | .02971 | .01968 | .01335 |
| H ₂ O | .21020 | .29389 | .31225 | .31646 | .31660 | .30312 | .29089 | .27814 |
| N ₂ | .24608 | .26711 | .27524 | .27944 | .28380 | .29377 | .29902 | .30346 |
| NO | .00018 | .00302 | .00668 | .00935 | .01251 | .01954 | .02230 | .02378 |
| O | .00007 | .00277 | .00709 | .01021 | .01363 | .01885 | .01873 | .01736 |
| O ₂ | .00002 | .00225 | .00896 | .01657 | .02898 | .07691 | .11192 | .14628 |
| OH | .00240 | .02114 | .03610 | .04402 | .05094 | .05718 | .05473 | .04991 |

Minor Exhaust Gas Constituents

| | | | | | | | | |
|----------------|-------------------|-------------------|-------------------|-------------------|-------------------|-------------------|-------------------|-------------------|
| C ₂ | 10 ⁻¹⁶ | 10 ⁻¹⁷ | 10 ⁻¹⁷ | 10 ⁻¹⁷ | 10 ⁻¹⁶ | 10 ⁻¹⁸ | 10 ⁻²⁰ | 10 ⁻²¹ |
| CH | 10 ⁻¹¹ | 10 ⁻¹¹ | 10 ⁻¹² | 10 ⁻¹² | 10 ⁻¹² | 10 ⁻¹³ | 10 ⁻¹³ | 10 ⁻¹⁴ |
| CN | 10 ⁻⁶ | 10 ⁻⁶ | 10 ⁻⁸ | 10 ⁻⁹ | 10 ⁻⁹ | 10 ⁻¹⁰ | 10 ⁻¹⁰ | 10 ⁻¹¹ |
| HCO | 10 ⁻⁶ | 10 ⁻⁶ | 10 ⁻⁶ | 10 ⁻⁶ | 10 ⁻⁶ | 10 ⁻⁶ | 10 ⁻⁶ | 10 ⁻⁷ |
| NH | 10 ⁻⁶ | 10 ⁻⁶ | 10 ⁻⁶ | 10 ⁻⁶ | 10 ⁻⁶ | 10 ⁻⁶ | 10 ⁻⁶ | 10 ⁻⁷ |

AFPHL-TR-66-163

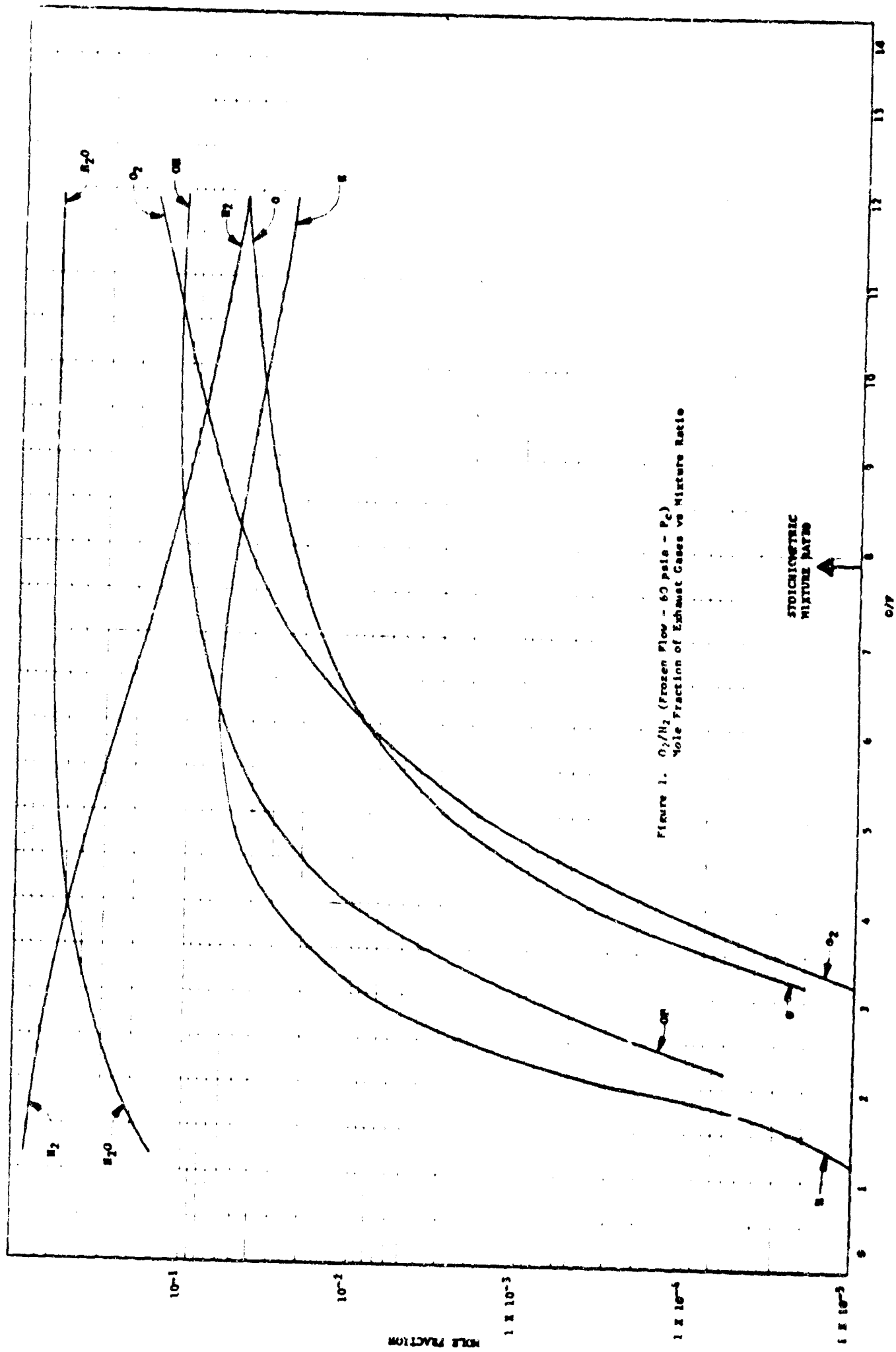


Figure 1. O₂/H₂ (Frozen Flow - 60 psia - P_c)
Mole Fraction of Exhaust Gases vs Mixture Ratio

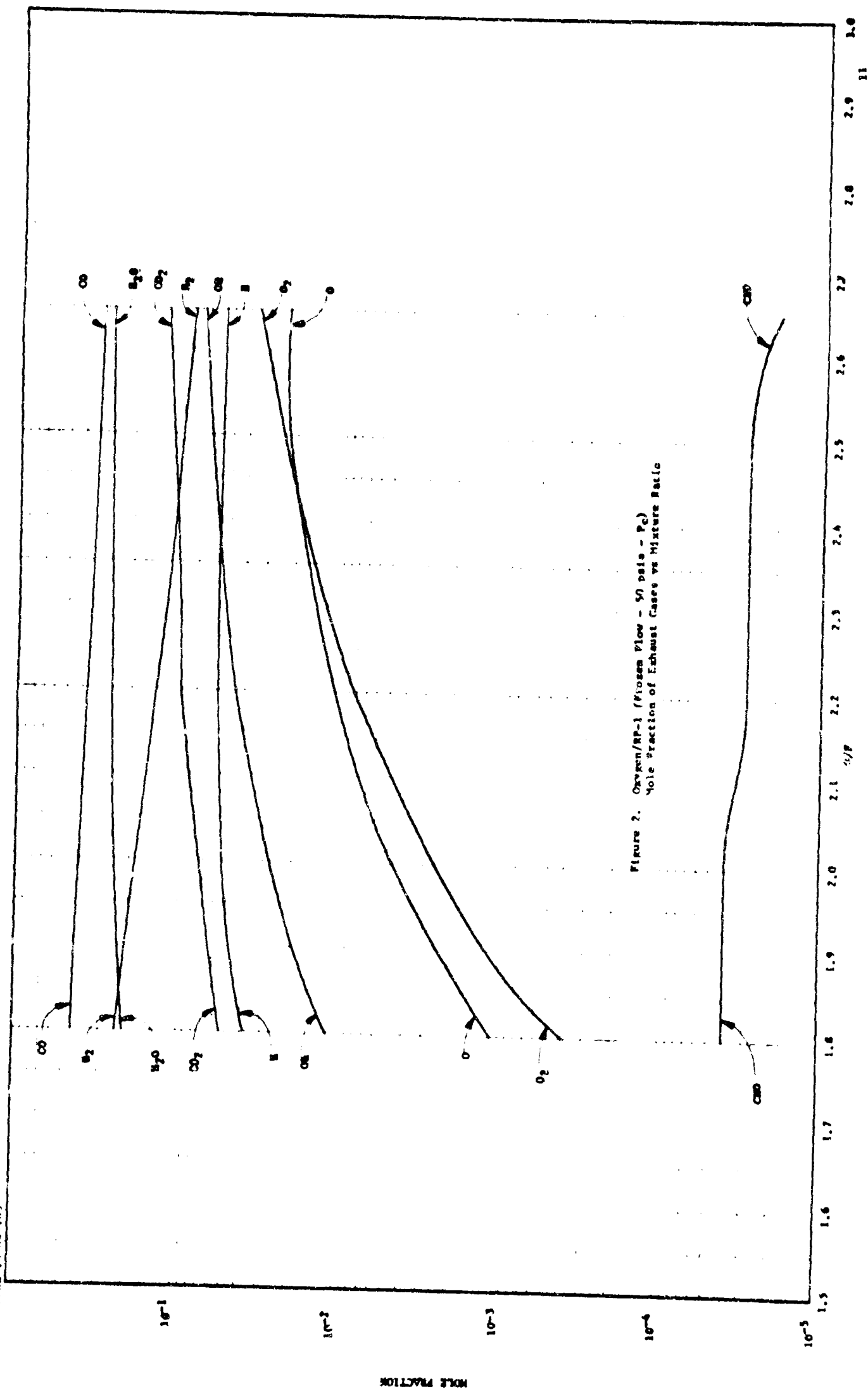


Figure 2. Oxygen/RP-1 (Piston Flow - 50 psi - P_c)
Mole Fraction of Exhaust Gases vs Mixture Ratio

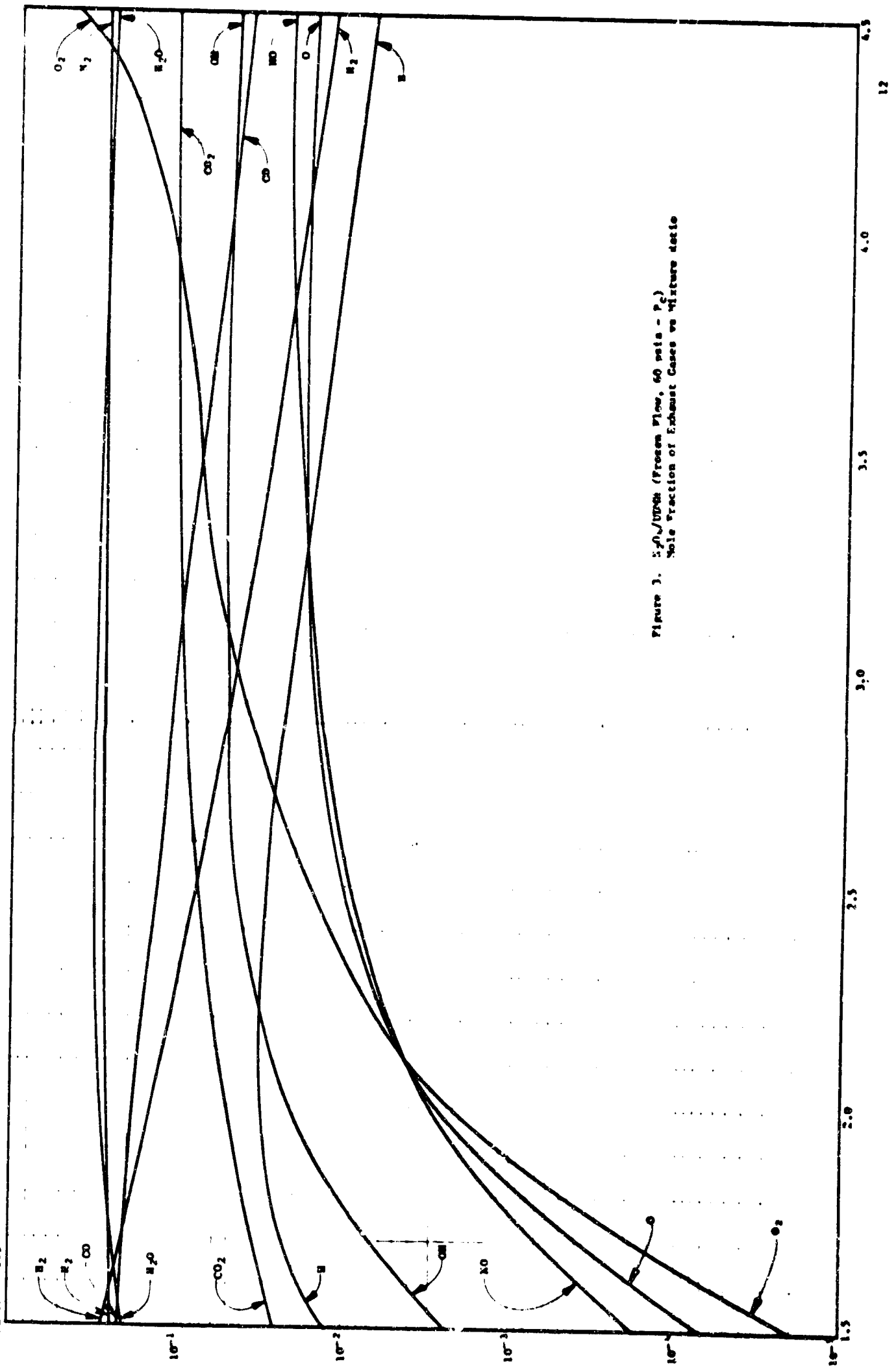


Figure 3. $5.70/1000$ (Frozen Flow, 60 psia - P_c)
Mole Fraction of Exhaust Gases vs Mixture Ratio

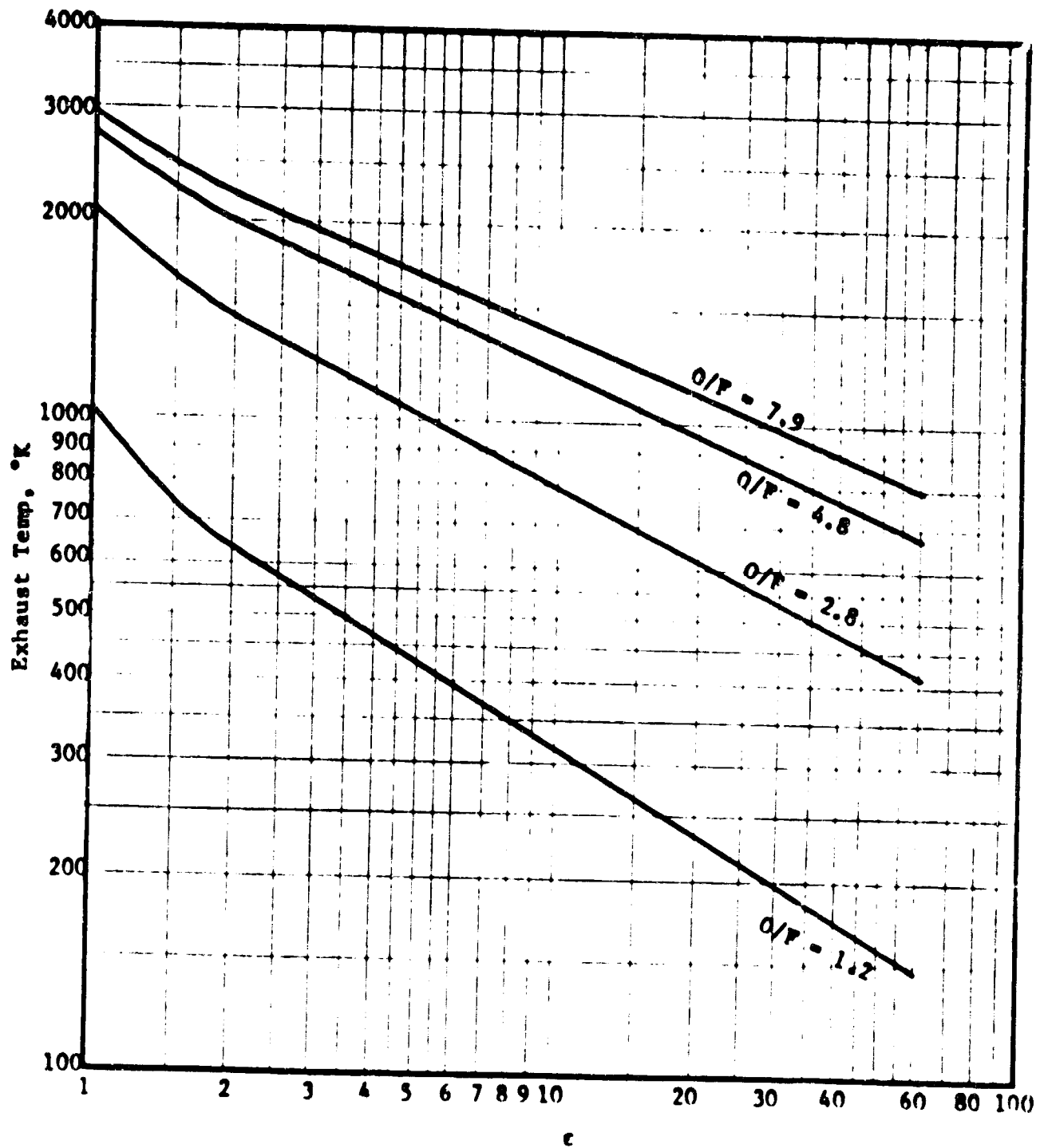


Figure 4. Oxygen-Hydrogen Exhaust Gas Temperature as a Function of Expansion Ratio and Mixture Ratio

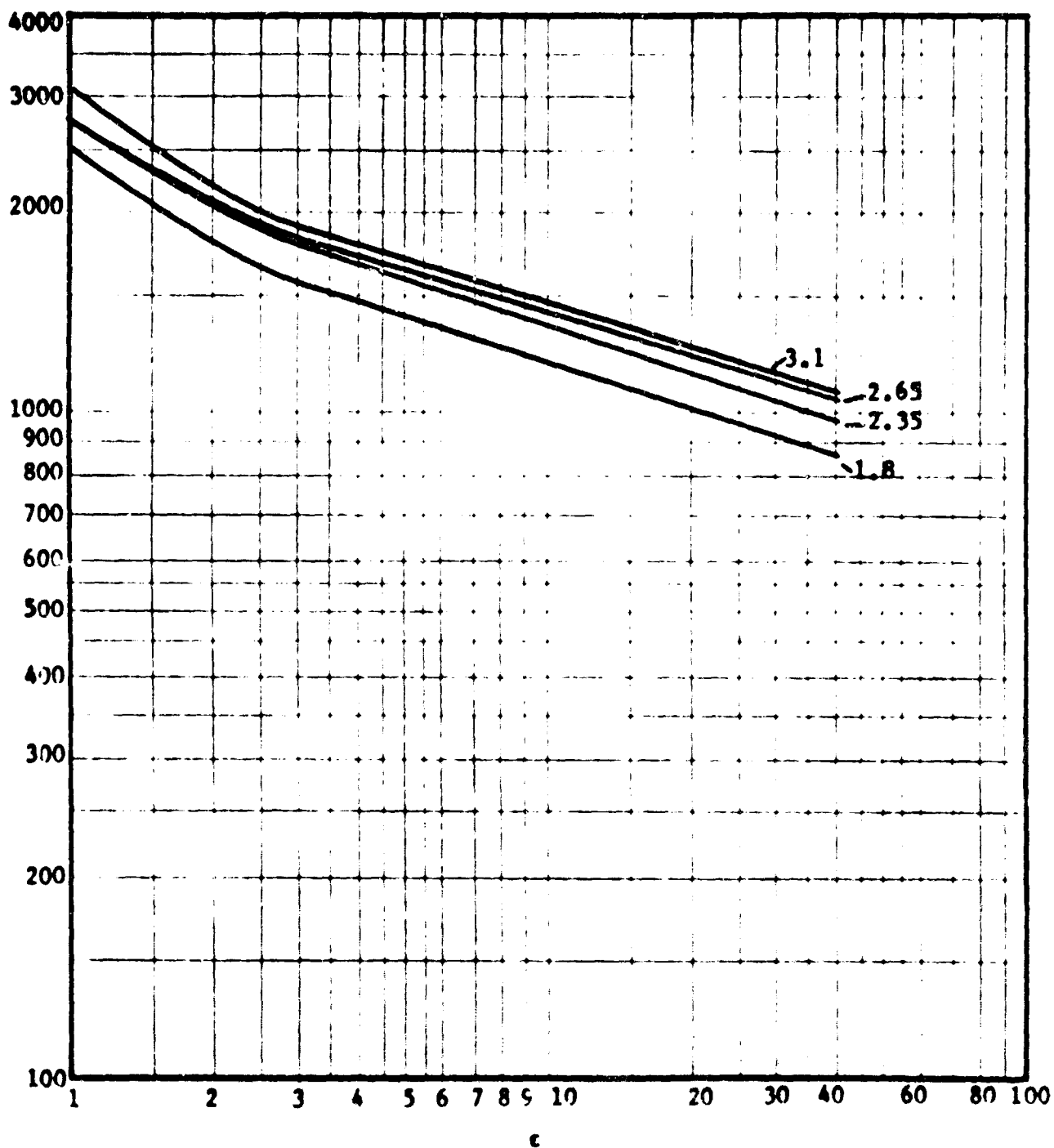


Figure 5. Oxygen - RP-1 Exhaust Gas Temperature as a Function of Expansion Ratio and Mixture Ratio

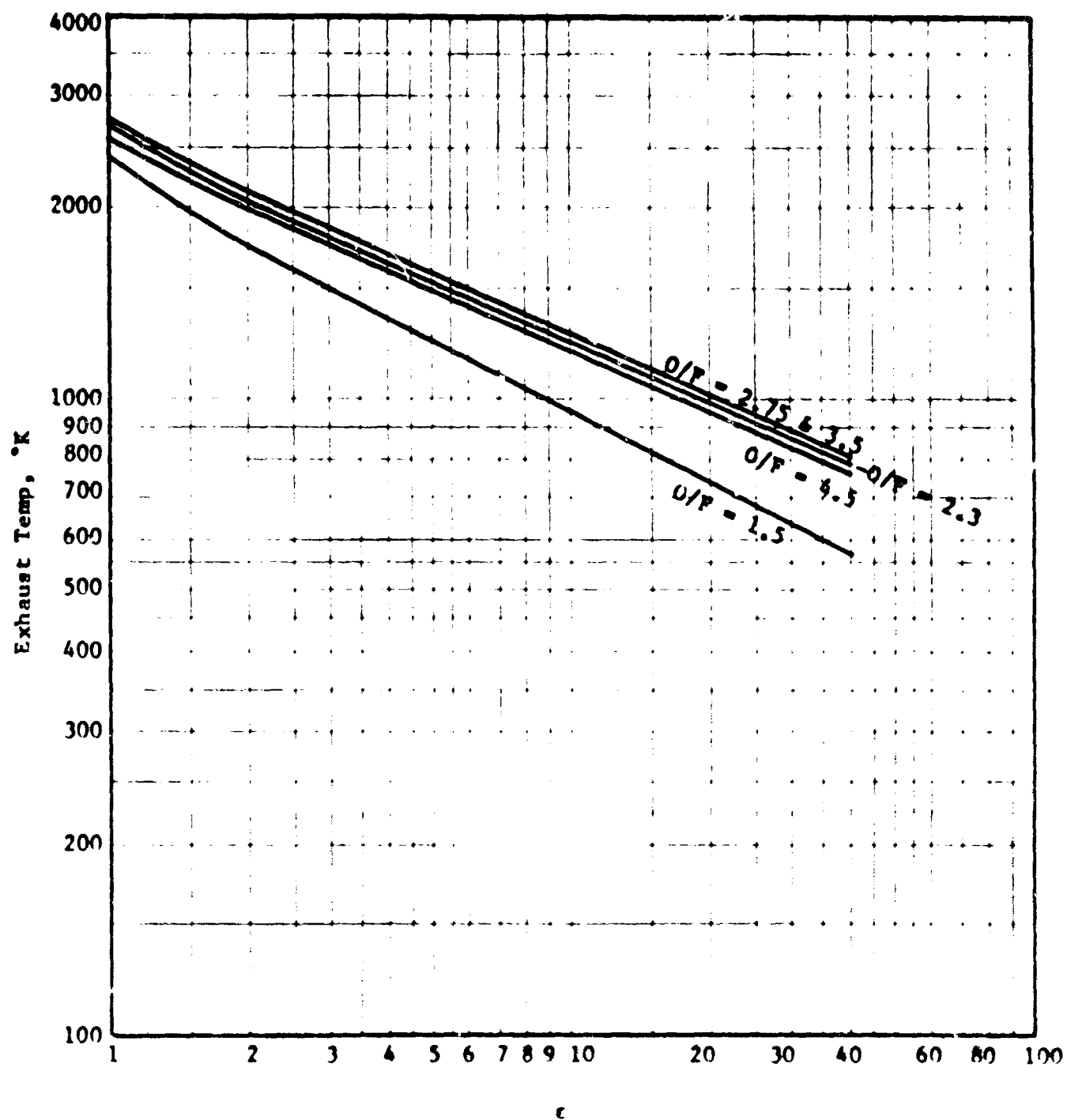


Figure 6. N_2O_4 - UDMH Exhaust Gas Temperature as a Function of Expansion Ratio and Mixture Ratio

TABLE 4

**EMISSION KNOWN TO ARISE FROM COMBUSTION
(PERSISTENT BAND HEADS ONLY)**

| <u>Specie</u> | <u>Wavelength</u> |
|---------------------------------|--|
| C ₂ | 6191.2, 6122.1, 6059.7, 6004.9, 5958.7, 5635.5, 5165.2, 4737.1, 4382.5, 2325 Å |
| CH | 4890, 4312.5, 3889.0, 3156.6, 3144 Å |
| CH ₄ | 7.6, 3.4, 3.3 μ |
| C ₂ H ₂ | 16.3, 13.8, 5.0, 3.0 μ |
| C ₂ H ₄ | 12.1, 10.6, 7.4, 6.9, 6.1, 3.3 μ |
| CHO | 4092.0-2585.5, 3802.7-2704.5 Å |
| CH ₂ O | 5107-3410 Å; 8.5, 7.8, 6.6, 5.7, 3.6, 3.4 μ |
| C ₂ H ₄ O | 14.6, 12.4, 11.6, 8.7, 7.9, 6.9, 6.7 μ |
| CO | 2800- < 2000 Å |
| CO ₂ | 5430-3911 Å; 15, 7.6, 7.2, 4.3 μ |
| C ₃ O ₂ | 16.1, 11.8, 6.4, 4.5 μ |
| H ₂ | (many line continuum) |
| H ₂ O | 9669, 8916, 8097, 7164.5, 6922, 6516.8, 6490.4, 6468, 6165.7 Å; 15.0, 6.26, 3.17, 2.74, 2.66, 1.88, 1.38, 1.14 μ |
| H ₂ O ₂ | 11.5, 7.3, 3.5, 2.93, 0.97 μ |
| N ₂ | > 10,000-5000 Å |
| NH | 3609.6, 3360, 3240.1, 3035.2 Å |
| NO | 5270-2018, 3458-1956 Å |
| CN | 4606.2, 4216.0, 3883.4 |
| O ₂ | 4400- < 2200 Å |
| O ₃ | 14.1, 9.6, 5.75 μ |
| OH | 3063.6, 2811.3 Å; 3.1-2.7 μ |

REFERENCES: Rosen, B. "Donnees Spectroscopiques Concernant les Molecules Diatomiques"; Paris 1951.

Pearse, R.W.B. and Gaydon, A.G. "The Identification of Molecular Spectra"; London 1950.

The emission wavelengths shown are those which can be expected to occur during a combustion process. Table 5 summarizes the adsorption spectra that might be obtained from combustion flames of the type studied herein.

In reviewing the exhaust gas constituents for each propellant combination as a function of the emission spectra which can be expected, the following observations can be made for LO_2/LH_2 . The only exhaust gas constituents of spectroscopic interest are H_2O , OH and O_2 . Both ionized H and O present a true continuum while H_2 displays the characteristic "many-line" continuum. It can be noted from the compilation presented in Table 4 that OH and O_2 both emit in the UV region while H_2O presents considerable orange emission as well as the known, strong IR emission. Table 5 presents known UV and visible absorption regions for species of interest in this program. Although self-absorption may not be a problem in a rocket plume under space conditions, known absorption regions are probably best avoided at this time. Hence, it would appear that the bands of most interest in LO_2/LH_2 studies are the OH 3064 and 2811Å regions, the O_2 4400-2200Å region and the H_2O 6166Å region. It will be necessary to confirm this through experimental spectroscopic scans, however, over the full range of interest for this propellant system 0.22-6.3μ.

In the case of $\text{LO}_2/\text{RP-1}$ it is interesting to note that the large number of minor constituents, or exhaust gas molecular fragments, which arise during this combustion process add an unknown factor to the analysis of this propellant combination. Past spectral analyses of $\text{O}_2/\text{RP-1}$ conducted at Tullahoma under moderate test altitude conditions show strong emission attributed to C_2 in the exhaust⁸. Most of this radiation occurs in the visible, providing the characteristic yellow-orange color of the RP flame. Other radicals which can be expected to emit strongly because of their excited nature are CH and CHO. Both are strong UV emitters and, if not overly sensitive to mixture ratio change, may prove to be good performance indicators.

For $\text{N}_2\text{O}_4/\text{UDMH}$ the rise and decline characteristics of H_2O make its use less likely for O/F monitoring because of the difficulty in determining which side of peak is indicated by the signal. CO, however, may be a good indicator in the UV. Of the minor constituents it can be expected that CH, CHO, NH and CN will emit strongly. C_2 emission is not anticipated in this system since the UDMH molecule contains C-N, N-H and C-H bonds, but no C-C bonds. The most promising emitters for performance determination in $\text{N}_2\text{O}_4/\text{UDMH}$ can, therefore, be expected to be OH, O_2 , CH, CN, NO and NH, all good UV emitters.

TABLE 5
 ABSORPTION SPECTRA OF COMBUSTION SPECIES
 (PRIMARYLY PERSISTENT BAND HEADS)

| <u>Specie</u> | <u>Wavelength</u> |
|---------------|---|
| C_2H_2 | 7901-7874, 2377-2245.8 Å |
| CH_2O | 3456-2667 Å |
| C_2H_4O | 3399.3-3172.2 Å |
| C_3O_2 | 3350-2946 Å |
| H_2O | 9420, 9060, 8227, 7227, 6994, 6524, 6324, 5952, 5924, 5722, 1780-1610, 1400-1300 Å |
| H_2O_2 | 3700-2150 Å |
| NO | 2415-1910 Å |
| O_2 | 7593.7, 6867.2, 6276.6, 2221-1768 Å |
| O_3 | 6020, 5730, 3432-3090 Å |

REFERENCES: Rosen, B., "Donnees Spectroscopiques Concernant les Molecules Diatomiques", Paris 1951.

Pearse, R.W.B. and Gaydon, A.G., "The Identification of Molecular Spectra", London 1950.

SECTION 3

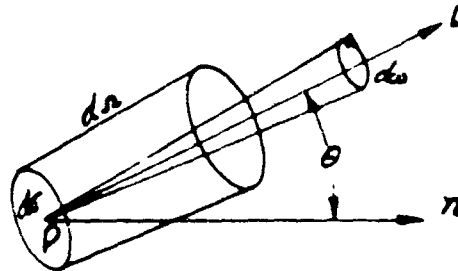
SIGNAL ANALYSIS

This section describes the methods used and results obtained in determining the emission intensities anticipated at the wavelengths of principal interest and the calculated instrumentation response to those intensities (signals).

A. EMISSION INTENSITIES

Emission intensities in the UV, visible and IR were calculated on a digital computer employing a program prepared during this project. In order to describe the manner in which these calculations were made, a review of applicable physical principles is presented followed by a description of the program and terminating with a presentation of the results obtained.

1. Definitions - Consider a cavity penetrated in all directions by radiation. In this cavity select an arbitrarily oriented small area ds and erect on it at the point P a normal n . Then draw a line L at an angle θ to the normal, which then is taken as an axis for an element of solid angle $d\omega$.



The cone $d\Omega$ is similar to the cone $d\omega$. Its cross-sectional area at the point P, perpendicular to L will be $ds \cos \theta$. The quantity of energy dE_ν passing in time dt through the area ds inside the cone $d\Omega$ in the frequency interval between ν and $\nu + d\nu$ is called the specific intensity of radiation or just the intensity, and is defined by the following limit:

$$I_\nu = \lim_{d\nu, dt, d\omega, ds \rightarrow 0} \frac{dE_\nu}{ds d\omega dt d\nu \cos \theta} \text{ in erg-cm}^{-2}\text{-sr}^{-1}\text{-sec}^{-1} \quad (3.1)$$

so that:

$$dE_\nu = I_\nu ds \cos \theta dt d\omega d\nu \quad \text{in erg} \quad (3.2)$$

The intensity due to the whole spectrum is obtained simply by:

$$I = \int_0^\infty I_\nu d\nu \quad (3.3)$$

and is called the integrated intensity.

The total amount of radiant energy traversing the surface element ds from one side to another, expressed in terms of unit area and unit time, can

be written as:

$$F_+ = \int_0^{2\pi} \int_0^{\pi/2} I \sin\theta \cos\theta d\theta d\phi \quad \text{in erg-cm}^{-2}\text{-sec}^{-1} \quad (3.4)$$

and is called the radiation flux.

The radiation flux going in the opposite direction is:

$$F_- = \int_0^{2\pi} \int_{\pi/2}^{\pi} I \sin\theta \cos\theta d\theta d\phi \quad \text{in erg-cm}^{-2}\text{-sec}^{-1} \quad (3.5)$$

The net flux of radiation, F , across ds per unit area per unit time is:

$$F = F_+ - F_- \quad \text{and} \quad (3.6)$$

$$F = \int_0^{2\pi} \int_0^{\pi} I \sin\theta \cos\theta d\theta d\phi \quad \text{erg-cm}^{-2}\text{-sec}^{-1} \quad (3.7)$$

or

$$F = \int I \cos\theta d\omega \quad (3.8)$$

over the complete sphere.

The amount of radiant energy flowing from one element of surface to another element of surface will now be derived.

Let ds and ds' be the two elements of surface surrounding the points P and P' , respectively. Let r be the distance between P and P' . Further, let PP' make angles θ and θ' to the direction of the normals to ds and ds' at P and P' , respectively. Finally, let I be the specific intensity at P in the direction PP' . In free space the energy which traverses the element ds in time dt and which also traverses ds' is, according to our definition of intensity,

$$dE = I \cos\theta ds d\omega dt \quad (3.9)$$

where $d\omega$ is the solid angle which the element ds' makes at P . This is seen to be:

$$d\omega = \frac{ds' \cos\theta'}{r^2} \quad \text{element of solid angle} \quad (3.10)$$

From the two equations (3.9) and (3.10) we have

$$dE = I \frac{\cos\theta \cos\theta' ds ds'}{r^2} dt \quad (3.11)$$

which implies that the specific intensity is constant along the path of any ray in free space.

Let us now consider the energy density. The energy density u of the

integrated radiation at a given point is the amount of radiant energy per unit volume which is in course of transit, per unit time, in the neighborhood of a point under consideration. The energy density is given by:

$$u = \frac{1}{c} \int I d\omega \quad \text{erg-cm}^{-3} \quad (3.12)$$

also

$$u_\nu = \frac{1}{c} \int I_\nu d\omega \quad \text{erg-cm}^{-3} \cdot (\text{frequency interval})^{-1} \quad (3.13)$$

and

$$u = \int_0^\infty u_\nu d\nu \quad (3.14)$$

If the radiation is isotropic,

$$u_\nu = \frac{4\pi}{c} I_\nu \quad u = \frac{4\pi}{c} I \quad (3.15)$$

Equation (3.11) establishes the geometric relation between the detector and the light source. One can take θ and $d\sigma$ as pertaining to the source and θ' and $d\sigma'$ as pertaining to the detector. The area of the source viewed by the detector is determined by the cone defined by the acceptance angle of the detector's sensitive area. In the case where a large section of the source is viewed, then the element of area is integrated over that section.

2. Optical Depth of Radiation Source - The intensity of the radiation observed from the surface of light source may not always depend only on the area viewed, but also on the geometrical depth of the emitting layer. This means, essentially, that the intensity I included in equation (3.11) can be a function of s , the depth of the emitting layer along the line of sight.

There are two extreme cases in categorizing light sources; the case of an optically thin source and the case of an optically thick source. Optical thickness is defined as:

$$\tau_\nu = \int_0^s K_\nu ds \quad (3.16)$$

and for a homogeneous layer

$$\tau_\nu = K_\nu \cdot s \quad (3.17)$$

where s is the depth of the emitting layer. In order to qualify the sources, the parameter to be used will be the ratio of the geometrical thickness of the emitting layer to the mean free path of the photon for the particular frequency of interest.

$$\frac{s}{l_{ph}} = \tau_\nu = K_\nu \cdot s \quad \text{since } K_\nu = \frac{1}{l_{ph}} \text{ cm}^{-1} \quad (3.18)$$

In the case of a homogeneous emitting layer where $\frac{s}{l_{ph}} \ll 1$, that is in the optically thin case, the intensity I is given by:

$$I_{nm} = A_{nm} E_{nm} N_n s \quad \text{erg-cm}^{-2}\text{-sec}^{-1}\text{-sr}^{-1} \quad (3.19)$$

where A_{nm} is the Einstein transition probability in $\text{sec}^{-1}\text{-sr}^{-1}$, and I_{nm} indicates the radiated specific intensity for a transition $m \rightarrow n$, n being the upper state of the atom or molecule. E_{nm} is the energy difference between the states, N_n is the number density of particles in the upper state in cm^{-3} and s is the depth of the emitting layer in cm. In the optically thin source, therefore, the radiation emitted is isotropic and depends on the source geometrical thickness.

For an intermediate situation where $\frac{s}{l_{ph}} < 1$, equation (3.19) becomes:

$$I_{nm} = A_{nm} E_{nm} N_n \cdot s (e^{-\tau_v}) \quad \text{erg-cm}^{-2}\text{-sec}^{-1} \quad (3.20)$$

The factor $(e^{-\tau_v})$ allows for the fact that there exists appreciable absorption of radiation along the line of sight. The radiation detected in this case depends on both s and $e^{-K_v \cdot s}$.

When the optical depth of the source is $\frac{s}{l_{ph}} \sim 1$ or larger, than the source radiation may be described in terms of a blackbody for the frequency interval where the optical depth is large, and at the temperature of the source. Under such circumstances the radiation intensity becomes $I_v = B_v(T)$, where $B_v(T)$ is the Planck radiation law and therefore independent of the geometrical depth of the light source along the path of observation. The intensity $B_v(T)$ depends on the surface area of the source viewed by the detector.

3. Computer Program - The radiation equations programmed on the digital computer were derived assuming an optically thin homogeneous source. The radiation intensity for this homogeneous source is proportional to the thickness of the radiating layer as indicated in the previous section. For a homogeneous source where absorption becomes important, the radiation intensity is dependent upon the absorption factor $e^{-\tau}$ where τ is the optical thickness of the radiating layer and has a role analogous to that which the Knudsen number plays in rarefied gas dynamics. For a thick radiator approaching blackbody emitter, the radiation is independent of the thickness.

In this calculation the collision rates among the plume constituents were assumed to be high enough so that local thermodynamic equilibrium existed. The Maxwellian velocity distribution, the Boltzman distribution of excited states and the Saha equation were assumed to apply.

The intensity of vibrational bands which are associated with electronic transitions and which appear as radiation in the visible and ultraviolet were calculated for optically thin sources as follows:

$$I_{v',v''}(s) = \frac{16\pi^3}{3c^3} \nu_{v',v''}^4 \frac{P_{v',v''}}{g_m} N_{v'} \cdot s \quad (3.21)$$

The intensity of pure molecular vibrational bands which radiate in the infrared were calculated for thin sources as follows:

$$I_{v',v''}(s) = \frac{16\pi^3}{3c^3} ([M]^{v',v''})^2 N_{v'} \cdot s \quad (3.22)$$

Both equations are for a homogeneous emitting layer.

In the above equations $P_{v',v''}$ is the "band strength", in erg-cm^3 , g_m is the statistical weight of the upper state, s is the depth of the emitting layer along the line of sight in cm, and $N_{v'}$ is the population of the upper vibrational state in cm^{-3} which is calculated by:

$$N_{v'} = N \frac{(g_m)}{Z} e^{-X_m/kT} \left(\frac{e^{-X_{v'}/kT}}{O_{v'}} \right) \quad (3.23)$$

Where N is the total number density for the species under consideration, Z the electronic partition function, $O_{v'}$ the vibrational partition function, X_m the energy of the m state measured from ground state, $X_{v'}$ the energy of the v' vibrational state measured from the $v=0$ state, and:

$$O_{v'} = 1 + e^{-X_{v'}/kT} + e^{-X_{v''}/kT} + \dots \quad (3.24)$$

Where k is the Boltzman constant and T the temperature in $^{\circ}\text{K}$.

$\{[M]^{v',v''}\}^2$ in equation (3.22) is the pure vibrational band strength and can be calculated as follows:

$$fK_{\nu} d_{\nu} = \frac{2\pi^2 \nu_{v',v''}}{3ch} \{[M]^{v',v''}\}^2 N_{v''} \quad (3.25)$$

Where K_{ν} is the absorption coefficient in cm^{-1} , defined for S.T.P. conditions, h is Planck's constant (6.6×10^{-27} erg-sec) and c is the speed of light.

Equation (3.21) was rewritten in the following form before being programmed:

$$I_{v',v''}(s) = 5.33(\pi/c)^3 (E_{v',v''}/h)^4 P_{v',v''} N_{v'} s / g_m \quad (3.26)$$

With the existing G-20 propellant performance analysis program no provision exists for printing out values for the throat pressure and temperature. Hence, for expediency, data was calculated at $P_c/P_e = 2.0$ which approximates the sonic throat condition to within one percent ($A_e/A_t = 1.01$). Because of the uncertainty in experimental combustion temperature which is always lower than theoretical (due to heat transfer and incomplete combustion) this degree of approximation was deemed acceptable. Copies of the UV and IR radiance programs (written in GATE

translation languages) are shown in Appendix 3. The input data required include the mach cone temperature (taken as T_0 , calculated previously), the pressure, species mole fraction (assuming frozen composition) molecular constants and transition probabilities.

4. Tabulation of Constants - Before initiating the computer analysis it was first necessary to tabulate the radiation constants for the species of interest. An extensive survey was conducted (see General References list) to obtain the requisite constants, but the computer analysis was limited by the unavailability of constants for some of the more "exotic" species which generally occur only under the conditions of high temperature and pressure that exist in a rocket combustion chamber. Following are the main bands from which intensities were computed for selected frequencies:

- (a) C_2
 2325Å (Mulliken's System) Probably $d^1\Sigma \rightarrow a^1\Sigma (0,0)$
 Also intense bands in the Swan System $A^3\Pi \rightarrow X^3\Pi$

Swan System:

| <u>B, Å.</u> | <u>Relative Intensity</u> | <u>Vibrational Transition</u> |
|--------------|---------------------------|-------------------------------|
| 5635.5 | 8 | (0,1) |
| 5585.5 | 3 | (1,2) |
| 5540.7 | 6 | (2,3) |
| 5165.2 | 10 | (0,0) |
| 5129.3 | 6 | (1,1) |
| 4737.1 | 9 | (1,0) |
| 4715.2 | 8 | (2,1) |
| 4697.6 | 7 | (3,2) |
| 4684.8 | 4 | (4,3) |

- (b) CH
4300Å System

| | | |
|--------|----|--------------------------------------|
| 4312.5 | 10 | (0,0) $A^2\Delta \rightarrow X^2\Pi$ |
|--------|----|--------------------------------------|

5700Å System

| | | |
|--------|---|--------------------------------------|
| 3889.0 | 4 | (0,0) $B^2\Sigma \rightarrow X^2\Pi$ |
|--------|---|--------------------------------------|

- (c) CHO
System A

| | | |
|---------|----|-------|
| 3588.6Å | 8 | |
| 3502.7 | 8 | |
| 3377.4 | 10 | (1,9) |
| 3299.2 | 10 | (0,8) |
| 3014.8 | 8 | |
| 2948.2 | 7 | |
| 2858.0 | 6 | |

| <u>B.H.</u> | <u>Relative Intensity</u> | <u>Vibrational Transition</u> |
|---|---------------------------|-------------------------------|
| <u>System B</u> | | |
| 3359.0Å | 5 | (1,9) |
| (d) CO ₂ | | |
| I.R. Bands at 2.7μ, 4.3μ, 15μ | | |
| (e) CO | | |
| Fourth Positive System $A^1\pi \rightarrow X^1\Sigma$ | | |
| 2286.1 | 7 | (6,15) |
| 2311.5 | 8 | (7,16) |
| 2337.9 | 7 | (8,17) |
| 2381.6 | 6 | (6,16) |
| 2407.6 | 7 | (7,17) |
| 2433.9 | 9 | (8,18) |
| 2463.2 | 10 | (9,19) |
| 2509.9 | 8 | (7,18) |
| 2567.8 | 5 | (9,20) |
| 2492.9 | 8 | (10,20) |
| (f) H ₂ O | | |
| I.R. Bands 1.38μ, 1.88μ, 2.66μ, 2.74μ, 3.17μ, 6.26μ | | |
| (g) NH | | |
| $A^3\pi \rightarrow X^3\Sigma$ | | |
| 3360Å | | (0,0) |
| 3370 | | (1,1) |
| (h) NO | | |
| <u>B System</u> | | |
| $B^2\pi \rightarrow X^2\pi$ | | |
| 2198.8Å | | (0,0) |

γ System $A^2\Pi \rightarrow X^2\Pi$

2262.8Å

(0,0)

(i) CN

 $B^2\Sigma \rightarrow X^2\Sigma$ Violet System

3883.4

10

(0,0)

3871.4

9

(1,1)

3861.9

8

(2,2)

3854.7

6

(3,3)

(j) OH

 $A^2\Sigma \rightarrow X^2\Pi$

3063.6

10

(0,0)

2811.3

6

(1,0)

5. Results Obtained - The types of radiation expected to be emitted by a rocket plume are molecular: electronic-vibrational and pure vibrational-rotational bands in the ultraviolet-visible and infrared; and blackbody radiation. Some of the exhaust product specie concentrations were not calculated by the computer as their molar fractions were below the limit of the machine's capability ($<10^{-6}$). These had to be hand calculated assuming chemical equilibrium exists in the rocket combustion chamber and subsequently the gas flow through the rocket nozzle is frozen, thus maintaining constant composition.

Table 6 gives the results of intensity calculations for the primary vibrational bands associated with electronic transitions in the UV-visible. Calculations were made for $\text{LO}_2/\text{RP-1}$ (Table 6, Part A) and $\text{N}_2\text{O}_4/\text{UDMH}$ (Part B) propellants. It is of interest to note that the null radiant intensity calculation result for the 3064\AA OH band at the Mach cone is due to high self absorption. It is possible to observe this band at the Mach cone but only blackbody type radiation. A spectral (3064\AA) blackbody intensity calculation for the temperature indicated, yielded a value of 5.16×10^{-6} watts/cm²/ster. Chemiluminescence and non-equilibrium effects will affect the radiation intensities computed. Also, inhomogeneous burning will result in pockets of combustion species and, in turn, will change their number density. This will also noticeably affect the radiation intensity.

Table 7 presents a detailed listing of the UV-visible radiation which can be expected from the secondary transitions of the prime radiating species in the $\text{LO}_2/\text{RP-1}$ exhaust flame. This data indicates that several CH, OH and CO lines will be detectable and many C_2 lines will also be detectable.

Employing the computer program previously described, calculations were carried out to determine the primary radiation intensity of the plume at the Mach cone in the IR portion of the optical spectrum. It was assumed that the plume thickness was 2 cm, and that the band width $\Delta\nu$ was 0.2 cm^{-1} . These results are presented in Table 8. The vibrational-rotational bands calculated are, for the most part, readily detectable.

Blackbody radiation intensities can be calculated by the following expression:

$$I_v = B_v - \frac{I}{K_v}, \text{ grad}_s B_v \quad (3.27)$$

where I_v = radiation per unit area per steradian for the surface in question,

B_v = radiation from a blackbody surface at temperature T for a particular wavelength,

K_v = absorption coefficient in cm^{-1} .

The blackbody intensity per steradian can be calculated from the Planck distribution:

$$B_v = C_1 \bar{\nu}^3 / (e^{C_2 \bar{\nu}/T} - 1) \quad (3.28)$$

where $C_1 = 1.1909 \times 10^{12}$ watts/cm²/ster

$C_2 = 1.4388 \text{ cm}^{-1}\text{K}$

$\bar{\nu}$ = wave number = $1/\lambda = \nu/c$

The gradient of B_v along s ($\partial B_v / \partial s$) can be calculated provided the quantity $\partial T / \partial s$ is known, since:

$$\partial B_v / \partial s = (\partial B_v / \partial T) (\partial T / \partial s) \quad (3.29)$$

TABLE 6

UV-VISIBLE PRIMARY RADIATION INTENSITY AT THE MACH CONE

Part A

Propellant: LO₂/RP-1
 O/F Ratio: 3.4 (stoichiometric)
 Chamber Pressure: 100 psia
 Exhaust Pressure: 50 psia
 Exhaust Temperature: 2953°K
 Area Ratio: 1.01:1

| Exhaust Product | Molar Fraction | Transition Band | Vibrational Transition | $\lambda_{v'v''}$, Å | $N_{v'}$, # density of upper state, #/cm ³ | $I_{v'v''}$, watts/cm ² /ster |
|-----------------|-------------------------|---|------------------------|-----------------------|--|---|
| C ² | 4.995×10^{-14} | A ² $\pi \rightarrow X^3\Sigma$ | (0,0) | 5165.2 | 21 | 1.17×10^{-10} |
| CH | 2.176×10^{-12} | B ² $\Sigma \rightarrow X^2\Sigma$ | (0,0) | 4315.3 | 20 | 1.80×10^{-10} |
| OH | 9.062×10^{-2} | A ² $\Sigma \rightarrow X^2\Sigma$ | (0,0) | 3064 | 4.99×10^{10} | -0- |
| CO | 2.232×10^{-1} | A ¹ $\pi \rightarrow X^1\Sigma$ | (9,19) | 2455.4 | 108 | 3.376×10^{-6} |

Part B

Propellant: N₂O₄/UDMH
 O/F Ratio: 2.0
 Chamber Pressure: 100 psia
 Exhaust Pressure: 50 psia
 Exhaust Temperature: 2740°K

| | | | | | | |
|----|------------------------|---|-------|--------|--------------------|-----------------------|
| NI | 4.623×10^{-6} | A ³ $\pi \rightarrow X^3\Sigma$ | (0,0) | 3360 | 1.2×10^7 | 8.4×10^{-6} |
| NO | 1.063×10^{-2} | A ² $\Sigma \rightarrow X^2\Sigma$ | (0,0) | 2262.8 | 3.18×10^6 | 2.91×10^{-5} |
| CN | 2.841×10^{-6} | B ² $\Sigma \rightarrow X^2\Sigma$ | (0,0) | 3883.4 | 3.01×10^4 | 3.98×10^{-7} |

TABLE 7

UV-VISIBLE SECONDARY RADIATION INTENSITY AT THE MACH CONE

Propellants: LO₂/RP-1
 O/F Ratio: 3.4:1
 Chamber Pressure: 100 psia

| Exhaust Product | $\lambda_{0'v''}$ Å | Vibrational Transition | $I_{v'y''}$ watts/cm ² /ster |
|-----------------|------------------------|------------------------|--|
| C ₂ | 5160.4 | (0,0) | 5.864 x 10 ⁻¹¹ |
| | 5123.9 | (1,1) | 2.996 x 10 ⁻¹¹ |
| | 5090.4 | (2,2) | 1.368 x 10 ⁻¹¹ |
| | 4731.8 | (1,0) | 2.675 x 10 ⁻¹¹ |
| | 4708.3 | (2,1) | 4.123 x 10 ⁻¹¹ |
| | 4687.2 | (3,2) | 4.046 x 10 ⁻¹¹ |
| | 4668.4 | (4,3) | 5.102 x 10 ⁻¹¹ |
| | 4375.2 | (2,0) | 4.320 x 10 ⁻¹² |
| | 4361.4 | (3,1) | 9.355 x 10 ⁻¹² |
| | 4349.5 | (4,2) | 1.550 x 10 ⁻¹¹ |
| ----- | | | |
| CH | 3889.0 | (0,0) | 1.44 x 10 ⁻¹⁰ |
| | 3886.6 | (0,0) | -0- |
| | 3143.2 | (0,0) | -0- |
| ----- | | | |
| OH | 2806.8 | (1,0) | 1.432 x 10 ⁻² |
| | 2602.2 | (2,0) | 1.181 x 10 ⁻² |
| ----- | | | |
| CO | 2463.2 | (9,19) | 1.117 x 10 ⁻⁶ |
| | 2483.6 | (10,20) | 3.225 x 10 ⁻⁶ |

TABLE 8
IR RADIATION INTENSITY AT THE MACH CONE

Propellant: LO₂/RP-1
O/F Ratio: 3.4 (stoichiometric)
Chamber Pressure: 100 psia

| Exhaust Product | Moler Fraction | Transition Band | $\bar{\nu}$ (cm ⁻¹) | P _e psia | T _e deg. K | # density of upper state, #/cm ³ | I _v 'v" watts/cm ² /ster. | |
|--------------------|-------------------|--------------------|---------------------------------|------------------------|--------------------------|---|--|-------------------------|
| CO ₂ | 0.17990 | 010 | 000 | 667 | 50 | 2952.9 | 9.914 x 10 ¹² | 7.47 x 10 ⁻⁶ |
| CO ₂ | 0.17990 | 001 | 000 | 2349 | 50 | 2952.9 | 2.184 x 10 ¹² | 2.07 x 10 ⁻⁶ |
| CO ₂ | 0.17990 | 101 | 000 | 3715 | 50 | 2952.9 | 1.118 x 10 ¹² | 4.13 x 10 ⁻⁶ |
| CO ₂ | 0.17990 | 201 | 000 | 4978 | 50 | 2952.9 | 6.009 x 10 ¹⁰ | 1.47 x 10 ⁻⁷ |
| H ₂ O | 0.28848 | 010 | 000 | 1595 | 50 | 2952.9 | 2.99 x 10 ¹⁴ | 8.64 x 10 ⁻⁶ |
| H ₂ O | 0.28848 | 001 | 000 | 3755 | 50 | 2952.9 | 1.047 x 10 ¹⁴ | 1.83 x 10 ⁻⁶ |
| H ₂ O | 0.28848 | 011 | 000 | 5331 | 50 | 2952.9 | 4.85 x 10 ¹³ | 1.78 x 10 ⁻⁴ |
| H ₂ O | 0.28848 | 101 | 000 | 7250 | 50 | 2952.9 | 1.91 x 10 ¹³ | 1.62 x 10 ⁻⁴ |
| H ₂ O | 0.28848 | 111 | 000 | 8807 | 50 | 2952.9 | 8.95 x 10 ¹² | 4.18 x 10 ⁻⁶ |

and $\partial B/\partial T$ can be calculated from the expression given for B_v in equation (3.28). The result for the calculation $\partial B_v/\partial T$ is:

$$(\partial B_v/\partial T) = (C_2 B_v^2)/(C_1 \bar{v}^2 T^2) e^{C_2 \bar{v}/T} \quad (3.30)$$

Thus, the radiation intensity will be given by:

$$I_v = B_v [1 - C_2 B_v e^{C_2 \bar{v}/T}] / K_v C_1 \bar{v}^2 T^2 \left(\frac{\partial T}{\partial s} \right) \quad (3.31)$$

where $\partial T/\partial s$ is determined from available results for the required plume temperature distribution.

B. INSTRUMENTATION SENSITIVITY

Optical instrumentation was reviewed for sensitivity in two general ranges: the near UV-visible-near IR from 2000 to 10,000Å and the infrared from 1μ (10,000Å) to 8μ.

1. Near UV-Visible-Near IR - In the near UV (above 2000Å), in the visible and up to about 1 micron, phototubes offer the most sensitive means of detecting radiation. The sensitivity of the phototube devices will be expressed here in terms of current per unit incident radiant energy in units of amperes/watt.

There are several combinations of UV sensitive photocathodes and UV transmitting windows that cover the range between 2000Å and 4000Å. The 1P28 has an S-5 response which peaks at 3400Å with a sensitivity of 0.05 amp/watt, a current amplification of 1.25×10^6 and a Corning 9741 UV transmitting window that cuts off around 2200Å. The maximum equivalent anode dark current is about 2×10^{-12} watts with a supply voltage adjusted to give a radiant sensitivity of 0.04 amp/watt. The photocathode is Cs-Sb. The 7200 type photomultiplier is almost identical to the 1P28, except for the fact that it has a fused silica window giving it an S-19 response, with a cut off around 1700Å.

Two E.M.I. photomultipliers seem to have outstanding characteristics for the near UV region, the 6255B and the 6256B. With a photocathode sensitivity of about 0.06 amp/watt these photomultipliers have a gain of about 29×10^6 . The 6255B has an equivalent anode dark current of 2.5×10^{-14} watts at an overall voltage of 1400 volts, and the 6256B has an equivalent anode dark current of about 1.5×10^{-15} watts at an overall voltage of 1600 volts. These two tubes have fused silica windows and a spectral response of S-13 which peaks at 4400Å and covers the range from 5000Å to 1700Å. The photocathode composition for the S-13 response is Sb-Cs-O.

E.M.R., ASCOP produces photomultipliers similar to the ones manufactured by E.M.I. of Britain. Their 641B-03 Sb-Cs photocathode, 9741

glass window P.M. has a range between 2200Å and 6500Å with a peak of 4500Å. The maximum gain of the P.M. is about 10^6 , with an equivalent anode dark current input of 1.2×10^{-14} watts. A similar P.M. is the 541P-05 which has a sapphire window extending the spectral range down to 1450Å. The maximum gain for this tube is 1×10^6 , with an equivalent anode dark current input of 10^{-13} watts.

Photocathodes for visible light detection usually fall in the categories of spectral response S-11, S-17 and S-20. The quantum efficiency for S-11 is about 10 percent, and its composition is Sb-Cs-O with a photocathode sensitivity of about 0.05 amp/watt. The S-17 and S-20 cathodes have a quantum efficiency of about 15 percent, and their composition is for S-17: Cs-Sb, and for S-20: Sb-K-Na-Cs. The spectral ranges for S-11 and S-17 are from 3200Å to 6000Å with a peak at 4400Å, and for S-20 from 3200Å to 7000Å with a peak at about 4000Å.

A particularly suitable photomultiplier for the visible is the E.M.I. 9558B, S-20. It has a quantum efficiency of 20 percent, with a photocathode sensitivity of about 0.1 amp/watt. The maximum gain is 3.5×10^6 , and at a gain of 1.4×10^6 the equivalent anode dark current input is about 10^{-15} watts.

Photomultipliers with sensitivity in the infrared up to 1μ have an S-1 response, with the photocathode composed of Ag-O-Cs. The S-1 curve peaks at 8500Å with a quantum efficiency of 0.5 percent and a sensitivity of 0.003 amperes/watt. It covers a range between 6000Å and 10,000Å. A particularly suitable photomultiplier for the near infrared is the I.T.T. built FW118. It has a cathode radiant sensitivity of 0.0022 amp/watt, a gain of 10^7 and an equivalent anode dark current input of about 10^{-10} watts.

The signal produced by a photomultiplier has already been considerably amplified by the electron secondary emission process taking place between the cathode and anode electrodes. The output signal can be measured by using a load resistor at the anode and measuring the voltage drop across it, or by using a cathode follower for impedance matching at the output and measuring the cathode follower output. The basic limitation in measuring low radiant fluxes is the noise level of the tube. To achieve low noise, low gain is required (low overall voltage) and therefore, the lowering of the anode sensitivity. A compromise usually has to be worked out between signal strength (which depends on gain) and a tolerable noise level.

2. Infrared from 1-8μ - Before discussing infrared detectors for the 1-8μ range, it is necessary to define the system under which these detectors are to be compared. The magnitude of the response related to the quantity of incident radiation is called the responsivity and is given by:

$$R(\lambda, f, A_d) d\lambda = S(\lambda, f, A_d) d\lambda / W(\lambda) \quad (3.32)$$

where $W(\lambda)$ = incident radiation in joules, watts, photons
or photons/sec
 S = detector output (response)

The detectivity is defined as the signal-to-noise ratio per unit quantity of incident radiation, given by:

$$D(\lambda, f, \Delta f, A_d) d\lambda = R(\lambda, f, A_d) d\lambda / N(f, \Delta f, A_d) = \frac{S(\lambda, f, A_d) d\lambda}{W(\lambda) N(f, \Delta f, A_d)} \quad (3.33)$$

where D is in units of (joules) $^{-1}$, or (watts) $^{-1}$ or (# of photons) $^{-1}$ or (# of photons/sec) $^{-1}$. The reciprocal of the detectivity is the noise-equivalent power.

$$P_n(\lambda, f, \Delta f, A_d) \equiv 1/D \quad (3.34)$$

The detectivity of a detector reduced to a sensitive area of 1 cm² and measured with a bandwidth of 1 cps is called the specific detectivity and is useful for intercomparison among various detectors. The specific detectivity is given by:

$$D^* \equiv D A_d^{1/2} (\Delta f)^{1/2} \text{cm-cps}^{1/2} \text{-(watt)}^{-1} \quad (3.35)$$

and is denoted in the general case by $D^*(\lambda, f, T_d)$.

It is useful to establish the limitations to the detection of small signals set by ultimate physical conditions external to the detector itself. The condition of operation of a detector under background photon noise limitations has been termed the BLIP (for background-limited infrared photoconductor) condition.

$$D^*_{\text{BLIP}}(\lambda_c, 0) = D^*_{\text{BLIP}}(\lambda_c, 2\pi) \csc(\theta/2) \quad (3.36)$$

where λ_c is the long wavelength cutoff. A specific BLIP detectivity is defined with reference to a detector exposed to 2π steradians solid angle of background radiation. It is given in terms of D by:

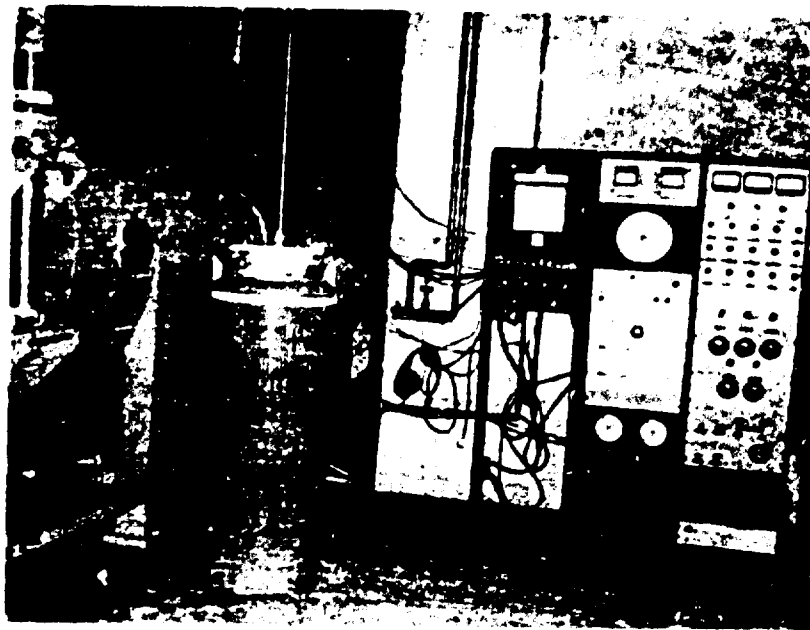
$$D^*_{\text{BLIP}} \equiv D A_d^{1/2} (\Delta f)^{1/2} \sin(\theta/2) \quad (3.37)$$

Present day infrared detectors in the operational stage include a variety of photosensitive elements: PbS, PbSe, PbTe, InSb, Ge:As, Ge:(Au,Sb), Ge:Cu, Ge:Zn, InAs, thermistor bolometers, galav cells, thermocouples, and carbon bolometers.

The principles of operation of the photosensitive detectors employing such elements as listed above are: thermal detectors and photon detectors. The photon detectors can operate as photoconductors, photovoltaic detectors, and photoelectromagnetic detectors.

For the range of interest here, 1-8 μ , the Au doped germanium detectors appear to provide the best specific detectivity coupled to a time response of less than a microsecond. The cooling required is at

a temperature of 77°K, the boiling temperature of liquid nitrogen. The usual angle of the field of view is about 60°.



FIGURES 7 and 8. VIEWS OF DYNAMIC VACUUM FACILITY NO. 2

SECTION 4

ROCKET ENGINE ANALYSIS

This section presents an analysis of the factors influencing a rocket engine design capable of providing the necessary radiation signal strength and compatible with the volumetric capacity of the vacuum facility to be used for testing. In a program designed to study the characteristics of a rocket plume under simulated space conditions a certain interdependency exists among the capabilities of the rocket engine, the test facility and the optical monitoring instrumentation. Ideally, one would design a rocket engine for a very low flow rate requiring a minimum vacuum facility investment, since the facility is the major cost element in the program. But this approach would require very sensitive radiation instrumentation, which would then become the ultimate limiting factor in reduction of engine flow rate, and would not consider the simulation characteristics of the engine. Hence, as a result, the vacuum facility must be sized to the minimum engine flow which is satisfactory from a simulation standpoint and yet provides a detectable signal.

A. FLOW RATE VERSUS ALTITUDE

The subscale engine techniques developed on previous contracts at this corporation (see Appendix C) provide good radiation simulation (as evidenced by comparison with Project RAMP data) with very low flows of 0.1 gm/sec or less. The ultimate limitation on reduction of engine flow from this viewpoint remains to be determined, but it is probably governed by the ability to avoid excessive nozzle heat transfer and to compensate for boundary layer effects. However, in order to initiate the necessary tradeoff study among the three prime parameters noted above, the vacuum facility and radiation instrumentation requirements will be examined initially on the basis of rocket engine flow rates in the range 0.1 gm/sec. This was the same value used to compute radiation intensity.

1. Facility Description - The vacuum system to be used for experimental verification of the analysis conducted under this program is shown in Figures 7-11. The main chamber measures six feet in diameter and twelve feet in length. It is provided with six viewing ports along the side spaced at two foot intervals; three viewing ports along the top—one at either end and one four feet from the working end; and four ports located at both ends of the tank positioned at 45° angles to the horizontal plane. These latter ports are one foot from the forward end and one foot from the aft end. The ports consist of 9" flanges with "O" ring grooves machined into them. The actual openings into the tank through these ports are 4" in diameter. To insure that the top and side ports are mutually perpendicular and that the ports at 45° to the horizontal are properly located, the entire tank was placed in a large surface grinder after the port flanges were welded and all of the flanges were then ground while the tank was accurately rotated in the grinder.

The forward end bell of the tank is detachable and swings away from

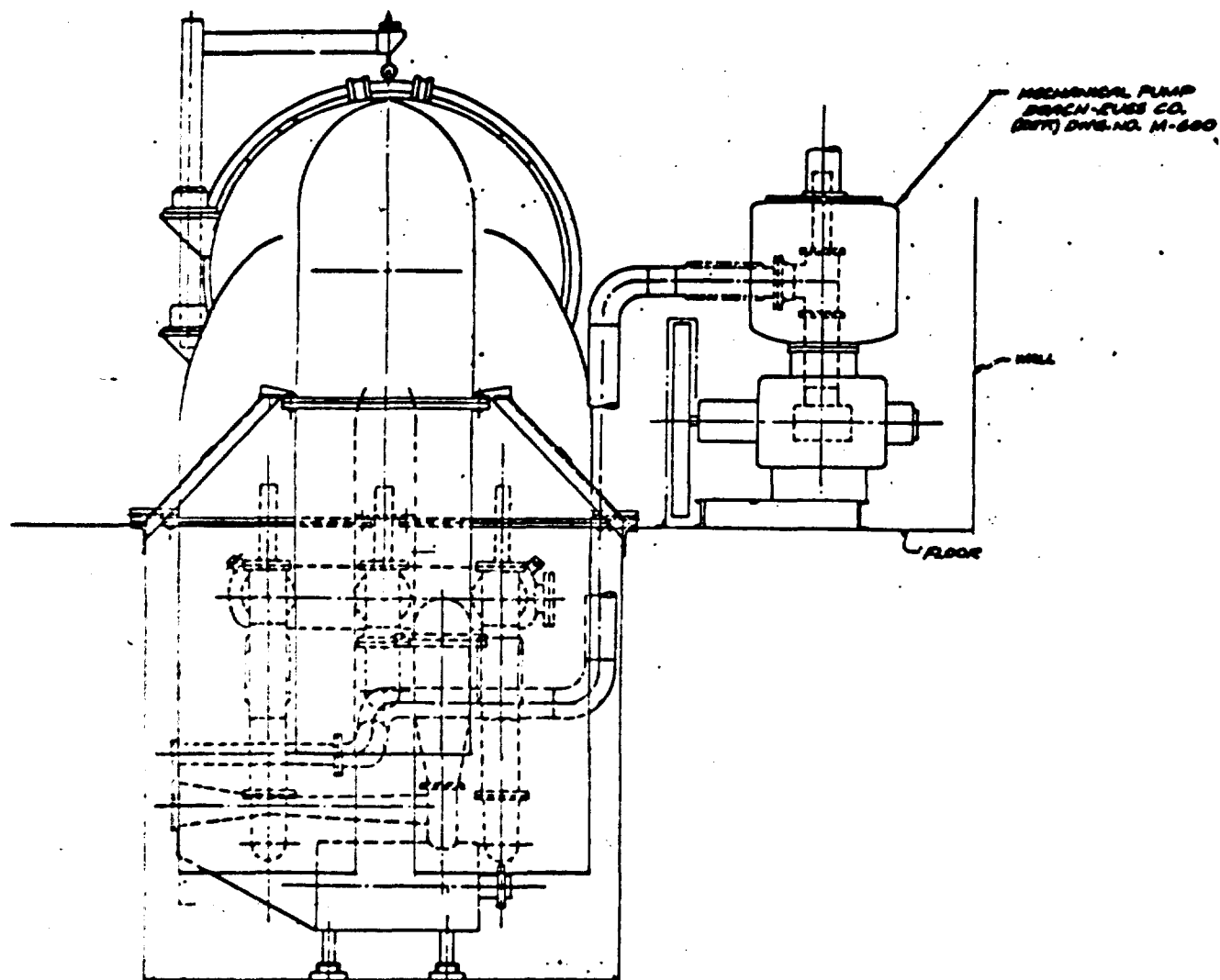


Figure 9. Dynamic Vacuum Facility
Front Elevation

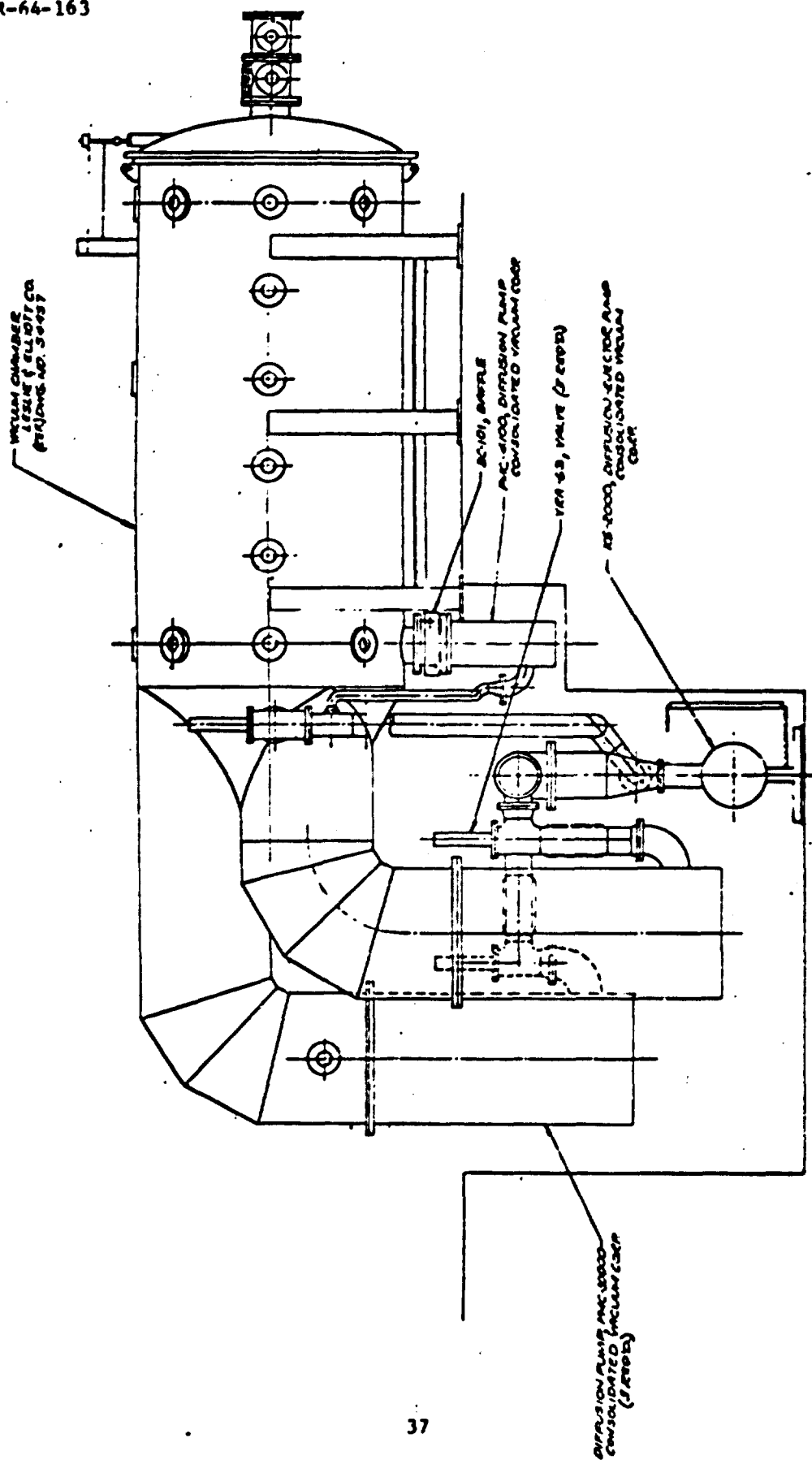


Figure 10. Dynamic Vacuum Facility
Side View

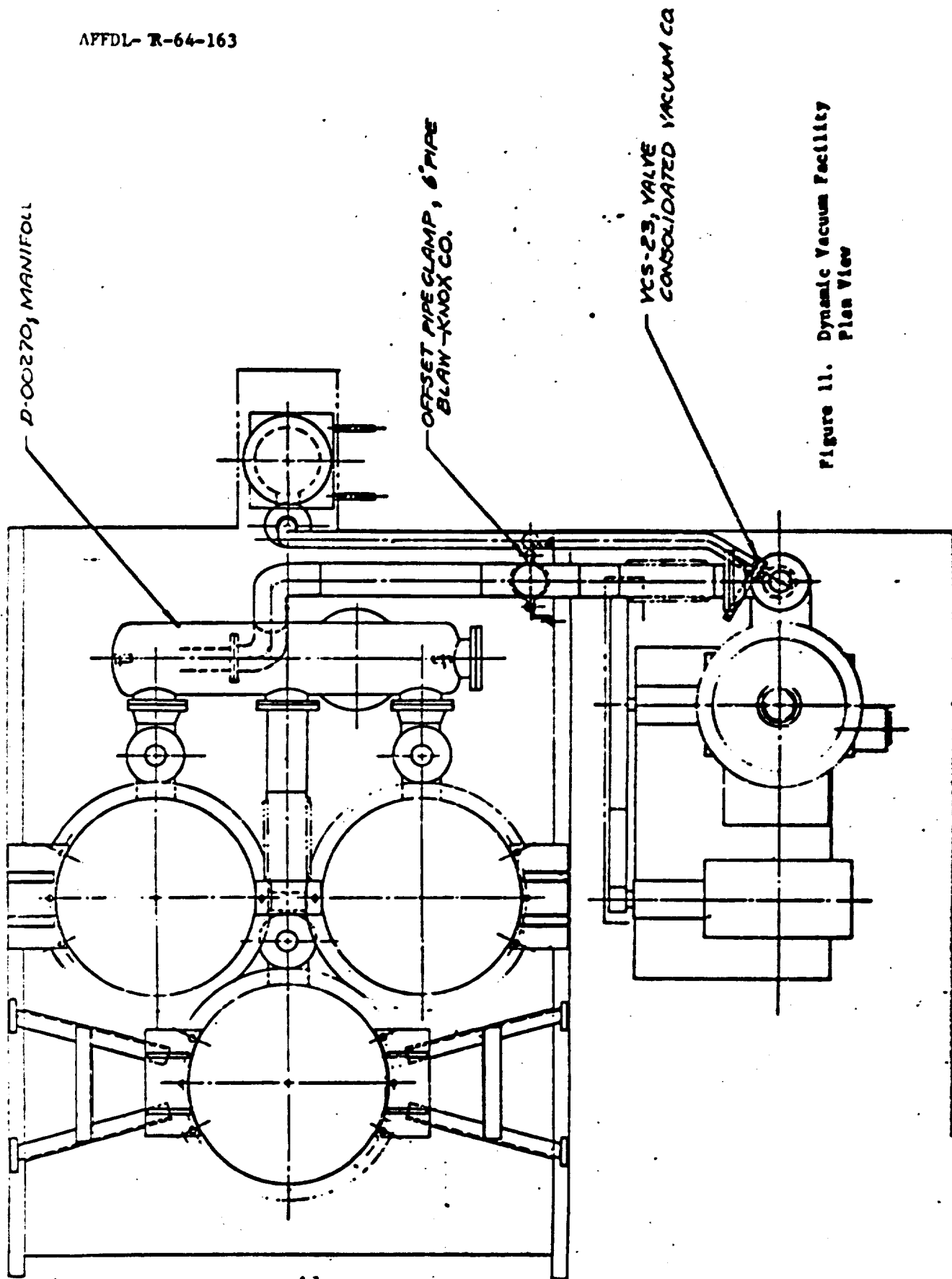


Figure 11. Dynamic Vacuum Facility
Plan View

the main chamber on a davit which is permanently attached to the tank. This design allows access to the entire six foot diameter of the tank which facilitates installation and operation of the optical collecting system. The end bell is sealed to the tank by means of an "O" ring which is 74 inches in diameter; swing bolts clamp the end bell to the tank. The port located in the center of the end bell of the tank is one foot in diameter and has an "O" ring groove machined into it. This is the port through which the rocket engine is fired.

At the aft end of the main chamber is a permanently attached water cooled manifold which communicates to three 32 inch diameter diffusion pumps. These pumps were manufactured by the Consolidated Vacuum Corporation and are their type PMC-50000. These pumps are connected to an oil ejector pump by means of a manifold. The oil ejector pump was also manufactured by the Consolidated Vacuum Corporation and is their type KS2000. The oil ejector pump is connected to a mechanical pump which was manufactured by Beach-Russ and is their type RP-Model 375. The location of these devices is evident from the three views of the facility presented.

A liquid nitrogen cryogenic baffle (or cold trap) is located within the vacuum tank at the aft end just upstream of the diffusion pump elbow inlets. This baffle serves the dual purpose of trapping heavy rocket exhaust gas particles such as CO_2 and H_2O and preventing oil backflow from the diffusion pumps. The baffle is fabricated of low carbon stainless steel (type 316) to insure against the formation of latent leaks which would otherwise appear after repeated thermal cycling. The chevron is non-amealed sheet and the liquid nitrogen tubing which is fusion welded to the sheet is 3/8 inch seamless with an 0.049 inch wall. Design provisions have been made in the baffle assembly for thermal expansion and contraction.

Four 6 inch vacuum valves are employed to control vacuum in the tank-pump system. Three of these valves are located one each at the outlet of the three diffusion pumps, and the fourth is at the inlet to the mechanical pump. By proper manipulation of these valves, the mechanical pump and the ejector pump can be isolated from the system and the three diffusion pumps can each be isolated from the ejector pump. However, the diffusion pumps cannot be isolated from each other at the inlets. The physical location of these valves is shown on the three views of the facility.

The vacuum instrumentation employed in this facility consists of four thermocouple vacuum gauges and two ionization vacuum gauges. The thermocouple gauges are located as follows:

- inlet of the mechanical pump
- inlet of the oil ejector pump
- aft end of the main chamber
- fore end of the main chamber

The ionization gauges are located as follows:

aft end of the main chamber
fore end of the main chamber

The thermocouple gauges were manufactured by Hastings-Raydist and are their type DV-3. The ionization gauges were manufactured by Veeco and are their type RG-75P. The thermocouple and ionization gauges are readout on a Cook Vacuum Gauge Unit Model CD-22.

2. Total Gas Load on Systems - The ultimate pressure which can be attained by the vacuum facility will be a function of the effective pumping speed of the facility and the total gas load on the system, which in turn is dependent on the type(s) of propellants selected for test. Considering initially the total gas load on the system, the following equation can be derived from a material balance on the system:

$$V_1 \frac{dP}{dt} + SP = Q_{\text{const}} + Q(t) \quad (4.1)$$

where: V_1 is the volume of the chamber in liters
 P is the pressure in torr (or mm Hg)
 t is the time in seconds
 S is the total effective pumping speed (or conductivity) of the system in liters/sec
 Q_{const} is the gas load due to leaks and engine flow in t-l/s
 $Q(t)$ is the time-dependent gas load due to outgassing in the system in t-l/s.

The solution of the equation⁹ can be written:

$$P(t) = \left(P_1 - \frac{Q_{\text{const}}}{S} \right) e^{\left(\frac{S}{V_1} t \right)} + \frac{Q_{\text{const}}}{S} + \frac{1}{V_1} e^{\left(\frac{S}{V_1} t \right)} \int_0^t Q(t) e^{\left(+ \frac{S}{V_1} \right) dt} \quad (4.2)$$

The third term may be integrated by expanding $Q(t)$ in a Taylor's series and the equation written in general form as:

$$P(t) = K e^{\left(- \frac{S}{V_1} t \right)} + \frac{Q_{\text{const}}}{S} + M(t) \quad (4.3)$$

where: $K = P_1 - \left(\frac{Q_{\text{const}}}{S} \right) + X$

$$M(t) = \sum_{n=0}^{\infty} a_n t^n$$

$X = \text{a constant}$

The first term of equation (4.3) will disappear in the order of 100 to 1000 seconds since S/V_1 will be in the range of 1 to 1/100. Experience with our present large carbon-steel tank system indicates that the third term containing the time-dependent outgassing function will dis-

appear in the order of 5 to 10 hours (the tank has been pumped to a steady pressure of 2×10^{-6} torr in 5 hours). Thus, after 5 to 10 hours the ultimate steady pressure in the system would be Q_{const}/S . The Q_{const} will be composed of tank leaks (Q_L) and the rocket flow (Q_R). The amount of Q_L can be estimate from tests to be about 0.07 torr-liters/sec or approximately 2×10^{-4} standard cubic feet per minute at 273°K and 1 atm (SCFM).

The values of Q due to rocket flow can be calculated as follows:

$$Q = P\dot{V} = \dot{n} RT = \frac{\dot{W}}{\bar{M}} RT = 62.4 \dot{W} \frac{T}{\bar{M}} \quad (4.4)$$

where: Q is the gas load, torr-liters/sec
 \dot{W} is the weight flow rate, gm/sec
 T is the static gas temperature, °K
 \bar{M} is the average gas molecular weight, gm/gm-mol

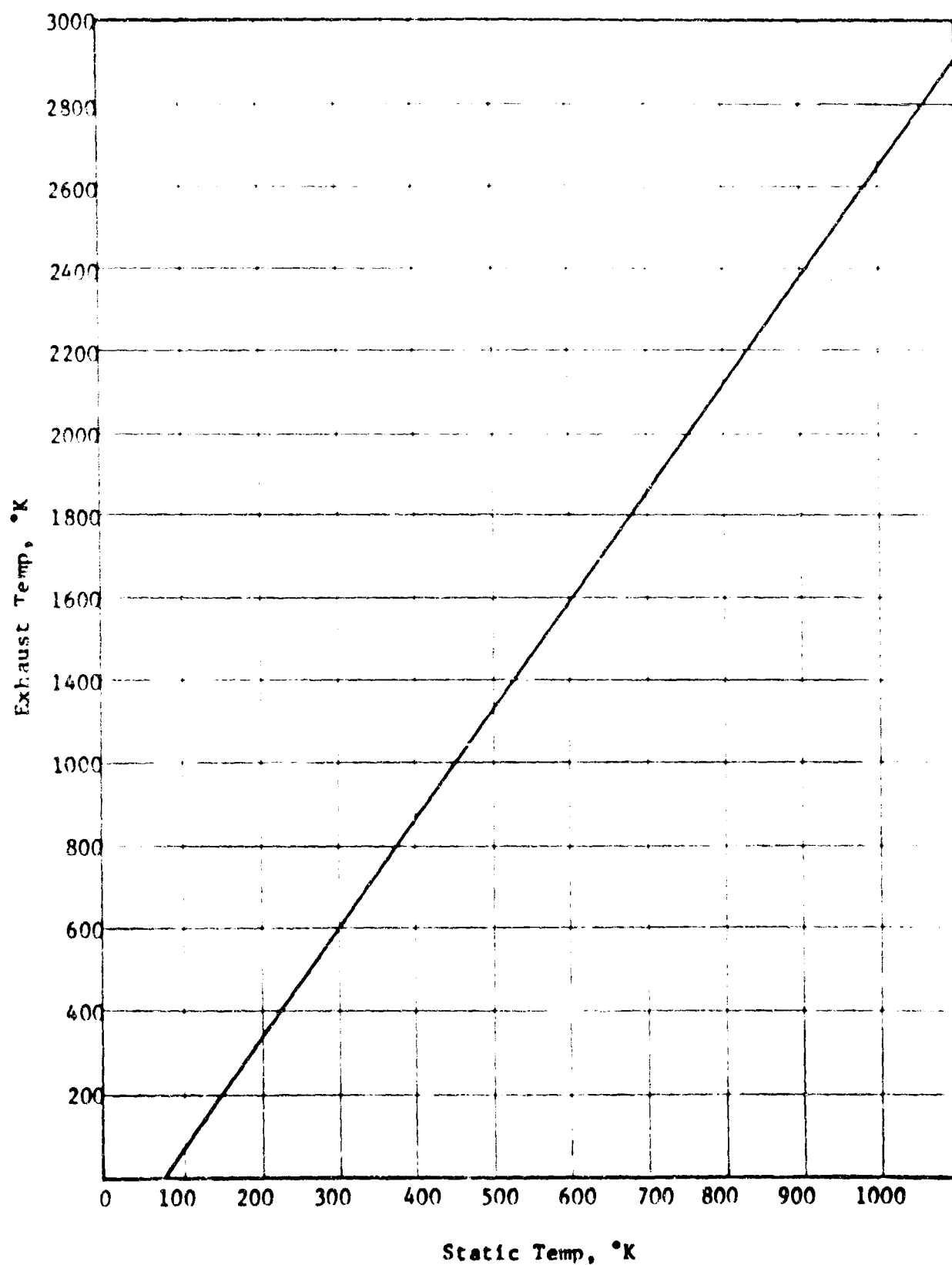
A convenient conversion factor is:

$$Q_{\text{SCFM}} = 0.174 \dot{W} \frac{T}{\bar{M}} \quad (4.5)$$

Actual gas loads may now be calculated for the three propellant systems selected for analysis. However, before so doing two things must be kept in mind. First, the static gas temperature to be used in the calculation is the temperature at the diffusion pump inlet downstream of the cryogenic baffle. This temperature can be closely estimated from past tests conducted by this corporation in the facility previously described under contracts listed in Appendix C hereto. The static gas temperature is shown as a function of exhaust gas temperature in Figure 12. Secondly, the weight flowrate is also assumed to be that which reached the diffusion pumps and must be reduced by the proportion of exhaust constituent which will adhere to the baffle. Figure 13 presents the vapor pressure curves of various substances as a function of temperature^{10,11}. Since it is known that the maximum altitude for testing need not exceed that which is sufficient to provide free molecular flow (i.e. test pressure will be 5×10^{-4} - 5×10^{-3}), and the cryogenic baffle when LN₂ cooled will be at a temperature of 80°K, it can then be seen from Figure 13 that H₂O and CO₂ will stick to the baffle and not reach the diffusion pumps. Past tests have shown that sticking factors are close to one under these conditions.

Employing the data presented for O₂/H₂ in Section 2, a family of curves was constructed during the course of this program as shown in Table 3A and Figure 14) which describe the full range of operating conditions anticipated during rocket tests and how they affect gas load on the vacuum systems. This unique analysis was required to determine the capability of the vacuum system to be used for test over a range of rocket engine operating conditions not previously investigated by this corporation. This information is presented for O₂/RP-1 and N₂O₄/UDMH in Tables 9 and 10 and Figures 15 and 16.

FIGURE 12. ROCKET ENGINE EXHAUST GAS TEMPERATURE VS
DIFFUSION PUMP INLETS STATIC GAS
TEMPERATURE (AFTER COOLING)



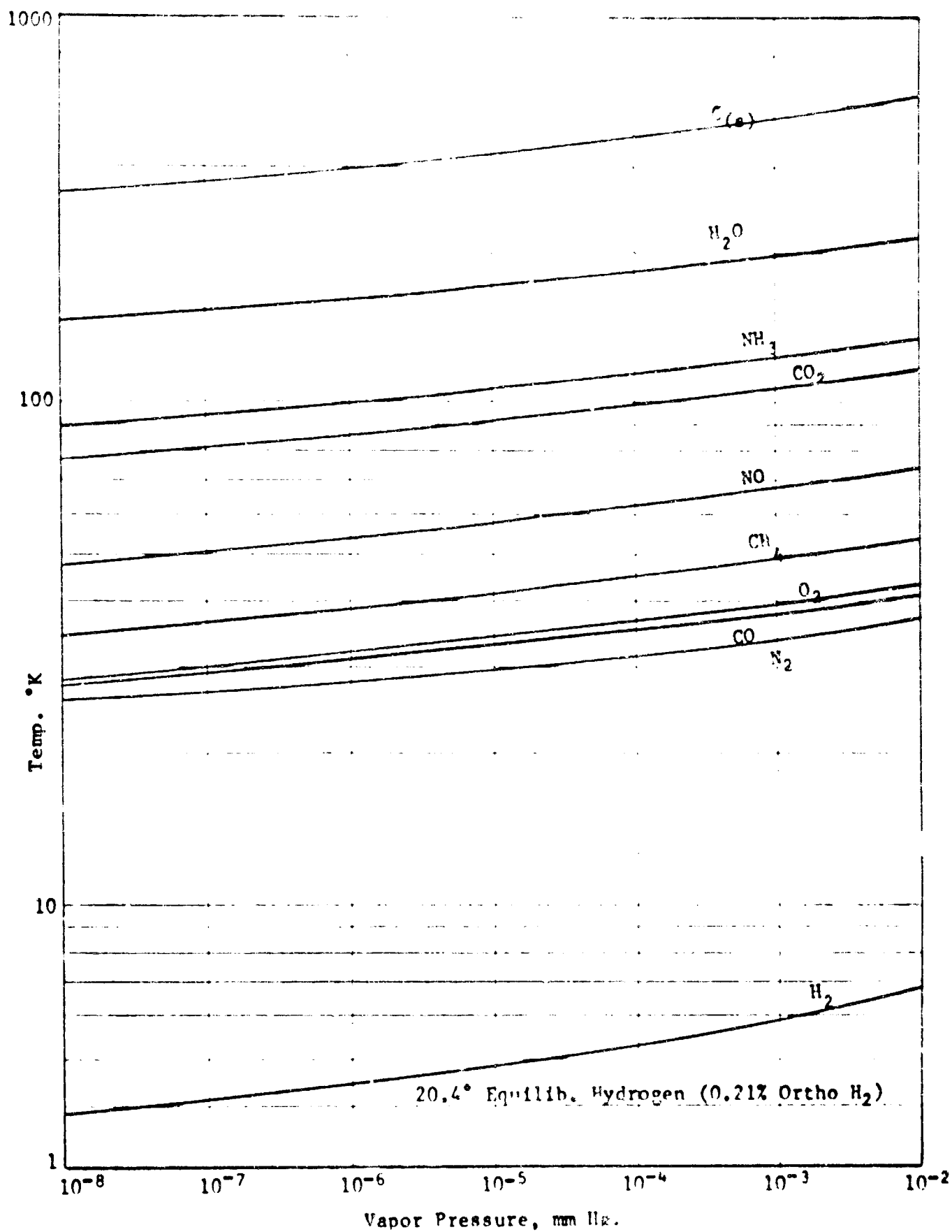


Figure 13. Vapor Pressure of Some Exhaust Gas Constituents vs Temperature

TABLE 8A

OXYGEN-HYDROGEN GAS LOAD ON VACUUM SYSTEMS
AS A FUNCTION OF MIXTURE RATIO AND EXPANSION RATIO
(FRCZEN CONDITIONS, $P_c = 60$ PSIA)

| Case No. | Expansion Ratio | Exhaust Temp. | Cooled Gas Temp. | Total Gas Load | Gas Load on Pumps |
|----------|-----------------|--------------------|--------------------|----------------|-------------------|
| | A_e/A_t | $^{\circ}\text{K}$ | $^{\circ}\text{K}$ | SCFM | SCFM |
| A | 1.0 | 1008 | 375 | 1.48 | 1.26 |
| | 2.0 | 643 | 240 | 0.95 | 0.80 |
| | 4.0 | 439 | 175 | 0.69 | 0.59 |
| | 8.0 | 340 | 130 | 0.51 | 0.44 |
| | 15.0 | 270 | 105 | 0.41 | 0.35 |
| | 40.0 | 175 | 60 | 0.24 | 0.20 |
| B | 1.0 | 2065 | 790 | 1.81 | 1.18 |
| | 2.0 | 1470 | 520 | 1.19 | 0.77 |
| | 4.0 | 1135 | 415 | 0.95 | 0.62 |
| | 8.0 | 900 | 330 | 0.76 | 0.49 |
| | 15.0 | 700 | 270 | 0.62 | 0.40 |
| | 40.0 | 460 | 180 | 0.41 | 0.27 |
| C | 1.0 | 2715 | 1010 | 1.58 | 0.71 |
| | 2.0 | 2005 | 750 | 1.18 | 0.53 |
| | 4.0 | 1620 | 600 | 0.94 | 0.42 |
| | 8.0 | 1300 | 490 | 0.77 | 0.35 |
| | 15.0 | 1103 | 410 | 0.64 | 0.29 |
| | 40.0 | 800 | 300 | 0.47 | 0.21 |

TABLE 8A (continued)

| Case No. | Expansion Ratio | Exhaust Temp. | Cooled Gas Temp. | Total Gas Load | Gas Load on Pumps |
|----------|-----------------|---------------|------------------|----------------|-------------------|
| D | 1.0 | 2912 | 1080 | 1.22 | 0.44 |
| | 2.0 | 2220 | 820 | 0.94 | 0.34 |
| | 4.0 | 1815 | 670 | 0.77 | 0.28 |
| | 8.0 | 1440 | 560 | 0.64 | 0.23 |
| | 15.0 | 1255 | 470 | 0.54 | 0.19 |
| | 40.0 | 945 | 350 | 0.39 | 0.14 |

* Case A $O/F = 1.2$, $\bar{M} = 4.42$, $\%H_2O = 15$
 B $O/F = 2.8$, $\bar{M} = 7.60$, $\%H_2O = 35$
 C $O/F = 4.8$, $\bar{M} = 11.14$, $\%H_2O = 55$
 D $O/F = 7.9$, $\bar{M} = 15.40$, $\%H_2O = 64$

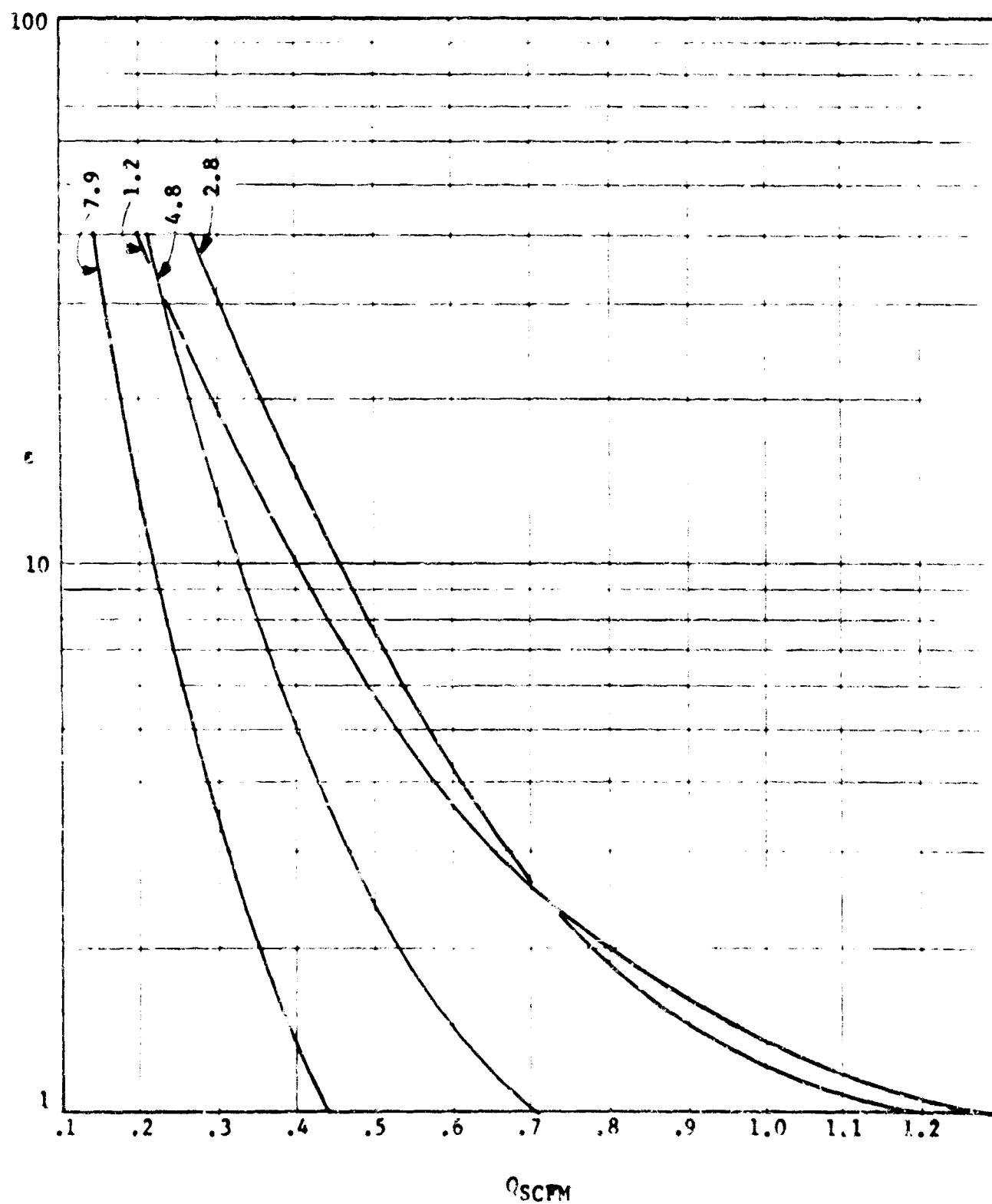


Figure 14. Oxygen-Hydrogen Gas Load on Vacuum System as a Function of Expansion Ratio and Mixture Ratio

TABLE 9
OXYGEN-RP-1 GAS LOAD ON VACUUM
SYSTEMS AS A FUNCTION OF MIXTURE RATIO AND EXPANSION RATIO
(FROZEN CONDITIONS, $P_c = 50$ PSIA)

| Case No. | Expansion Ratio | Exhaust Temp. | Cooled Gas Temp. | Total Gas Load | Gas Load on Pumps |
|----------|-----------------|---------------|------------------|----------------|-------------------|
| | A_e/A_t | $^{\circ}K$ | $^{\circ}K$ | SCFM | SCFM |
| A | 1.0 | 2590 | 970 | 0.88 | 0.65 |
| | 2.0 | 1780 | 670 | 0.61 | 0.45 |
| | 4.0 | 1480 | 560 | 0.50 | 0.37 |
| | 8.0 | 1260 | 475 | 0.43 | 0.32 |
| | 15.0 | 1090 | 410 | 0.37 | 0.27 |
| | 40.0 | 865 | 330 | 0.30 | 0.22 |
| B | 1.0 | 2785 | 1040 | 0.84 | 0.52 |
| | 2.0 | 2000 | 750 | 0.61 | 0.38 |
| | 4.0 | 1700 | 640 | 0.52 | 0.32 |
| | 8.0 | 1440 | 540 | 0.44 | 0.27 |
| | 15.0 | 1240 | 470 | 0.38 | 0.24 |
| | 40.0 | 985 | 375 | 0.31 | 0.19 |
| C | 1.0 | 2810 | 1055 | 0.82 | 0.48 |
| | 2.0 | 2050 | 770 | 0.60 | 0.35 |
| | 4.0 | 1740 | 655 | 0.51 | 0.30 |
| | 8.0 | 1490 | 565 | 0.44 | 0.26 |
| | 15.0 | 1300 | 490 | 0.38 | 0.22 |
| | 40.0 | 1050 | 400 | 0.31 | 0.18 |

TABLE 9 (continued)

| Case No. | Expansion Ratio | Exhaust Temp. | Cooled Gas Temp. | Total Gas Load | Gas Load on Pumps |
|----------|-----------------|---------------|------------------|----------------|-------------------|
| D | 1.0 | 3200 | 1210 | 0.89 | 0.51 |
| | 2.0 | 2160 | 810 | 0.60 | 0.34 |
| | 4.0 | 1800 | 660 | 0.49 | 0.28 |
| | 8.0 | 1550 | 585 | 0.43 | 0.25 |
| | 15.0 | 1350 | 510 | 0.38 | 0.22 |
| | 40.0 | 1080 | 410 | 0.30 | 0.17 |

* Case A $O/F = 1.80$, $\bar{M} = 19.23$, $\%H_2O = 21$, $\%CO_2 = 5$
 B $O/F = 2.35$, $\bar{M} = 21.50$, $\%H_2O = 27$, $\%CO_2 = 11$
 C $O/F = 2.65$, $\bar{M} = 22.45$, $\%H_2O = 28$, $\%CO_2 = 13$
 D $O/F = 3.10$, $\bar{M} = 23.60$, $\%H_2O = 28$, $\%CO_2 = 15$

TABLE 10
 N_2O_4 -UDMH GAS LOAD ON VACUUM SYSTEMS
 AS A FUNCTION OF MIXTURE RATIO AND EXPANSION RATIO
 (FROZEN CONDITIONS, $P_c = 60$ PSIA)

| Case No. | Expansion Ratio | Exhaust Temp. °K | Cooled gas Temp. °K | Total Gas Load SCFM | Gas Load on Pumps SCFM |
|----------|-----------------|---------------------|------------------------|------------------------|---------------------------|
| * A | A_e/A_t | °K | °K | SCFM | SCFM |
| | 1.0 | 2400 | 900 | .83 | .63 |
| | 2.0 | 1750 | 655 | .61 | .46 |
| | 4.0 | 1350 | 510 | .48 | .36 |
| | 8.0 | 1040 | 395 | .37 | .28 |
| | 15.0 | 820 | 310 | .29 | .22 |
| B | 40.0 | 570 | 220 | .21 | .16 |
| | 1.0 | 2780 | 1040 | .82 | .50 |
| | 2.0 | 2050 | 770 | .61 | .38 |
| | 4.0 | 1650 | 625 | .49 | .30 |
| | 8.0 | 1330 | 505 | .40 | .25 |
| | 15.0 | 1080 | 410 | .32 | .20 |
| C | 40.0 | 800 | 305 | .24 | .15 |
| | 1.0 | 2800 | 1050 | .79 | .47 |
| | 2.0 | 2120 | 800 | .60 | .35 |
| | 4.0 | 1700 | 640 | .48 | .28 |
| | 8.0 | 1360 | 510 | .38 | .22 |
| | 15.0 | 1120 | 425 | .32 | .19 |
| | 40.0 | 815 | 315 | .24 | .14 |

TABLE 10 (continued)

| Case No. | Expansion Ratio | Exhaust Temp. | Cooled Gas Temp. | Total Gas Load | Gas Load on Pumps |
|----------|-----------------|---------------|------------------|----------------|-------------------|
| D | 1.0 | 2800 | 1050 | .73 | .43 |
| | 2.0 | 2120 | 800 | .56 | .33 |
| | 4.0 | 1700 | 640 | .45 | .27 |
| | 8.0 | 1360 | 510 | .36 | .21 |
| | 15.0 | 1120 | 425 | .30 | .18 |
| | 40.0 | 815 | 315 | .22 | .13 |
| E | 1.0 | 2650 | 995 | .66 | .40 |
| | 2.0 | 2000 | 750 | .49 | .29 |
| | 4.0 | 1600 | 600 | .40 | .24 |
| | 8.0 | 1280 | 480 | .32 | .19 |
| | 15.0 | 1050 | 400 | .26 | .16 |
| | 40.0 | 765 | 290 | .19 | .11 |

* Case A $O/F = 1.5$, $\bar{M} = 18.68$, $\%H_2O = 21$, $CO_2 = 3$
 B $O/F = 2.3$, $\bar{M} = 22.08$, $\%H_2O = 31$, $CO_2 = 7$
 C $O/F = 2.75$, $\bar{M} = 23.38$, $\%H_2O = 32$, $CO_2 = 9$
 D $O/F = 3.5$, $\bar{M} = 24.98$, $\%H_2O = 30$, $CO_2 = 11$
 E $O/F = 4.5$, $\bar{M} = 26.46$, $\%H_2O = 28$, $CO_2 = 12$

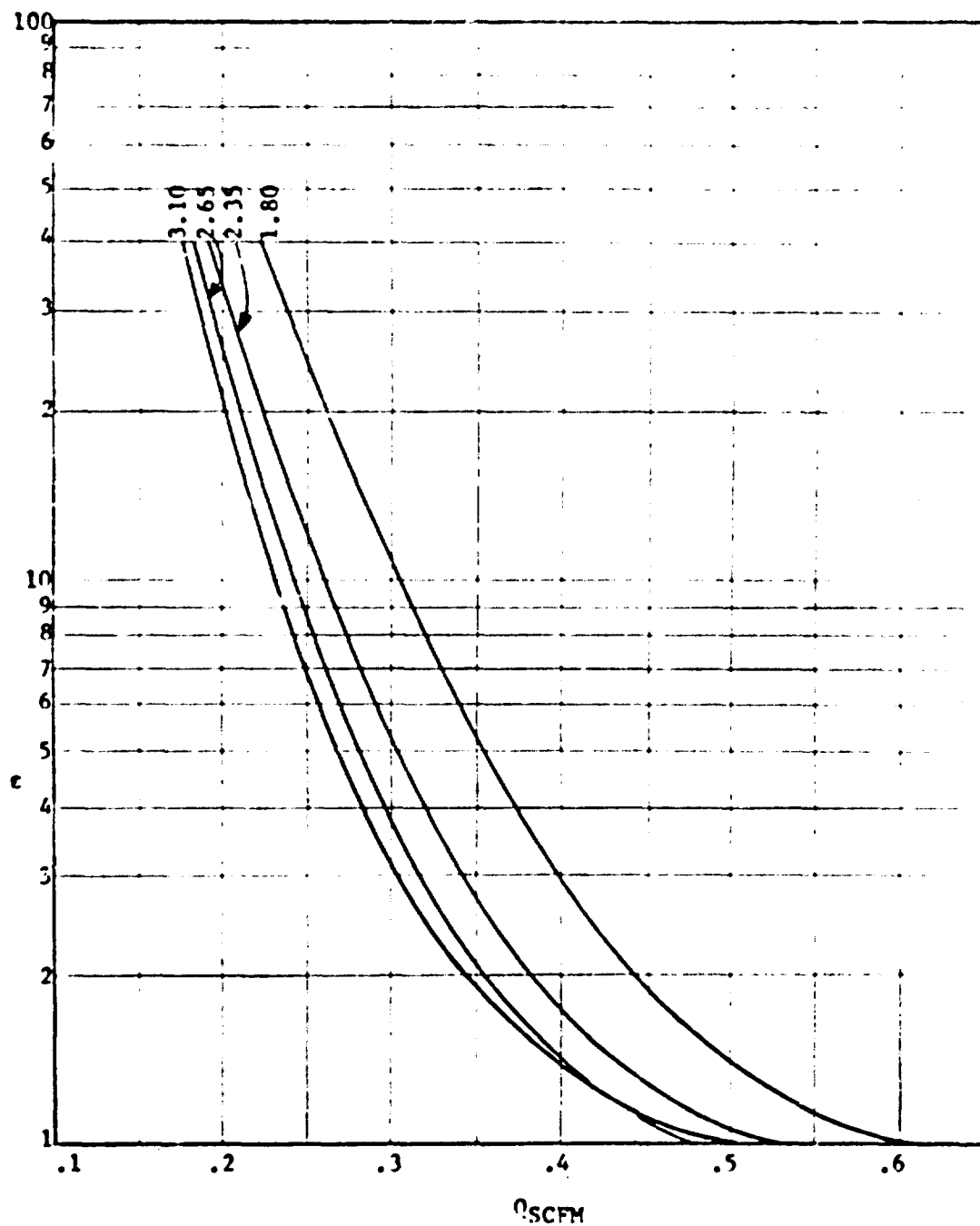


Figure 15. Oxygen - RPM Gas Load on Vacuum System as a Function of Expansion Ratio and Mixture Ratio

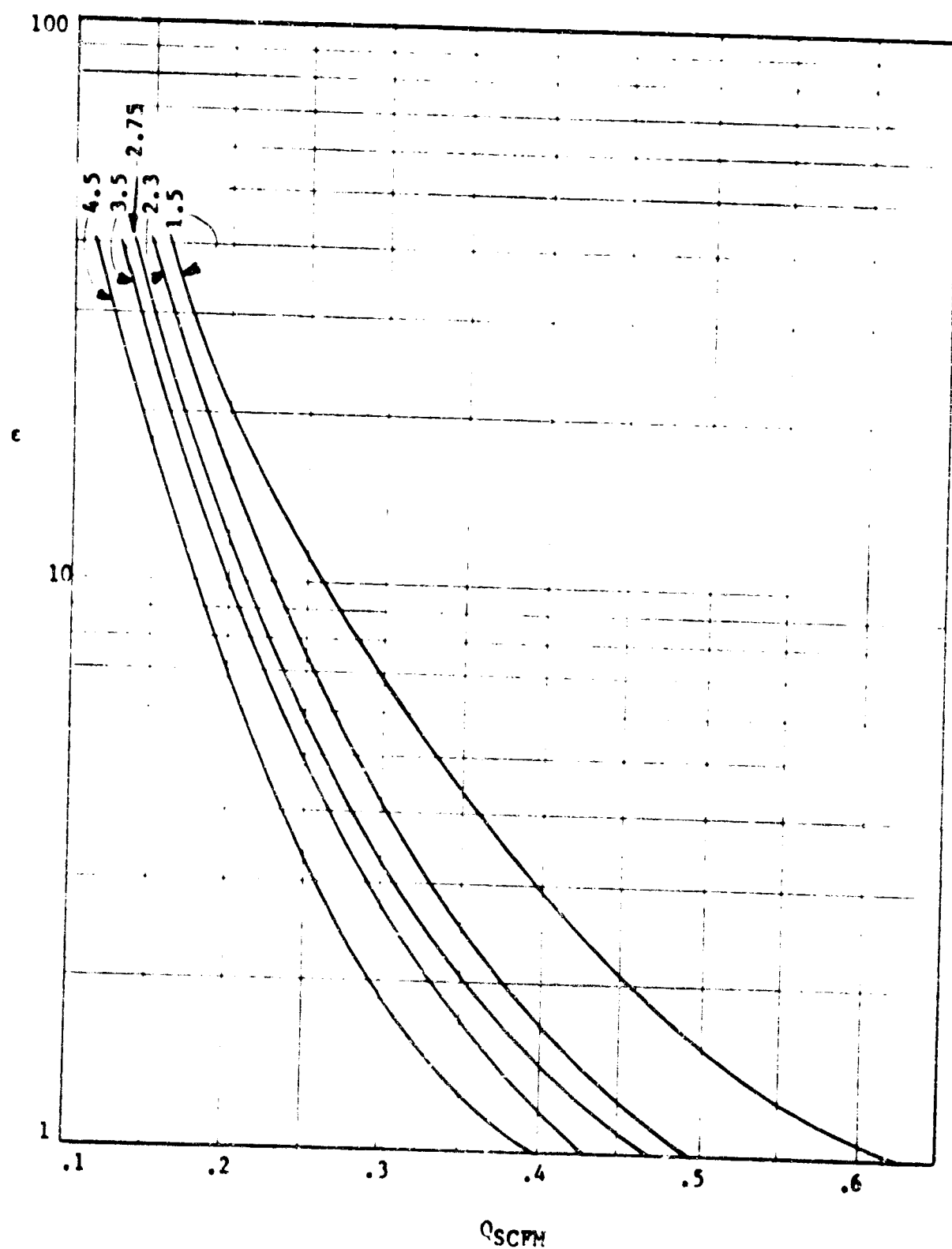


Figure 16. N_2O_4 - UDMH Gas Load on Vacuum System as a Function of Expansion Ratio and Mixture Ratio

3. Effective Pumping Speed of System - The effective pumping speed of the vacuum system is determined by the speed of the pumping system and the conductance of the lines leading to the pumping system. Thus, the speed or volumetric flow capacity of the system can be calculated as:

$$\frac{1}{S} = \frac{1}{C_l} + \frac{1}{C_b} + \frac{1}{S_p} \quad (4.6)$$

where: S is the effective speed of the system
 C_l is the conductance of the lines
 C_b is the conductance of the cryogenic baffle
 S_p is the speed of the pumps

The speed of Astrosystems pumping equipment is shown in Figure 17 for calibrations with air at 520°R (289°K). This curve in effect describes the speed of the overall system (S). It can be seen that the most efficient operating point for high altitude testing is between 300,000 and 340,000 feet ($P_a = 1 \times 10^{-3}$ to 1×10^{-4}).

The pumping speed of an oil diffusion pump can be calculated as follows:

$$S_d = \frac{2}{3} v_a \pi a^3 / l \quad (4.7)$$

where: v_a = average velocity of pumped molecules
 a = radius of the pump inlet port
 l = length of inlet port

This equation assumes correct inlet port design which is true for this case. The velocity of a gas molecule in free molecular flow is described by the following equation:

$$v_a = 1.455 \times 10^4 \left(\frac{T}{M} \right)^{1/2} \quad (4.8)$$

Hence, the diffusion pump speed for a constant inlet geometry and at a specific pressure is dependent only on the factor $\left(\frac{T}{M} \right)^{1/2}$.

The above factor can be calculated for the calibration conditions shown in Figure 17 to be 3.2. The same factor can be calculated for each condition being analyzed for experimental study from Tables 8-10. By ratio of these values to the above value a pumping capability can be established for each test condition employing the calibrated flow rate of 0.1 SCFM shown in Figure 17. These results are presented in Tables 11-13 in comparison with actual gas load as previously determined.

The resulting values indicate a need to reduce flow in most test cases; however, in the regions of most interest (large expansion ratio and near-optimum mixture ratio), capability and calculated gas load are closely matched for the assumed flow rate. It, therefore, appears advisable to design the test engine for a nominal flow rate of 0.1 gm/sec

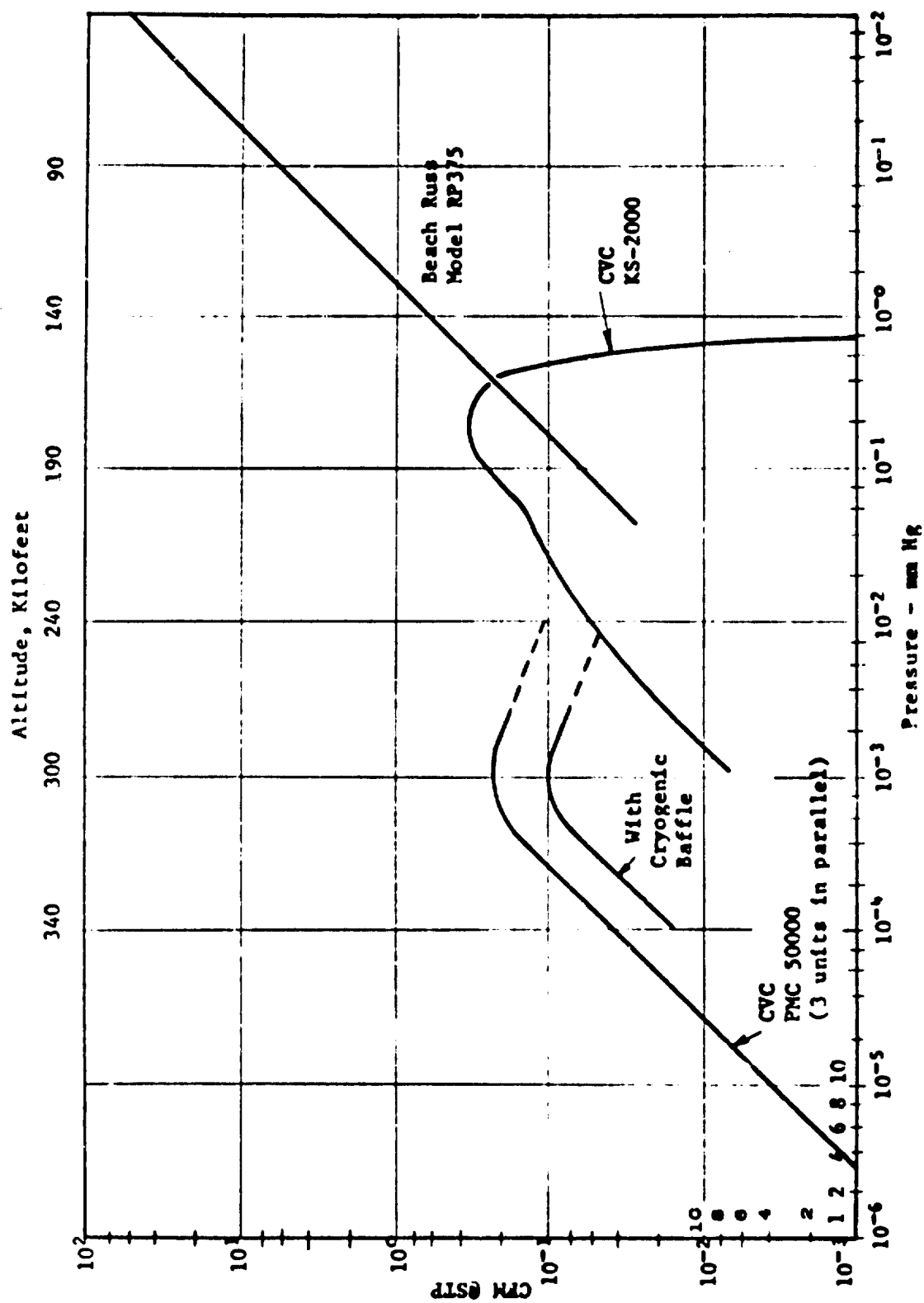


FIGURE 17. CAPACITY OF ASTROSYSTEMS LARGE DYNAMIC VACUUM FACILITY

TABLE 11

**CAPABILITY OF VACUUM SYSTEM FOR OXYGEN-HYDROGEN GAS AS A
FUNCTION OF MIXTURE RATIO AND EXPANSION RATIO**

| Case No. | Expansion Ratio | Gas Factor(f_g) | Capability Factor | Capability of Pumps | Gas Load at $\dot{w}=0.1$ g/s |
|----------|-----------------|---------------------|-------------------|---------------------|-------------------------------|
| * | ϵ | $(T/M)^{1/2}$ | f_g/f_{air} | Q_{SCFM} | Q_{SCFM} |
| A | 1.0 | 9.2 | 2.9 | 0.29 | 1.26 |
| | 2.0 | 7.4 | 2.3 | 0.23 | 0.80 |
| | 4.0 | 6.3 | 2.0 | 0.20 | 0.59 |
| | 8.0 | 5.4 | 1.7 | 0.17 | 0.44 |
| | 15.0 | 4.9 | 1.6 | 0.16 | 0.35 |
| | 40.0 | 3.7 | 1.2 | 0.12 | 0.20 |
| B | 1.0 | 10.2 | 3.2 | 0.32 | 1.18 |
| | 2.0 | 8.3 | 2.6 | 0.26 | 0.77 |
| | 4.0 | 7.4 | 2.3 | 0.23 | 0.62 |
| | 8.0 | 6.6 | 2.1 | 0.21 | 0.49 |
| | 15.0 | 6.0 | 1.9 | 0.19 | 0.40 |
| | 40.0 | 4.9 | 1.6 | 0.16 | 0.27 |
| C | 1.0 | 9.5 | 3.0 | 0.30 | 0.71 |
| | 2.0 | 8.2 | 2.6 | 0.26 | 0.53 |
| | 4.0 | 7.3 | 2.3 | 0.23 | 0.42 |
| | 8.0 | 6.6 | 2.1 | 0.21 | 0.35 |
| | 15.0 | 6.1 | 1.9 | 0.19 | 0.29 |
| | 40.0 | 5.2 | 1.6 | 0.16 | 0.21 |
| D | 1.0 | 8.4 | 2.7 | 0.27 | 0.44 |
| | 2.0 | 7.3 | 2.3 | 0.23 | 0.34 |
| | 4.0 | 6.6 | 2.1 | 0.21 | 0.28 |
| | 8.0 | 6.0 | 1.9 | 0.19 | 0.23 |
| | 15.0 | 5.5 | 1.7 | 0.17 | 0.19 |
| | 40.0 | 4.8 | 1.5 | 0.15 | 0.14 |

*Case A $O/F = 1.2$, $\bar{M} = 4.42$
 B $O/F = 2.8$, $\bar{M} = 7.60$
 C $O/F = 4.8$, $\bar{M} = 11.14$
 D $O/F = 7.9$, $\bar{M} = 15.40$

TABLE 12

**CAPABILITY OF VACUUM SYSTEM FOR OXYGEN - RP-1
GAS AS A FUNCTION OF MIXTURE RATIO AND EXPANSION RATIO**

| Case No. | Expansion Ratio | Gas Factor(f_g) | Capability Factor | Capability of Pumps | Gas Load at $\dot{w}=0.1$ g/s |
|----------|-----------------|---------------------|-------------------|---------------------|-------------------------------|
| * | ϵ | $(T/M)^{1/2}$ | f_g/f_{air} | Q_{SCFM} | Q_{SCFM} |
| A | 1.0 | 7.1 | 2.3 | .23 | 0.65 |
| | 2.0 | 5.9 | 1.9 | .19 | 0.45 |
| | 4.0 | 5.4 | 1.7 | .17 | 0.37 |
| | 8.0 | 4.9 | 1.6 | .16 | 0.32 |
| | 15.0 | 4.6 | 1.5 | .15 | 0.27 |
| | 40.0 | 4.2 | 1.3 | .13 | 0.22 |
| B | 1.0 | 6.9 | 2.2 | .22 | 0.52 |
| | 2.0 | 5.9 | 1.9 | .19 | 0.38 |
| | 4.0 | 5.5 | 1.7 | .17 | 0.32 |
| | 8.0 | 5.1 | 1.6 | .16 | 0.27 |
| | 15.0 | 4.8 | 1.5 | .15 | 0.24 |
| | 40.0 | 4.2 | 1.3 | .13 | 0.19 |
| C | 1.0 | 6.9 | 2.2 | .22 | 0.48 |
| | 2.0 | 5.9 | 1.9 | .19 | 0.35 |
| | 4.0 | 5.4 | 1.7 | .17 | 0.30 |
| | 8.0 | 5.0 | 1.6 | .16 | 0.26 |
| | 15.0 | 4.7 | 1.5 | .15 | 0.22 |
| | 40.0 | 4.2 | 1.3 | .13 | 0.18 |
| D | 1.0 | 7.2 | 2.3 | .23 | 0.51 |
| | 2.0 | 5.9 | 1.9 | .19 | 0.34 |
| | 4.0 | 5.3 | 1.7 | .17 | 0.28 |
| | 8.0 | 5.0 | 1.6 | .16 | 0.25 |
| | 15.0 | 4.6 | 1.5 | .15 | 0.22 |
| | 40.0 | 4.0 | 1.3 | .13 | 0.17 |

*Case A C/F = 1.80, \bar{M} = 19.23
 B C/F = 2.35, \bar{M} = 21.50
 C C/F = 2.65, \bar{M} = 22.45
 D C/F = 3.10, \bar{M} = 23.60

TABLE 13

**CAPABILITY OF VACUUM SYSTEM FOR N_2O_4 -UDMH GAS
AS A FUNCTION OF MIXTURE RATIO AND EXPANSION RATIO**

| Case No. | Expansion Ratio | Gas Factor (f_g) | Capability Factor | Capability of Pumps | Gas Load at $\dot{w}=0.1$ g/s |
|----------|-----------------|----------------------|-------------------|---------------------|-------------------------------|
| * | c | $(T/t)^{1/2}$ | f_g/f_{air} | Q_{SCFM} | Q_{SCFM} |
| A | 1.0 | 6.9 | 2.2 | .22 | .63 |
| | 2.0 | 5.9 | 1.9 | .19 | .46 |
| | 4.0 | 5.2 | 1.6 | .16 | .36 |
| | 8.0 | 4.6 | 1.5 | .15 | .28 |
| | 15.0 | 4.1 | 1.3 | .13 | .22 |
| | 40.0 | 3.4 | 1.1 | .11 | .16 |
| B | 1.0 | 6.8 | 2.2 | .22 | .50 |
| | 2.0 | 5.9 | 1.9 | .19 | .38 |
| | 4.0 | 5.3 | 1.7 | .17 | .30 |
| | 8.0 | 4.8 | 1.5 | .15 | .25 |
| | 15.0 | 4.3 | 1.4 | .14 | .20 |
| | 40.0 | 3.7 | 1.2 | .12 | .15 |
| C | 1.0 | 6.6 | 2.1 | .21 | .47 |
| | 2.0 | 5.9 | 1.9 | .19 | .35 |
| | 4.0 | 5.2 | 1.6 | .16 | .28 |
| | 8.0 | 4.7 | 1.5 | .15 | .22 |
| | 15.0 | 4.3 | 1.4 | .14 | .19 |
| | 40.0 | 3.7 | 1.2 | .12 | .14 |
| D | 1.0 | 6.4 | 2.0 | .20 | .43 |
| | 2.0 | 5.7 | 1.8 | .18 | .33 |
| | 4.0 | 5.1 | 1.6 | .16 | .27 |
| | 8.0 | 4.5 | 1.4 | .14 | .21 |
| | 15.0 | 4.1 | 1.3 | .13 | .18 |
| | 40.0 | 3.6 | 1.1 | .11 | .13 |
| E | 1.0 | 6.1 | 1.9 | .19 | .40 |
| | 2.0 | 5.3 | 1.7 | .17 | .29 |
| | 4.0 | 4.8 | 1.5 | .15 | .24 |
| | 8.0 | 4.3 | 1.4 | .14 | .19 |
| | 15.0 | 3.9 | 1.2 | .12 | .16 |
| | 40.0 | 3.3 | 1.0 | .10 | .11 |

*Case A O/F = 1.5, \bar{M} = 18.68
 B O/F = 2.3, \bar{M} = 22.08
 C O/F = 2.75, \bar{M} = 23.38

Case D O/F = 3.5, \bar{M} = 24.98
 E O/F = 4.5, \bar{M} = 26.46

and decrease flow rate as required to study the regions of less interest.

It should also be noted that the molecular weight of the exhaust gases entering the diffusion pumps will not be the same as that leaving the rocket engine. This effect adds to the capability of the pumping system for all cases of oxygen-hydrogen testing and aids the higher mixture ratio cases for the other two propellants. It will cause a slight decrease in capability for the carbonaceous propellants when the relative percentage of H_2O to CO_2 exceeds 2.5:1. Hence, the overall effect supports the general plan of designing the experimental engine for a flow rate of 0.1 gm/sec at optimum conditions and reducing flow at points well off optimum.

B. SIGNAL-TO-NOISE RATIO

The radiant intensities detailed in Section 3, Tables 6, 7 and 8 were based on a flow rate of 0.1 gm/sec. The foregoing rocket engine analysis versus vacuum test capability was based on the same flow rate. Therefore, a signal-to-noise ratio can now be specified by employing the detector capabilities detailed in Section 3, Part B.

Table 14 summarizes the radiant intensities at the primary transitions of the major radiating species in the ultraviolet-visible region of the spectrum and the dark current of the phototubes which we plan to use in these regions. The phototubes selected were among those described in Section 3, and were chosen from those currently available at this corporation based on their applicability to the detection of the wavelengths discussed previously. Because of the apparently good margin of detectability (at least four orders of magnitude), it does not appear to be necessary to select more specialized instrumentation than the two phototubes noted in Table 14. The EMI tube appears to be more than adequate from 2800 to 5500 Å and the EMR appears to be adequate at the shorter wavelengths down to 1450 Å. The sensitivity values noted for these phototubes in Table 14 were taken from calibration curves previously conducted at this corporation, and the dark current specified is an actual measured value.

In the infrared the noise-equivalent power ratio (NEP) of noise-to-signal ratio, for the common lead sulphide cell is 1.6×10^{-11} at 2.7 μ and 70°F and 1×10^{-8} at 4.3 microns and 70°F. This sensitivity will suffice for the detection of H_2O up to 3.0 μ where intensity is at least five orders of magnitude greater than the noise (see Table 8). However, for the detection of CO_2 up to about 6.0 μ an uncooled lead selenide detector is preferred. This will provide a signal-to-noise ratio of at least two orders of magnitude. Infrared detectors are available at this corporation.

C. SPECIFICATION OF DESIGN CRITERIA

The performance characteristics of small operational rocket engines functioning in a true space environment cannot be duplicated even in very large and costly space simulation chambers. Practical considerations,

TABLE 14
SIGNAL-TO-NOISE RATIO, UV-VISIBLE REGION

| Propellant Combination | Exhaust Product | Wave- Length, Å | Intensity (Watts/cm ² /ster) | Photo- multiplier Type | P.A Sens. @λ (Amps/watt) | PM Curr. (Amps) | PM Dark Current (Amps) | Signal-to- Noise Ratio |
|-------------------------------------|--------------------|-----------------------|--|------------------------------|--------------------------------|------------------------|------------------------------|---------------------------|
| LO ₂ /RP-1 | C ₂ | 5165.2 | 1.17 x 10 ⁻¹⁰ | EMI | 8.0 x 10 ³ | 9.4 x 10 ⁻⁷ | 1 x 10 ⁻¹¹ | 9.4 x 10 ⁴ |
| | CH | 4315.3 | 1.80 x 10 ⁻¹⁰ | EMI | 1.0 x 10 ⁴ | 1.8 x 10 ⁻⁶ | 1 x 10 ⁻¹¹ | 1.8 x 10 ⁵ |
| | CO | 2455.4 | 3.38 x 10 ⁻⁶ | EMR | 9.0 x 10 ³ | 3.0 x 10 ⁻² | 3 x 10 ⁻¹¹ | 3.0 x 10 ⁹ |
| | OH | 2806.8 | 1.43 x 10 ⁻² | EMR | 5.0 x 10 ³ | 7.1 x 10 ⁻¹ | 3 x 10 ⁻¹¹ | 2.4 x 10 ¹² |
| N ₂ O ₄ /UDMH | CN | 3883.4 | 3.98 x 10 ⁻⁷ | EMI | 1.3 x 10 ⁴ | 5.2 x 10 ⁻³ | 1 x 10 ⁻¹¹ | 5.2 x 10 ⁸ |
| | NH | 3360 | 8.4 x 10 ⁻⁶ | EMI | 1.0 x 10 ⁴ | 8.4 x 10 ⁻² | 1 x 10 ⁻¹¹ | 8.4 x 10 ⁹ |
| | NO | 2262.8 | 2.91 x 10 ⁻⁵ | EMR | 5.0 x 10 ³ | 1.5 x 10 ⁻¹ | 3 x 10 ⁻¹¹ | 5.0 x 10 ⁹ |

therefore dictate that compromises be made in order to obtain preliminary information on space phenomena for the purpose of establishing the feasibility of concepts.

1. Engine Description - Over a period of several years Astrosystems has developed and refined a technique for the production of rocket exhaust plumes at altitudes up to 350,000 ft. This technique utilizes the vacuum system described in Part A of this section together with miniature rocket motors operating efficiently with exhaust gas flows into the vacuum systems of approximately 1.5 gms/sec to under 0.1 gms/sec.

In order to achieve a high combustion efficiency (approximately 90% of theoretical C^*) and a low level of heat loss from the combustion products to the chamber wall, the rocket motor is operated at relatively high propellant flows and the excess combustion gases, exceeding that of the vacuum system pumping capability, are dumped overboard outside the vacuum tank. Hence, the combustion gases vented into the vacuum tank are representative of the center core combustion region and are relatively unaffected by the flow and thermodynamic conditions at the combustion chamber walls.

Schematically the experimental system may be represented as shown in Figure 18. From this figure it can be seen that various parameters can be controlled. The propellant pressurization and flow controls together with the injector pressure drop determine the total propellant mass flow and mixture ratio. The plume nozzle throat size and overboard bleed orifice size determine the combustion chamber pressure and relative fraction of combustion products that exhaust to the vacuum tank. The pump controls, nitrogen control and plume exhaust characteristics determine the pressure (altitude) in the vacuum tank. There are interrelations among the various available controls, and not all of them are necessarily used in any given experiment.

Figure 19 shows a typical micro-rocket with overboard bleed. This motor was designed for premix injection of gaseous oxygen/RP-1 liquid hydrocarbon fuel. For various propellant combinations the aft injector section of the motor is changed using the same bypass and nozzle section. The nozzles are removable so that various sizes, shapes and materials may be used.

2. Exhaust Nozzle Design - In designing the model rocket nozzle, consideration was given to simulation of full scale rocket engine nozzle exit conditions since they affect measurements made by the subject technique. Since the spectroscopic technique for monitoring mixture ratio is dependent upon the radiation from the nozzle exit station, both the temperature and density at the nozzle exit station must be simulated as close as possible. The exhaust temperature in microrocket engines is somewhat lower than the corresponding nozzle exit temperatures of full scale rockets. Thus to increase the exhaust temperatures in the model rocket, small area ratio ($c+1$) nozzles have been considered for this program. These sonic nozzles will maximize the radiation intensity emitted from the rocket exhaust.

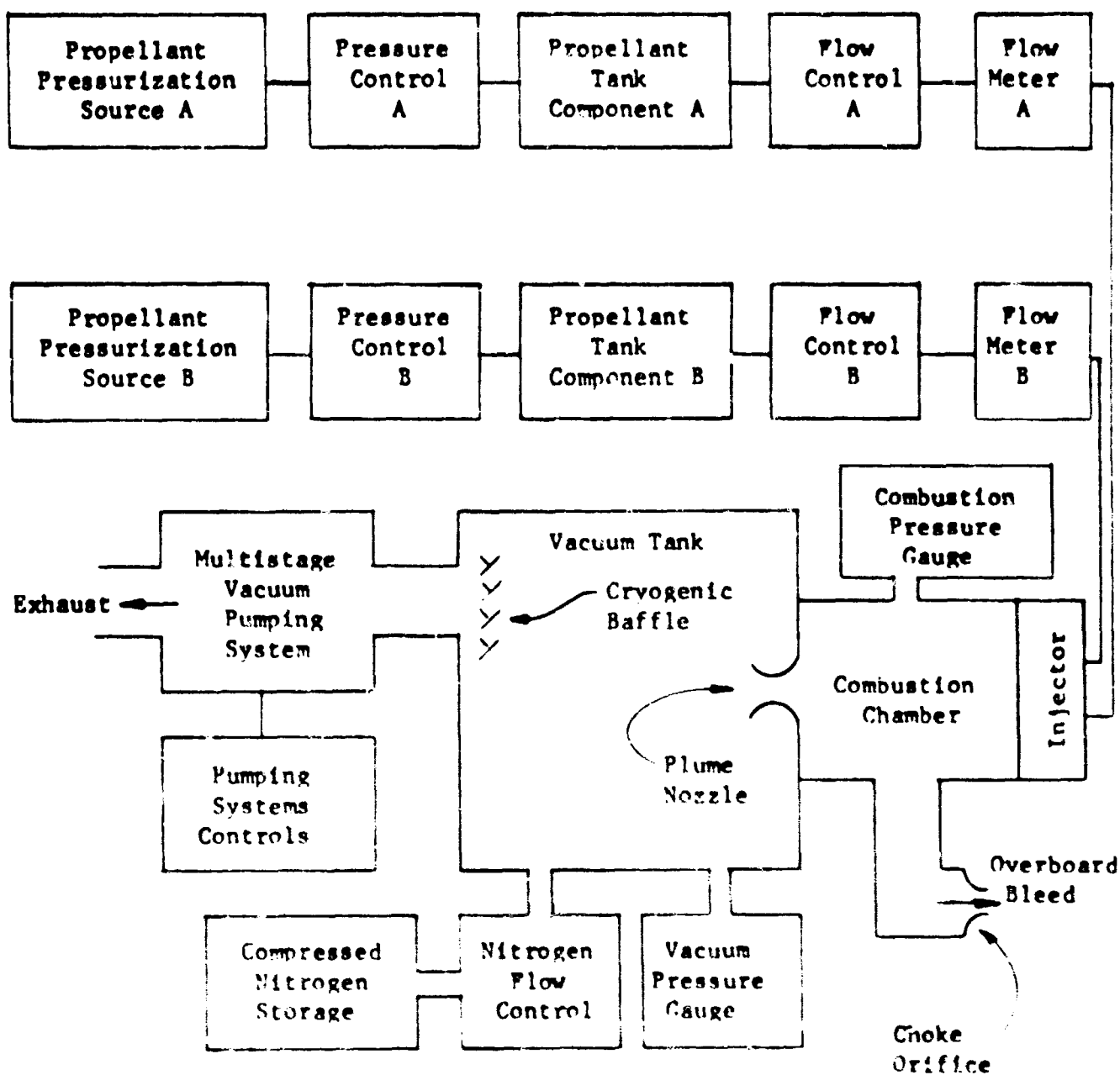


Figure 18. Schematic Rocket Engine - Vacuum System

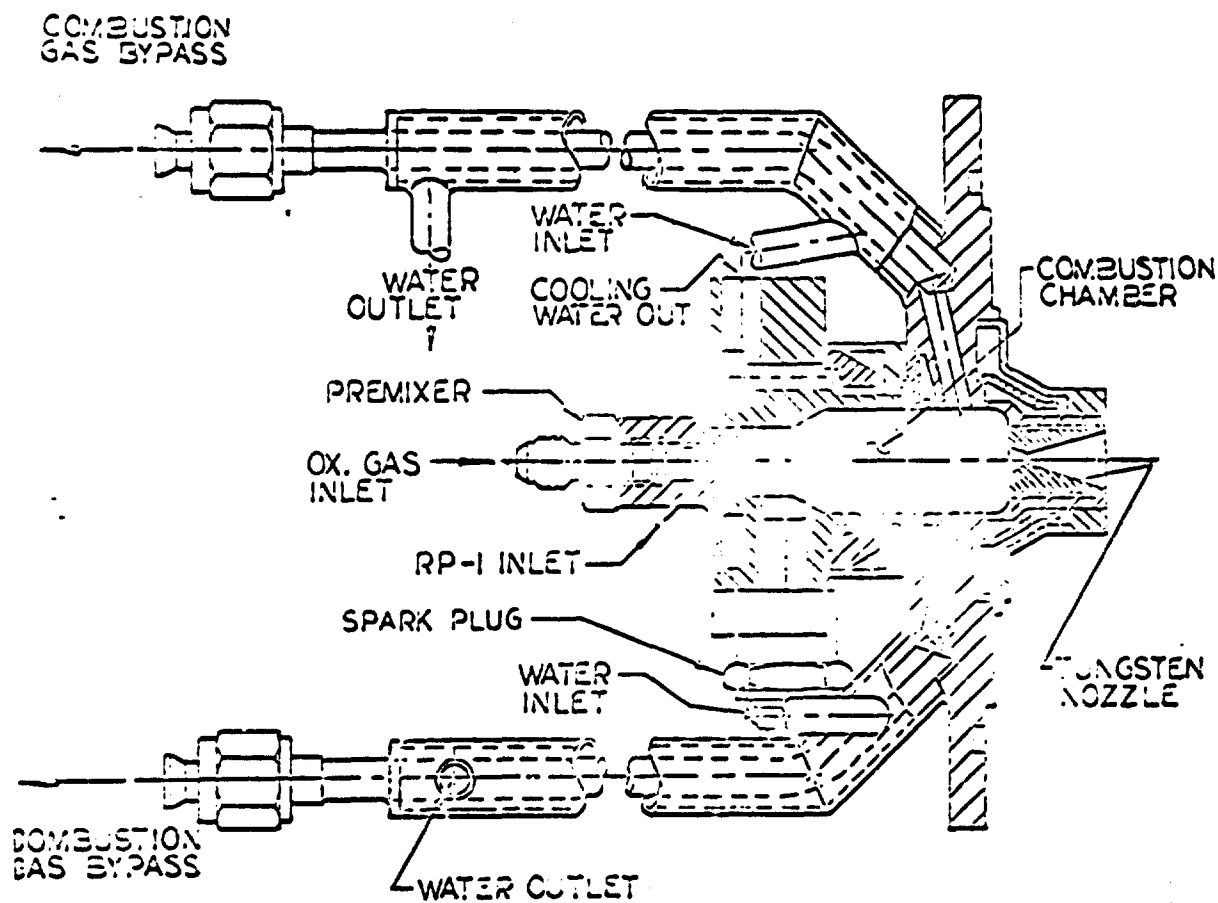


FIGURE 19 Research Rocket Engine (Premixer)

To demonstrate the simulation of the other important thermodynamic variable in the model rocket exhaust namely: density, a calculation was made comparing the sonic nozzle exit density with that of the Titan II second stage ($\epsilon=49.2$) which is comparable to the space rocket engines ($\epsilon=40$) being considered for spectroscopic monitoring.

The continuity equation for the conservation of mass can be written:

$$\rho = \dot{w}/(Au) \quad (4.9)$$

Using the subscript M for the model rocket engine and the subscript H for the full scale engine:

$$\rho_H = \dot{w}_H/(Au)_H \quad (4.10)$$

and

$$\rho_M = \dot{w}_M/(Au)_M$$

Defining the ratio ρ_r as the relative density between the model and full scale engines:

$$\rho_r = \rho_H/\rho_M = \frac{\dot{w}_H/\dot{w}_M}{(A_H/A_M)(u_H/u_M)} = \dot{w}_r/A_r u_r \quad (4.11)$$

where \dot{w}_r , A_r and u_r are the corresponding relative flow rates, exit areas and exit velocities.

The flow rate \dot{w}_m through the model rocket engine at the simulated altitude is dictated by the vacuum tank pumping capability. Using the appropriate values for the Titan II second stage engine (classified) and the model rocket sonic nozzle engine, it was found that one obtains equivalent exit densities ($\rho_r=1$) for a sonic nozzle design throat (or exit) diameter of .066 inches with a flow rate of .11 gm/sec. The resulting mass density at the nozzle exit in both the full scale and model rockets is then 1.5×10^{-3} lbs/ft³. One should note that for different model rocket nozzle throat diameters, ρ_r is directly proportional to the throat diameter squared, i.e., ρ_r is proportional to the sonic nozzle throat or exit area.

The radiation from the rocket exhaust however, is actually dependent upon the number density N and not the mass density ρ . Thus the factor N_A/\bar{M} has to be applied to ρ to obtain N . Since Avogadro's number is a constant and \bar{M} is approximately the same for both the full scale and model rocket engines, the total number density N will be equal for both engines ($N_r=1$). The value for the total number density is 1.85×10^{22} particles/ft³.

Thus, in conclusion, the number density at the nozzle exhaust which is an important parameter in the calculation of radiation intensities (for the case of optically thin and optically thick radiation sources) can be simulated by the use of the converging sonic nozzle for which these calculations were made. Based upon this factor, and the fact that

the sonic nozzle will maximize radiation intensity, it was decided to use this type of nozzle for the experimental program. Typical characteristics of a sonic nozzle which have already been run at Astrosystems are given in Table 15.

It should also be pointed out that large boundary layers exist near the exit station of a conventional converging-diverging microrocket engine nozzle. This boundary layer buildup causes non-uniform (parabolic) velocity and temperature distributions at the exit plane. These viscous effects also effect the rocket plume structure. Thus, to eliminate the boundary layer buildup on the diverging section of the nozzle, it is of further advantage to utilize converging sonic nozzles in carrying out an experimental program.

3. Convergent Nozzle Design - The previous analysis was conducted to demonstrate the correspondence between the macroscopic distribution of energies in the full scale and model rocket engines, and the geometrical similarity of the exhaust gas plume in the region of spectroscopic observation. Since the thermodynamic variables affecting the radiation emitted from the plume are coupled with the dynamics of the flow field, one would like to ensure that the distribution between the internal energy and the kinetic energy of the plumes are similar.

The initial inclination angle (C_b) of the jet boundary of the plume is a measure of the ratio between these two energy modes. Thus the following analysis was conducted to determine: (1) if the sonic nozzle presently being considered for the program actually simulates the plume energy distribution and geometry of space engines ($\epsilon=40/1$) in the immediate area of the nozzle exit station where radiation will be spectroscopically monitored, and to determine: (2) the optimum sonic nozzle convergence half angle for this purpose.

The method of analysis employed is the method of characteristics for non-reacting gases. The assumption of non-reacting gases is valid for both the microrocket plume and the full scale plume in the immediate neighborhood of the nozzle exit station where the plumes initial inclination (spreading) occurs, since the fluid dynamic flow time from the nozzle exit station to the point at which the initial spreading takes place is small.

The equation used here to demonstrate simulation of initial jet boundary inclination angle is basic to the method of characteristics and in particular to the Prandtl-Meyer type flow considered. For this flow, it is required that from one point to another in the flow field, the change in flow deflection angle (θ) must be equal to the change in the Prandtl-Meyer function (v); thus:

$$d\theta = dv, \text{ or} \quad (4.12)$$

$$\theta_2 - \theta_1 = v_2 - v_1$$

where in general:

TABLE 15
SUMMARY OF NOZZLE AND PLUME PARAMETERS
FOR THE SONIC NOZZLE

| | |
|---|-------------------------------------|
| Nozzle Exhaust Area Ratio ϵ | 1 |
| Nozzle Type | Converging Sonic |
| Exit Diameter | 0.063/0.067 |
| Exit Angle (Degrees) | -70 |
| Throat Diameter (in) | .063/.067 |
| Chamber Pressure (psia) | 42 |
| Characteristic Velocity (ft/sec) | 4920 |
| Flow Rate \dot{W}_m (gm/sec) | .110 |
| Vacuum Tank Pressure (microns) | .5/.7 |
| Overall Pressure Ratio (Chamber Pressure/Vacuum Tank Pressure) | $5.8 \times 10^6 / 3.7 \times 10^6$ |
| Overall Turning Angle (degrees) | 145 |
| Exit Mach Number | 1 |
| Internal Turning Angle (degrees) | 0 |
| External Turning Angle (degrees) | 145 |
| Initial Inclination of Jet Boundary (degrees) | 75 |
| Radius of Initial Portion of Jet Boundary (in) | 1.48 |
| Burning Time (Duration-sec.) | 930/975 |
| C^*/C^*_{theor} (%) | 90.3/92.6 |
| O/F (N_2O_4 -Aerozine) | 2.25/2.24 |

$$v = \left(\frac{\gamma+1}{\gamma-1}\right)^{1/2} \tan^{-1} \left[\left(\frac{\gamma-1}{\gamma+1}\right) (M^2-1) \right]^{1/2} - \tan^{-1} (M^2-1)^{1/2} \quad (4.13)$$

This equation can be derived from the equation for the change of speed across a weak oblique shock (which in the limit is a Mach line):

$$\frac{du}{u} (M^2-1)^{1/2} = d\theta \quad (4.14)$$

by definition:

$$u = aM \quad (4.15)$$

(u is the local velocity and a is the local sound speed), where M is given by the isentropic relationship:

$$\frac{T_t}{T} = \frac{a_t^2}{a^2} = 1 + \frac{\gamma-1}{2} M^2 \quad (4.16)$$

Differentiating, one finds that:

$$\frac{du}{u} = \frac{dM}{M} + \frac{da}{a} = \frac{dM}{M} \left(1 + \frac{\gamma-1}{2} M^2\right)^{-1} \quad (4.17)$$

and therefore,

$$d\theta = \left(1 + \frac{\gamma-1}{2} M^2\right) \frac{dM}{M} \quad (4.18)$$

Integrating this expression gives:

$$\theta_2 - \theta_1 = \left(\frac{\gamma+1}{\gamma-1}\right)^{1/2} \left(\tan^{-1} \sqrt{\left(\frac{\gamma-1}{\gamma+1}\right) (M^2-1)} \right) \bigg|_{M_1}^{M_2} - \tan^{-1} \sqrt{M^2-1} \bigg|_{M_1}^{M_2} \quad (4.19)$$

The right-hand side of the above equation is defined as the Prandtl-Meyer function v.

Thus,

$$\theta_2 - \theta_1 = v_2 - v_1 \quad (4.20)$$

where

$$v = \left(\frac{\gamma+1}{\gamma-1}\right)^{1/2} \tan^{-1} \left[\left(\frac{\gamma-1}{\gamma+1}\right) (M^2-1) \right]^{1/2} - \tan^{-1} (M^2-1)^{1/2} \quad (4.21)$$

as given previously.

For the problem considered here, the points of interest in the flow field are the nozzle exit station (e) across which the flow properties are assumed to be uniform, and the jet boundary (b) of the rocket ex-

haust plume where it is justifiably assumed that the plume static pressure is equal to the local ambient atmospheric pressure. For points between the exit station and the jet boundary, the above procedure is not applicable since this included flow field is not a simple wave flow field but is instead a region of wave interaction (non-simple wave flow). Unfortunately, therefore, the above procedure cannot be applied to calculate the entire plume flow field. To accomplish this, a digital computer program is required which can calculate the plume aerothermodynamics from the input conditions at the nozzle exit station.

In applying equation (4.20) to the problem at hand, namely determining the sonic nozzle convergence half angle θ_e required for simulation of the initial plume inclination angle θ_b of a full scale rocket engine, the following equation can be written for the full scale rocket engine:

$$\theta_e - \theta_b = v_e - v_b \quad (4.22)$$

$$\text{or } \theta_e = \theta_b + v_e - v_b$$

(For a bell shaped nozzle $\theta_e = 0$).

For sonic nozzle model rocket engine case, v_e is zero since $M_e = 1$, and hence:

$$\theta_e = \theta_b - v_b \quad (4.23)$$

The following considerations have to be made in determining the initial plume inclination angle θ_e from the values of v_e , v_b and θ_b . Since θ_e is known for a given full scale rocket nozzle geometry it is only necessary to determine v_e and v_b for the full scale rocket plume. Since $v = f(M, \gamma)$ it is only necessary to know the nozzle exit Mach number M_e , the ratio of specific heats γ_e , and the plume boundary Mach number M_b . The quantities M_e and γ_e are usually known for a given full scale rocket nozzle and the plume boundary Mach number can be determined from the isentropic flow relationship:

$$M_b = \left(\frac{2}{\gamma-1} \right)^{1/2} \left[\left(\frac{P_T}{P} \right)^{\gamma-1/\gamma} - 1 \right]^{1/2}, \quad (4.24)$$

where P_T is the total pressure in the isentropic flow field and is thus constant throughout the plume flow field, and P is the static pressure at the plume boundary.

Assuming an isentropic nozzle flow, the total pressure in the flow field is the combustion chamber pressure P_c (i.e., $P_T = P_c$). The static pressure at the jet boundary is simply the local ambient atmospheric pressure (P_∞) by virtue of the matching of the boundary condition that must be imposed at the plume boundary. This is necessarily true when a supersonic (or sonic) nozzle exhausts into a low pressure region as the exhaust jet expands until the pressure along the jet boundary adjusts to the ambient pressure. With these equations and the corresponding assumptions indicated, the following calculations were carried

out, using the procedure indicated.

Comparisons of plume initial inclination angle were made between a high area ratio nozzle such as that employed on the second stage of the Titan II missile and the sonic nozzle model rocket engines run at Astro-systems. Using the equations given previously the initial plume inclination angle for the full scale rocket θ_{bH} can be calculated using equation (4.20). Since the Titan II second stage employs a bell nozzle, the exit angle $\theta_{eH} = 0$. Thus for the full scale rocket (H)

$$\theta_{bH} = (v_b - v_e)H \quad (4.25)$$

where v_{bH} is calculated from the value of the pressure ratio parameter P_w/P_c and γ , and v_{eH} is calculated from the value of c_H and γ .

The results are plotted in Figure 20 from which it can be seen that the relationship between θ_{bH} and altitude is an approximately linear one over the range of the plot.

The sonic convergence half angle θ_{eM} required to simulate or produce this plume inclination angle θ_{bH} at the nozzle exit station is calculated using equation (4.23) as follows. Since $M_{eM} \approx 1$, $v_{eM} = 0$, and thus:

$$\theta_{eM} = \theta_{bM} - v_{bM} \quad (4.26)$$

where $\theta_{bM} = \theta_{bH}$ is the initial plume inclination angle to be reproduced as shown in Figure 20. The value of v_{bM} is calculated in the same way as v_{bH} ; namely, from the value of the pressure ratio parameter P_w/P_c and γ . It should be noted that the rocket chamber pressure of the full scale engine ($\epsilon = 49.2$) is approximately twenty times larger than the chamber pressure in the model rocket engine.

The results of the calculation for the variation of sonic nozzle convergence half angle with altitude are shown in Figure 21. From this figure it can be seen that the sonic nozzle convergence half angle must be approximately -75° to simulate the initial plume inclination angle over the range of altitude between 150,000 and 350,000 feet (and probably higher). Thus one nozzle can be used to simulate the plume jet boundary in the vicinity of the nozzle exit station where spectroscopic measurements are observed. This simulation implies that the distribution of thermal and kinetic energy at the rocket exhaust, which effects the radiation characteristics, will be duplicated. The manner in which the energy distribution is accounted for in the equation used here ($\Delta O = \Delta v$) can be seen from the derivation of this equation which was presented previously.

Comparative calculations were also carried out for "small" area ratio nozzles ($\epsilon \approx 8$) such as the Titan II first stage, to determine what the plume initial inclination angle and the necessary corresponding nozzle convergence half angle required are as a function of altitude. The calculations were carried out in the same manner as the previous calculations for the Titan II second stage. The results for θ_b and θ_e

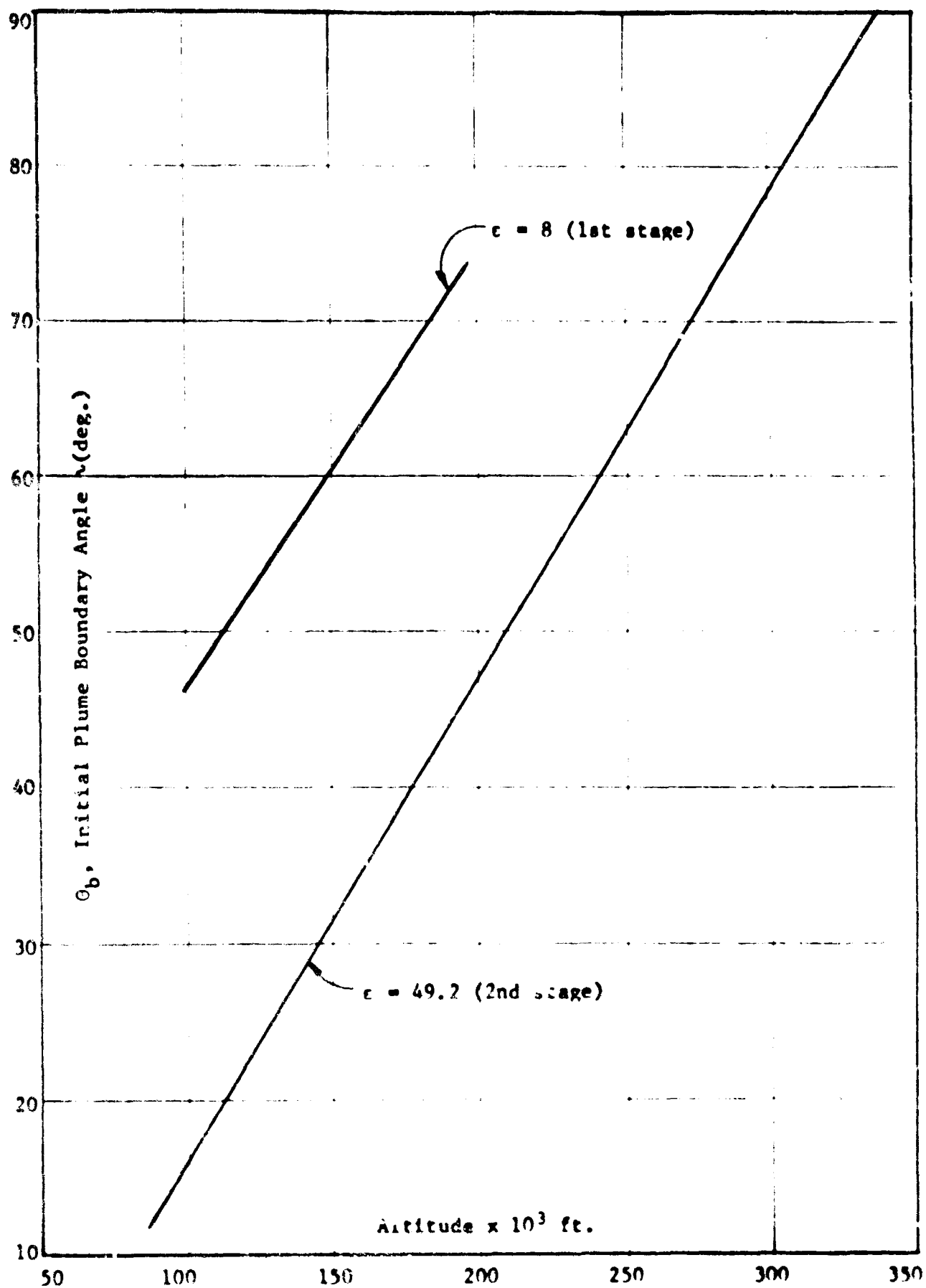


Figure 20. Initial Plume Boundary Angle
for Titan II Missile vs Altitude

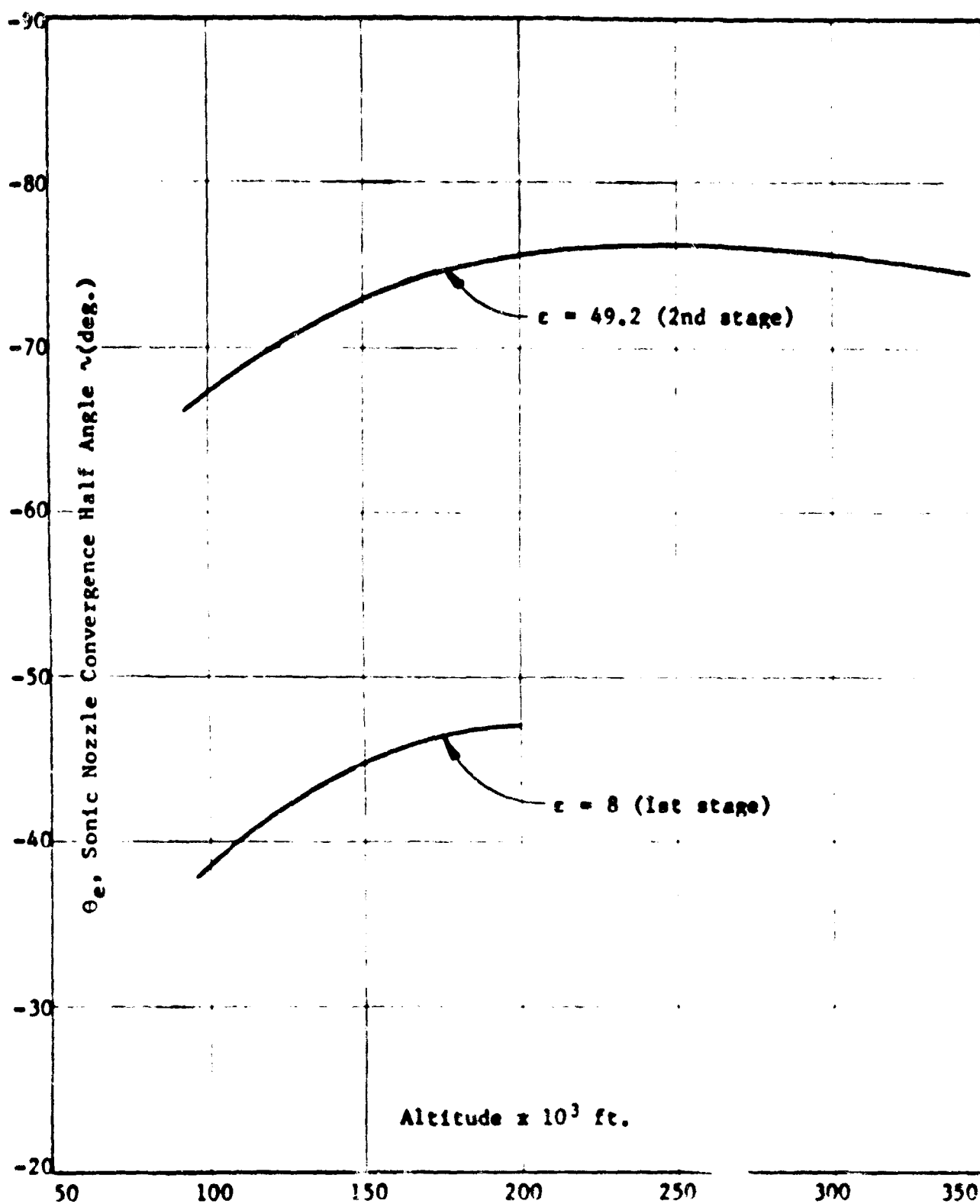


Figure 21. Sonic Nozzle Convergence Half Angle Required to Simulate Initial Plume Boundary Angle vs Altitude

are shown in Figures 20 and 21 respectively.

From Figure 20 it can be seen that the lower expansion ratio has a much larger θ_b (on the order of 30°) as would be expected, since the gases have not been accelerated to as high a velocity or expanded to as low a temperature as is the case with the higher area ratio nozzle. The relationship between θ_b and altitude for $\epsilon = 8$ is again linear as was the relationship between θ_b and altitude for $\epsilon = 49.2$. The corresponding sonic nozzle convergence half angle required to produce the values of θ_b shown in Figure 20, for $\epsilon = 8$, are shown in Figure 21, from which it can be seen that a sonic nozzle with $\theta_e = -45^\circ$ is required.

In order to determine if simulation of the jet boundary is obtained, one can use Latvala's circular arc approximation to calculate the jet boundary for the sonic nozzle from the following equation:

$$R/r_e = (R/r_e)_{\gamma=1.4} \left[\frac{(\gamma+1)(5+M_e^2)}{12(1+\frac{\gamma-1}{2}M_e^2)} \right]^{1/2} \quad (4.27)$$

where r_e = nozzle exit radius.

$(R/r_e)_{\gamma=1.4}$ can be determined from Figure 22 as a function of M_e . For the sonic nozzle where $\gamma_e = 1.4$ the value of (R/r_e) is 38.4. For other values of γ the value of 38.4 is still valid since setting $M_e = 1$ in equation (4.27) reduces the equation to $(R/r_e) = (R/r_e)_{\gamma=1.4}$.

Therefore, the circular arc plume boundary can be geometrically drawn using the sketch shown in the upper right corner of Figure 22, using the value of R given above and the value of θ_b calculated given previously in Figure 20.

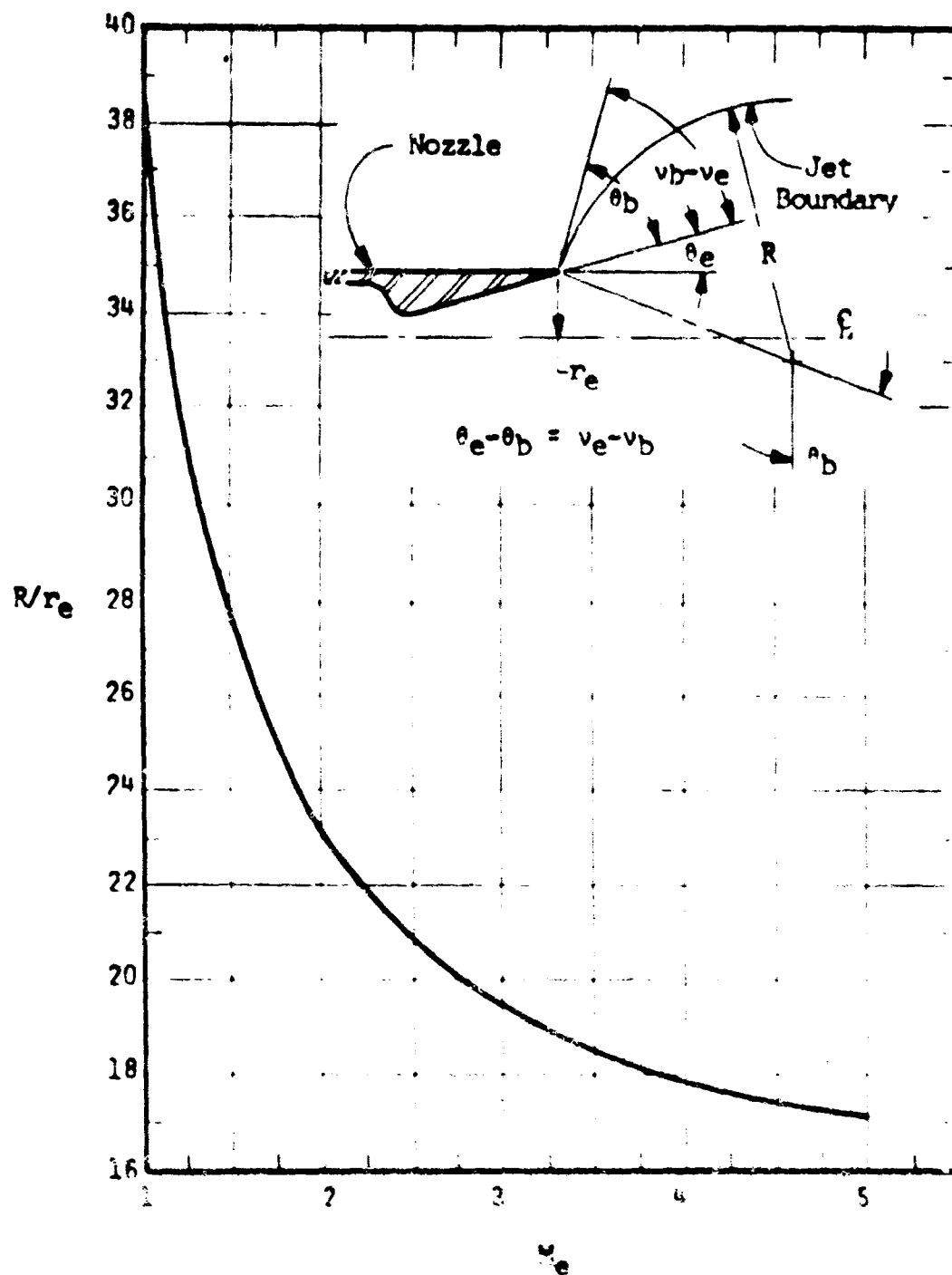


Figure 22. Radius of Jet Boundary for $\gamma=1.4$

SECTION 5

MIXTURE RATIO ANALYSIS

The objective of this section is the determination of plume radiant intensity as a function of mixture ratio and the applicability of seeding to the determination of mixture ratio by spectroscopic techniques. Plume radiant intensity as a function of mixture ratio was determined by programming the pertinent equations previously described for electronic transition, molecular vibration and blackbody induced radiation; examples of experimentally determined variations are also presented.

A. THEORETICAL INTENSITY VS MIXTURE RATIO

The calculations of the rocket exhaust radiant intensities for the constituents in the microrocket plumes radiating in the ultraviolet region of the optical spectrum have been completed for N_2O_4 /UDMH propellant. The data was obtained as a function of O/F ratio for constant chamber ($P_c = 100$ psia) and exhaust ($P_e = 50$ psia) pressures, for a sonic nozzle, assuming frozen flow.

The nozzle exhaust species considered were as follows: C_2 , CH, OH, CO, NO, NH, CN and CHO. The f values, or oscillator strengths, for several of the species (NO, CO, NH and CHO) were not available and therefore assumed. Many bands were considered for each specie so as to determine the most intense band system for the species. In some cases many such bands were considered, as in the case of NO (34 bands); in such cases the data for the more intense bands are presented. All of the intensities presented are given per unit path length (in cm) in watts/cm²-ster. To convert the values given to the intensities emitted by microrocket exhaust, one must multiply this value by the plume thickness (~ 2 cm).

The results obtained for C_2 indicated a null intensity for all bands in all cases run. This was found to be due to the limitations of the digital computer in handling the value e^{-x} as x becomes large. This is presently being corrected by breaking the exponential up into two parts namely; $e^{-a} \cdot e^{-b}$, where $a + b = x$.

The data obtained for the CH molecule at 4315.3Å (shown in Figure 23) indicated almost a linear relationship between the intensity (I) and the mixture ratio (O/F). The value of the slope of the line, i.e., $S = dI/d(O/F)$, which gives an indication of the sensitivity of the radiant intensity I to the O/F ratio, was 4×10^{-10} . Two other CH bands were calculated and showed the same linear relationship (Figures 24 and 25). The corresponding S values for these band wavelengths (3889.2Å and 3145.4Å) are 1×10^{-10} and 1.67×10^{-11} respectively. The percent change (decrease) in intensity from the peak intensity value over the range of mixture ratios considered are: 70% for the 4315.3Å band (peak intensity of 2.32×10^{-10}), 70% for the 3889.2Å band (peak intensity of 5.9×10^{-11}) and 77% for the 3145.4Å band (peak intensity 8.7×10^{-12}).

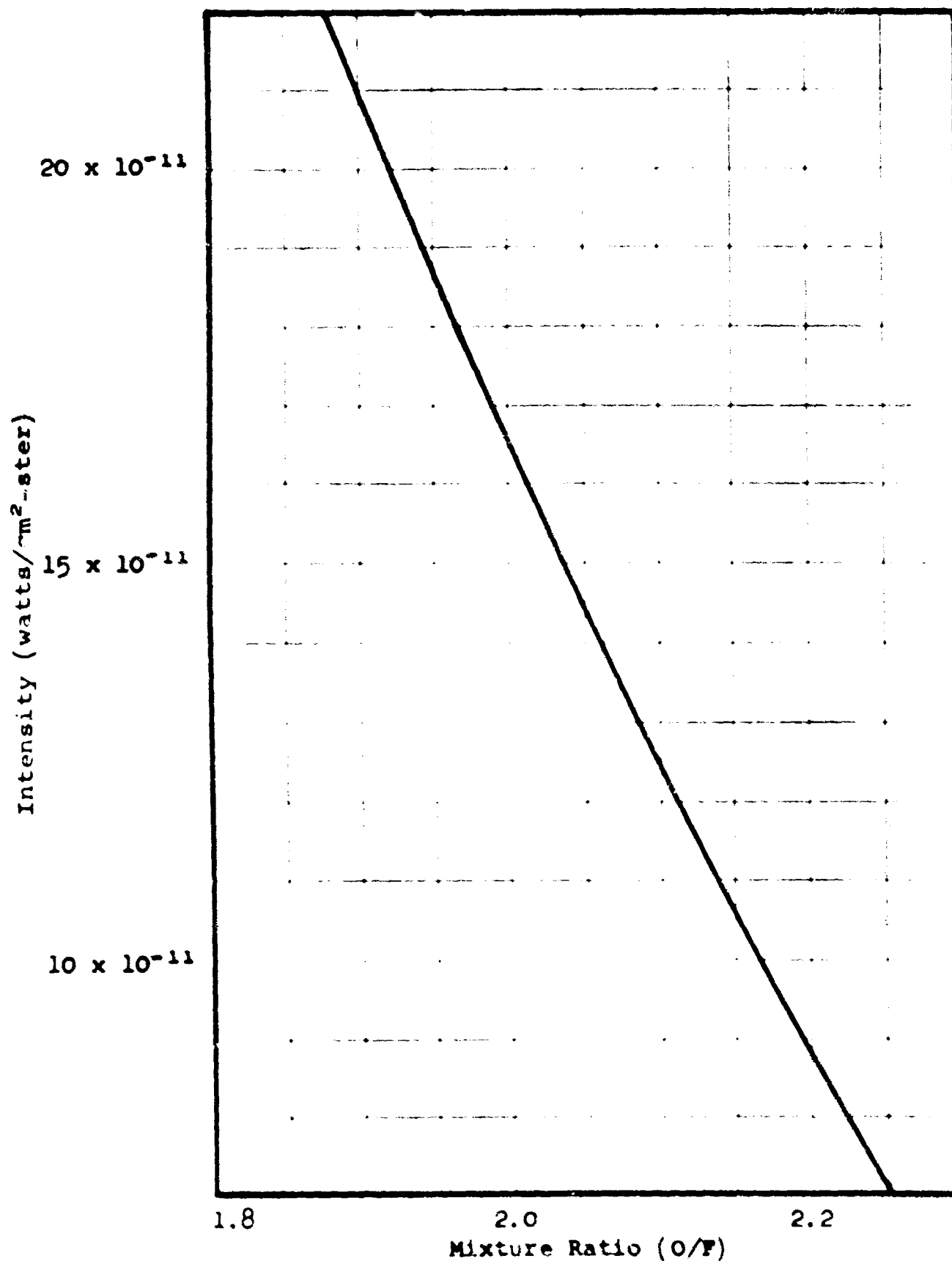


Figure 23. Theoretical Intensity of CH 4315.3A⁰ vs Mixture Ratio for N₂O₄/UDMH

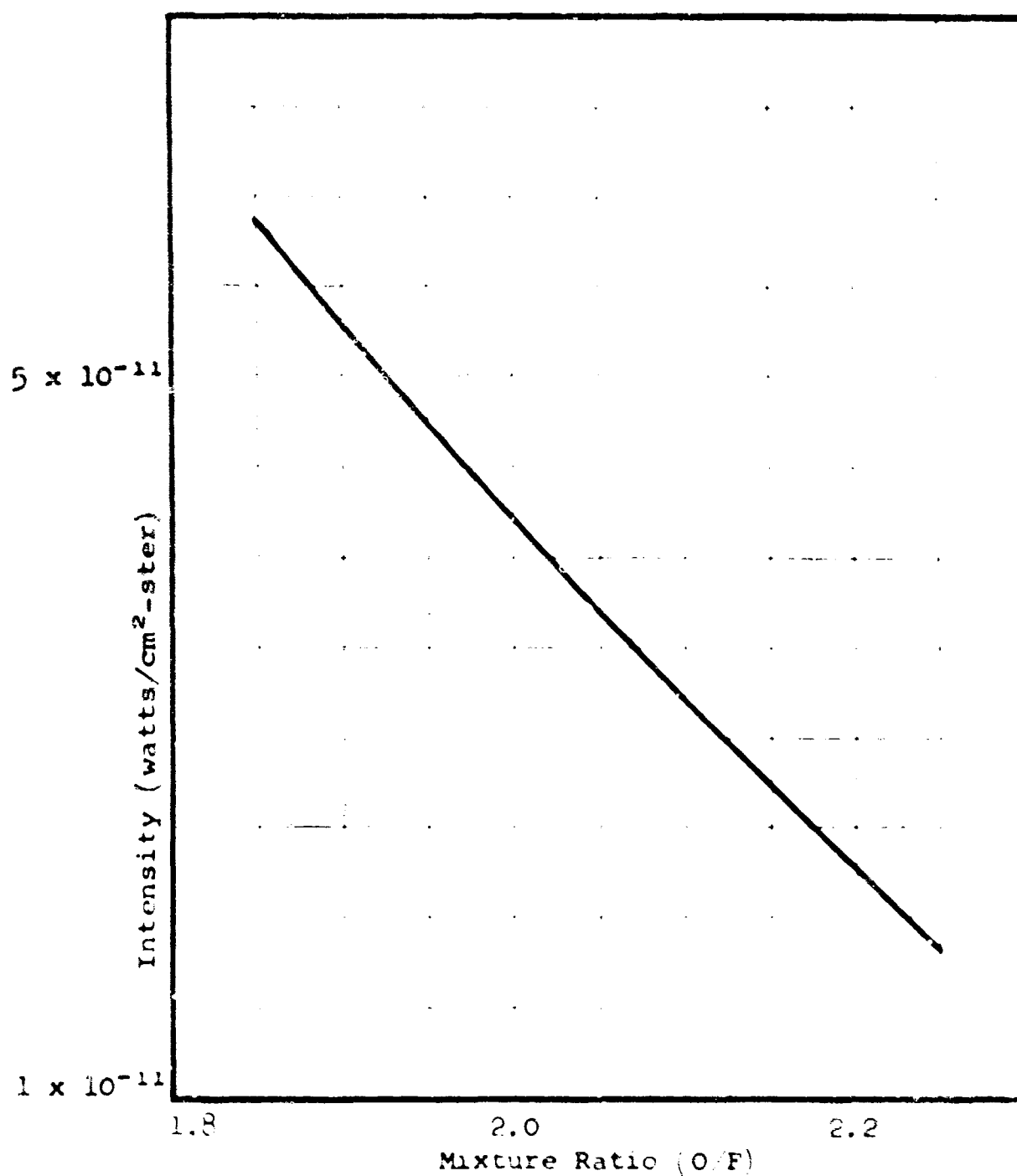


Figure 24. Theoretical Intensity of CH 3889.2A⁰ vs Mixture Ratio for N₂O₄/UDMH

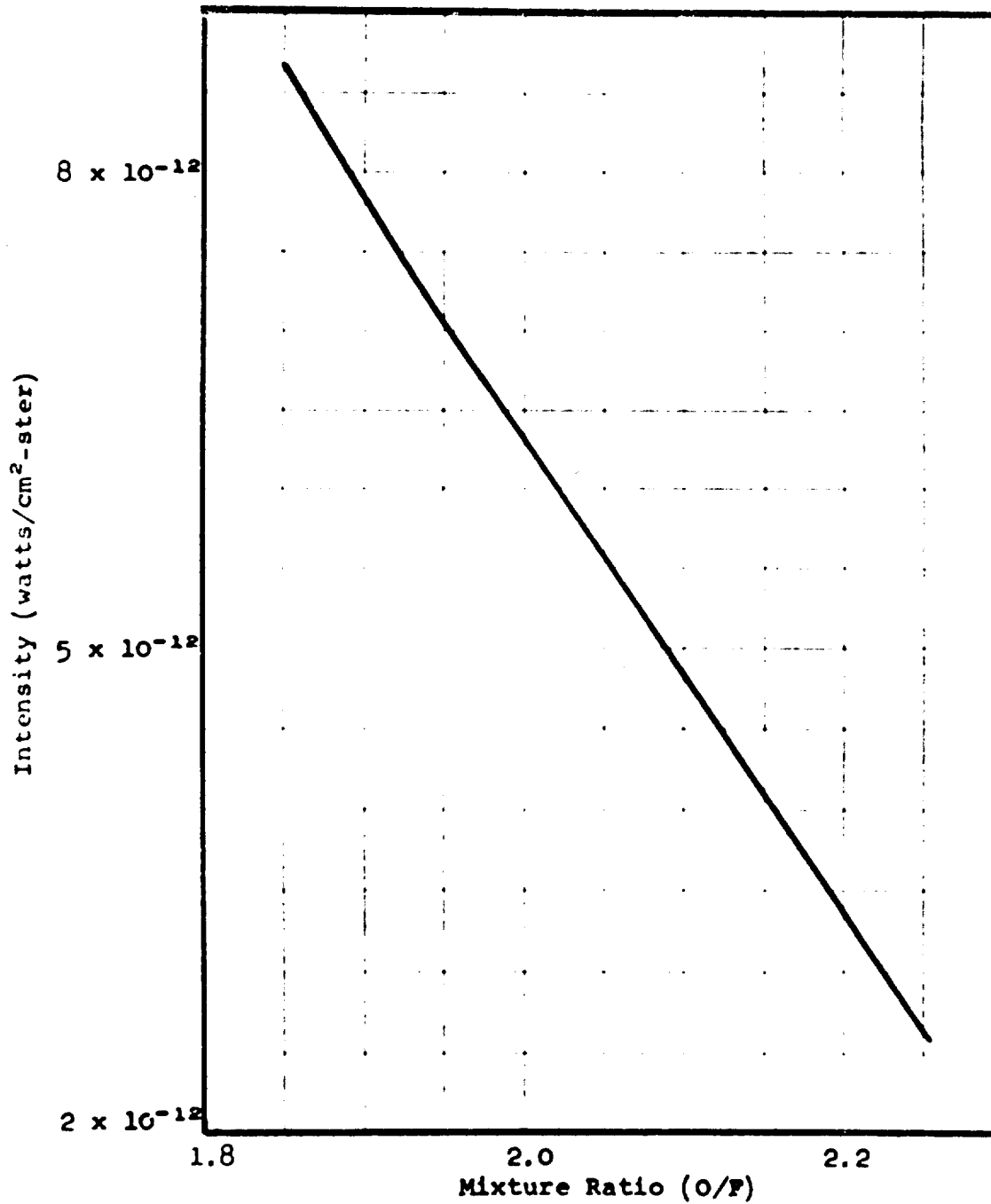


Figure 25. Theoretical Intensity of CH 3145.4 \AA vs Mixture Ratio for N_2O_4 /UDMH

The NH molecule at 2358.8Å displays the same characteristics as the CH molecule namely a linear relationship between I and O/F ratio with I decreasing with increasing O/F as can be seen in Figure 26. The peak intensity for the NH molecule radiating at this wavelength is 4.5×10^{-6} watts/cm²-ster. This intensity decreases with increasing O/F ratio to a value at approximately 75% of the peak intensity at O/F of 2.25. The value of the slope (or sensitivity) S is 3×10^{-6} .

Intensities obtained for the CO molecule at 2455.5 and 2433.6Å, the latter intensity running about 5% lower over the range of O/F ratios considered, are shown in Figure 27. In both cases the intensity remained relatively constant over the range $1.85 < O/F < 2.0$ and decreased over the range $2.0 < O/F < 2.25$ to approximately 75% of the peak intensity of 1.08×10^{-7} watts/cm³-ster (for 2455.5Å). It should be noted that these values are based upon the assumed value of the oscillation strength f.

Radiation intensities were calculated at five different wavelengths for the CHO molecule and are presented in Figure 28. The curves followed the same trend as those obtained for CH and NH, i.e., decreasing intensity with O/F ratio, however at the lower wavelengths (higher intensities) the curves exhibit a bit more non-linearity. The peak intensity of the most intense band (3108.2Å) was 5.9×10^{-8} watts/cm³-ster. The intensity dropped off to approximately 58% of this value at O/F = 2.25. S was approximately 6×10^{-7} , and decreased to 4×10^{-7} at the lower intensity bands.

The CN molecule radiant intensities were obtained for eight different wavelengths four of which (the most intense) are presented in Figure 29. The most intense emitting wavelength was 3876.3Å the peak value for which is 6.8×10^{-7} watts/cm³-ster. The four peak intensities were within 25 percent of one another. The general trend shown is similar to that displayed by the CHO molecule (namely I is inversely proportional to O/F ratio) with the exception that the slope decreases with increasing O/F ratio for the CN molecule, whereas the slope increases with increasing O/F ratio for the CHO molecule. The percent decrease in I over the O/F range considered was 59 percent for the 3876.3Å band. The value of S for this band was 1×10^{-6} .

Radiation due to the NO molecule at nine different wavelengths (of the 34 calculated) are presented in Figure 30. The highest intensity occurring at the lowest wavelength 2362.8Å. All nine curves are similar, the magnitude of the intensity increasing with increasing mixture ratio. The salient feature of these results is that NO is the only specie displaying this characteristic other than the OH molecule. This trend is influenced by the role the absorption factor plays in the intensity value. The intensity increased (nearly doubled) from the value at O/F = 1.85 to the peak intensity of 1.65×10^{-5} watts/cm³-ster at O/F = 2.25 (stoichiometry). The shape of the curve indicates that the peak intensity is not reached at stoichiometric O/F. The curves are seen to be slightly nonlinear. The spread in intensity from the most intense to the least intense of the nine bands presented here is approximately one order of magnitude.

Values were obtained for the OH molecule from the computer program described. However, the computer program does not consider absorption which

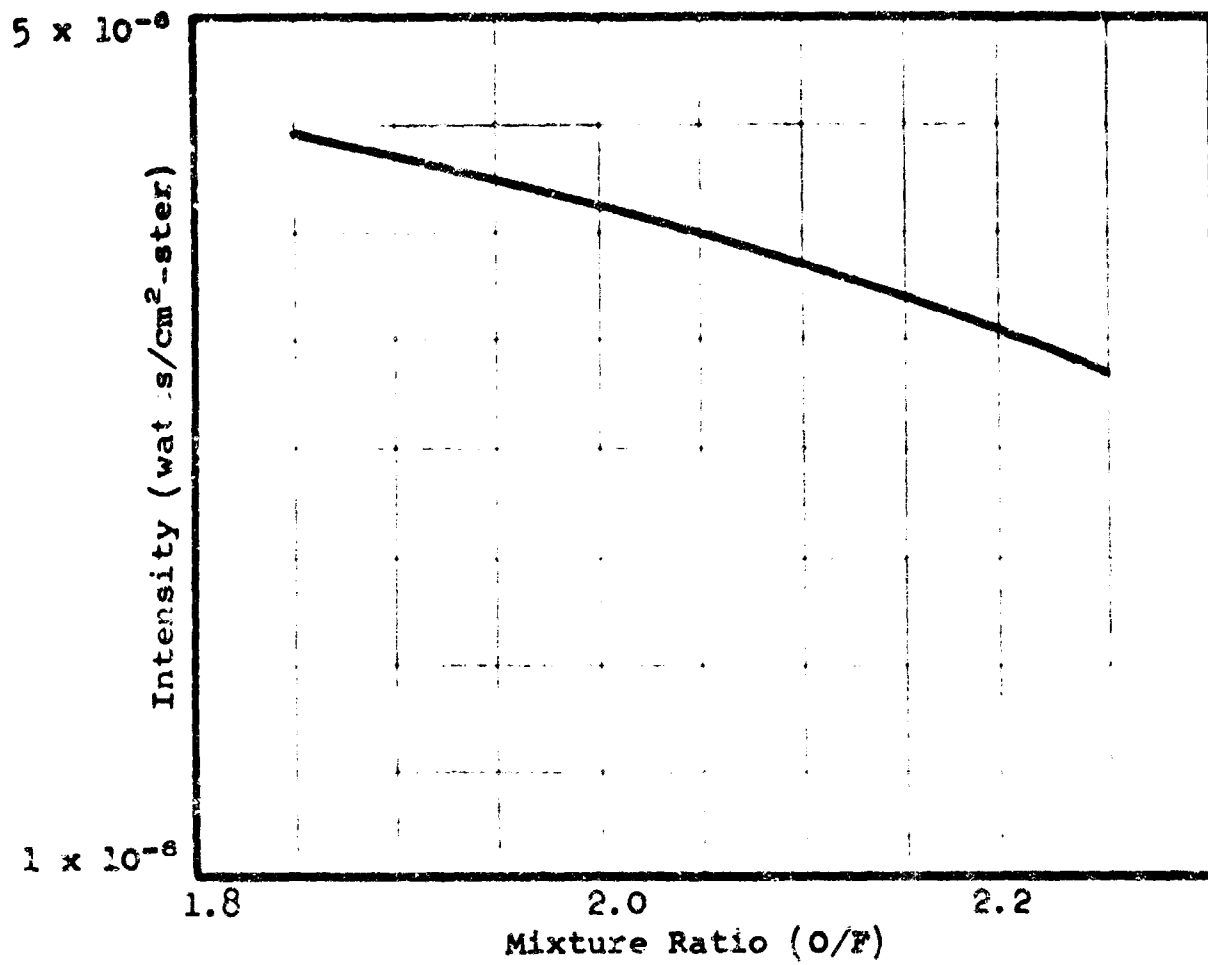


Figure 26. Theoretical Intensity of NH 3358.8 \AA vs Mixture Ratio for N_2O_4 /UDMH

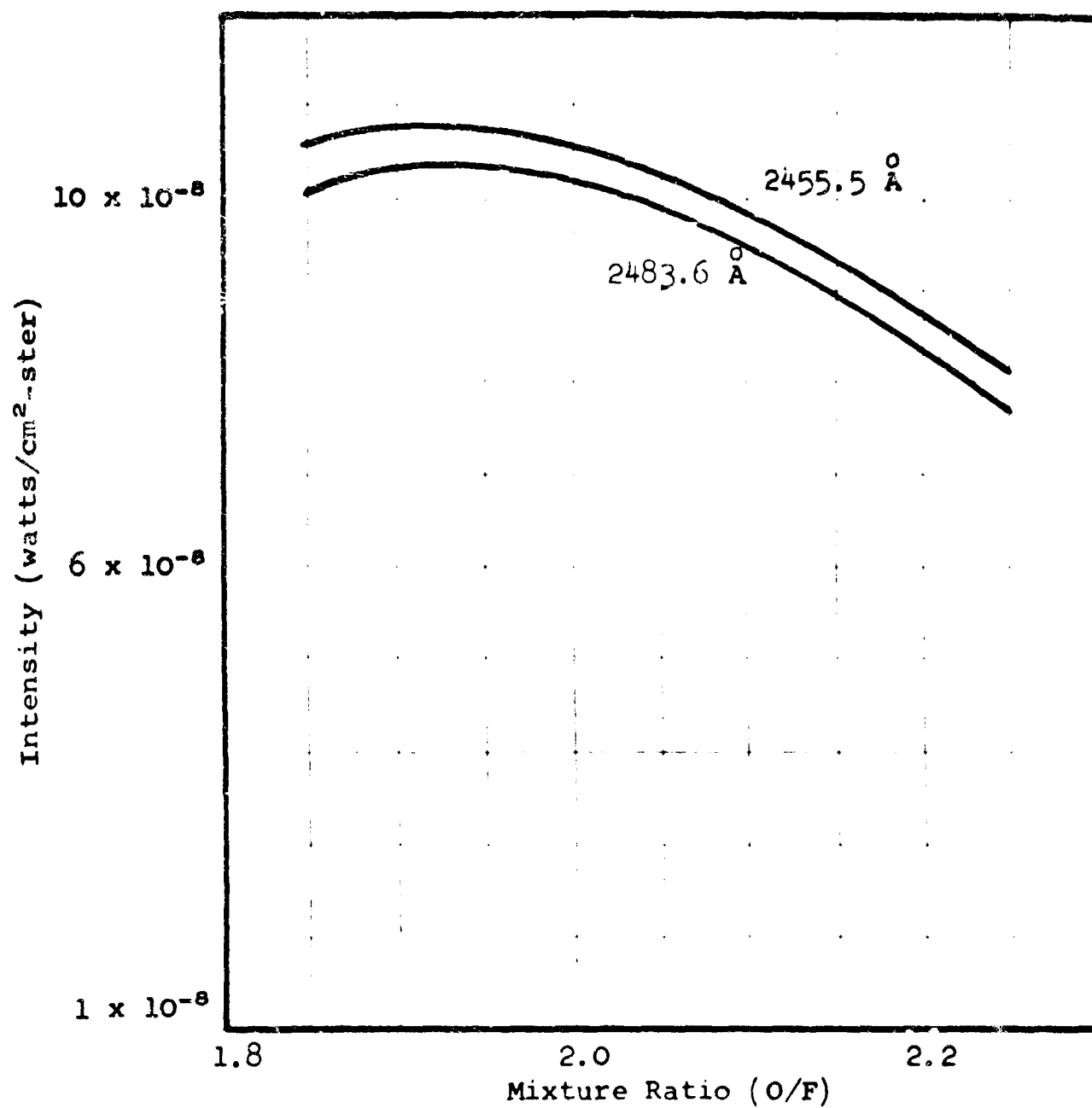


Figure 27. Theoretical Intensity of CO Bands vs Mixture Ratio for $\text{N}_2\text{O}_4/\text{UDMH}$

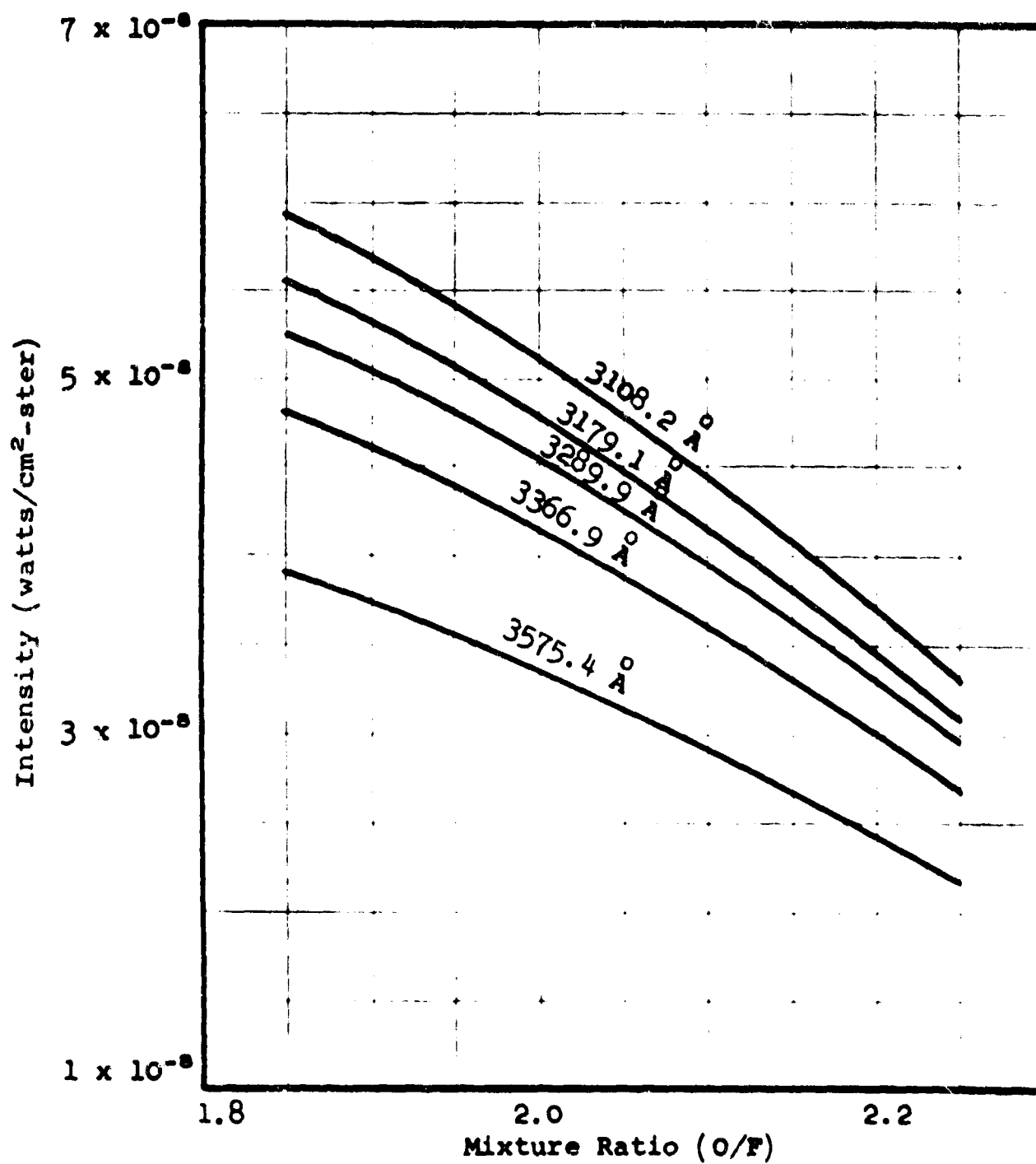


Figure 28. Theoretical Intensity of CHO Bands vs Mixture Ratio for N₂O₄/UDMH

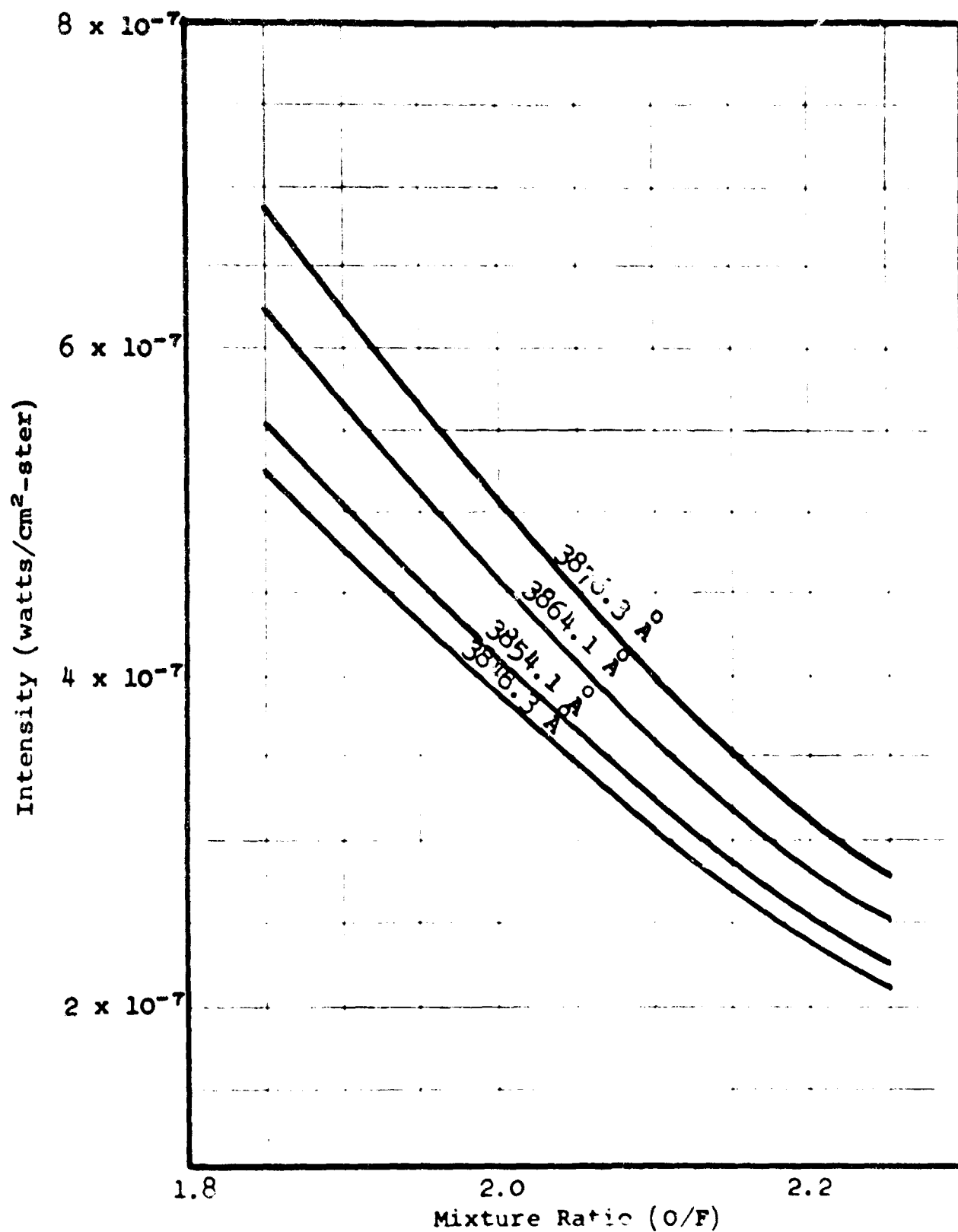


Figure 29. Theoretical Intensity of CN Bands vs Mixture Ratio for $N_2O_4/UDMH$

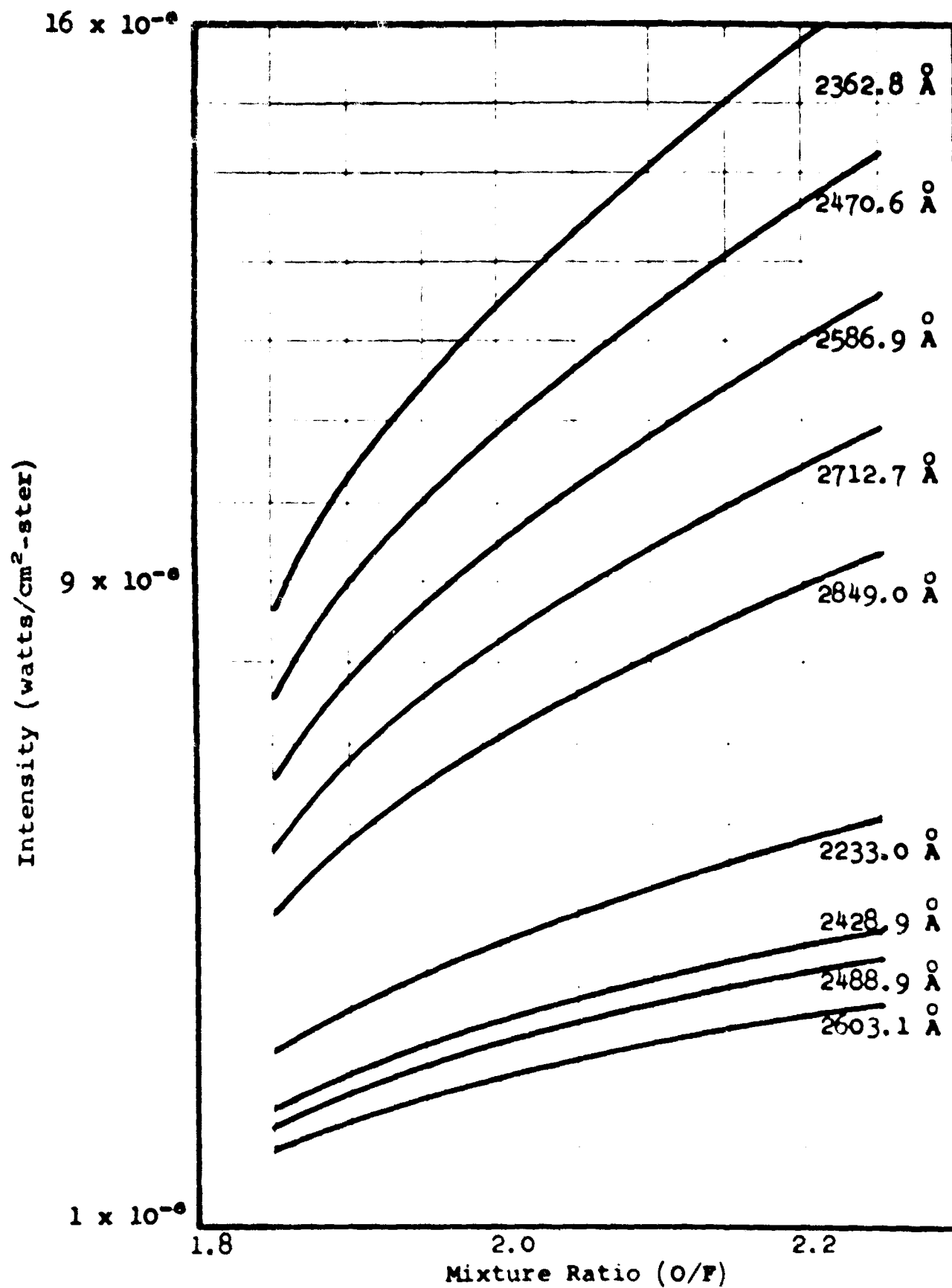


Figure 30. Theoretical Intensity of NO Bands vs Mixture Ratio for N₂O₄/UDMH

plays a large part in the radiant intensity emitted by this specie in the UV. The self absorption is high and thus these values must be decreased by the factor $e^{-\tau/\Delta\nu}$ where τ is the optical thickness calculated from the absorption coefficient (K_ν) and the plume thickness (l). That is, the equations programmed were derived assuming an optically thin homogeneous source. The radiation intensity for this homogeneous thin radiation source is proportional to the thickness of the radiating layer. For a homogeneous source where absorption becomes important, the radiation intensity is dependent upon the absorption factor $e^{-\tau/\Delta\nu}$ where τ is the optical thickness of the radiating source. For a thick radiator approaching blackbody emission the radiation is independent of the thickness and is given by:

$$B_\nu = \frac{2h\nu^3}{c^2} \left(\frac{1}{e^{h\nu/KT}-1} \right)$$

Since the self absorption for the OH molecule is high, it will radiate as a blackbody at the corresponding exhaust temperature T , and therefore the equation above was used to calculate the spectral blackbody OH intensities in addition to the computer program.

The values shown in Figure 31 are uncorrected for absorption. The trend of I vs O/F ratio is similar to that of the NO bands. When absorption is taken into account in the blackbody calculations, the shape of the curves and their trend change as shown in Figure 32 since each point on the curve represents a different set of rocket engine exhaust conditions. The intensity is seen to peak at 1.5×10^{-6} for 3064\AA and for all three bands at O/F = 2.05, decreasing slightly (8%) with increasing or decreasing O/F ratio. The f value was assumed for the OH band radiating at 2602\AA .

The results of all bands presented are summarized in Table 16, which give the radiant intensities emitted by the specie indicated, at the wavelength indicated and over the range of mixture ratios considered for the N_2O_4 /UDMH propellant system.

B. EXPERIMENTAL INTENSITY VS MIXTURE RATIO

Data previously obtained at Astrosystems has been correlated to demonstrate the effects of O/F ratio variation on radiation intensity for several propellant combinations. These data are presented in Figures 33-42 and summarized in Table 17.

Figures 33 and 34 show the relationship between O/F and I for LO_2 /RP-1 propellant at 215,000 and 110,000 feet respectively. Note that the intensities peak before the stoichiometric O/F ratio of 3.4 is reached. The scan (1000-5000 \AA) at the lower altitude produced intensities on the order of 500 times the intensity of the 2811\AA OH band at 215,000 feet. This altitude effect was not observed with LO_2 /NII₃ propellant for the 2811\AA OH band, as can be seen from the data presented in Figure 35.

The relationship of spectral emission intensity to mixture ratio, for each of three radiating molecules, was studied at three altitudes. The

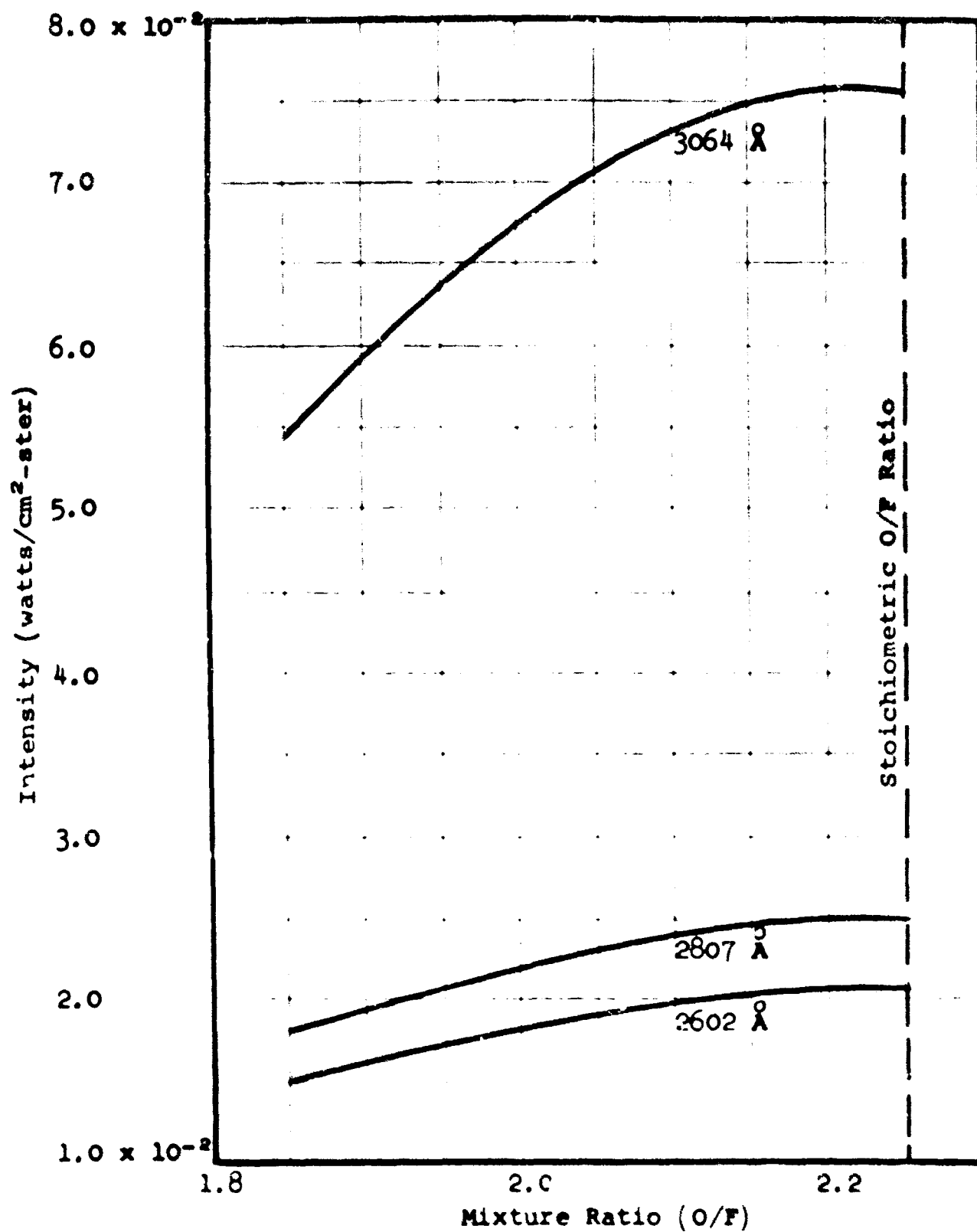


Figure 31. Theoretical Blackbody Radiant Intensity of OH Bands vs Mixture Ratio for $\text{H}_2\text{O}_2/\text{UDMH}$

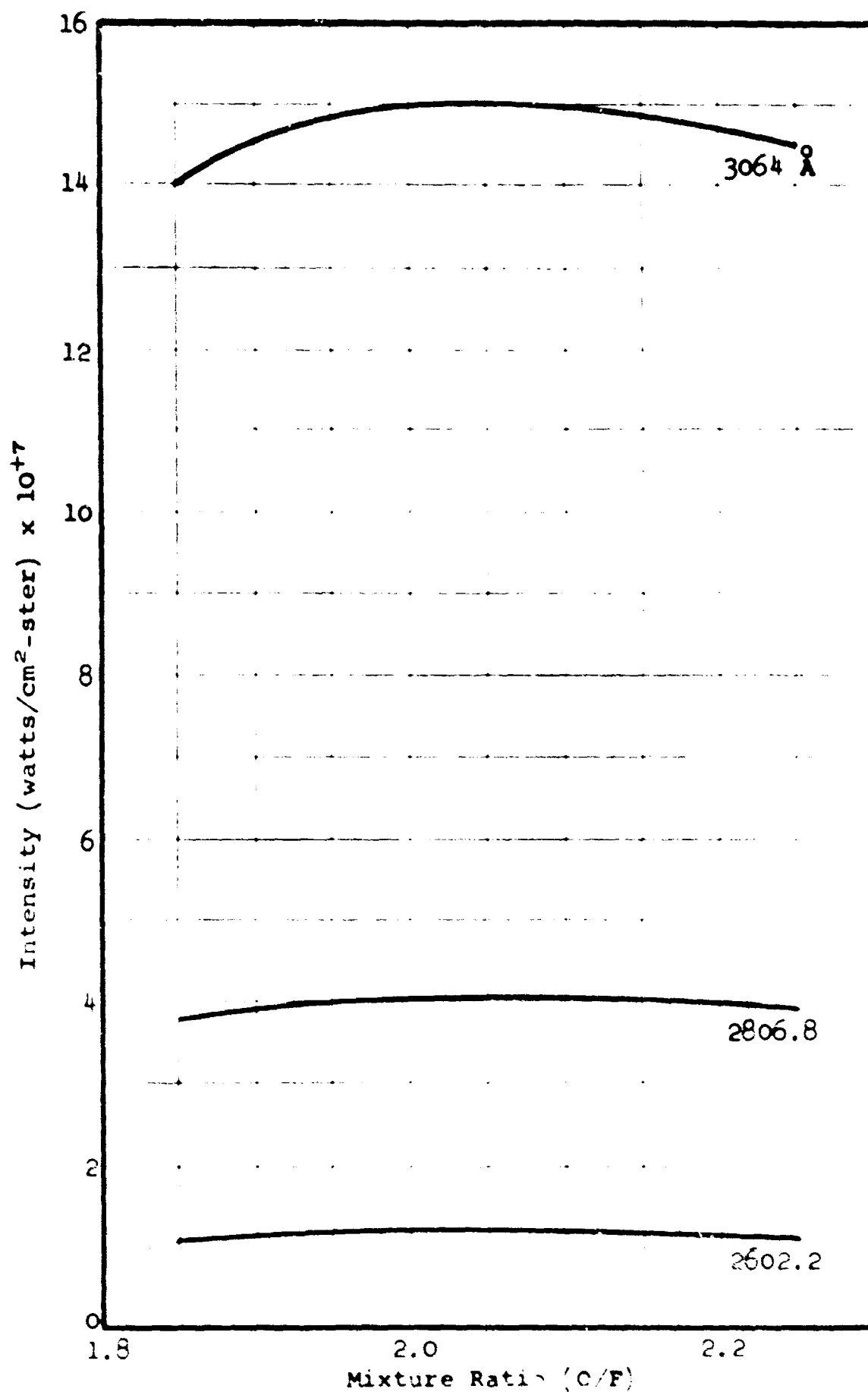


Figure 32. Theoretical Intensity of OH Bands vs Mixture Ratio for N₂O₄/UDMH

TABLE 16

SUMMARY OF N_2O_4 /UDMH SPECIES
RADIANT INTENSITIES VS MIXTURE RATIO

| Specie | λ (Å) | Peak I | I_{min}/I_{max} (%) | Slope(S) |
|--------|---------------|------------------------|-----------------------|----------------------|
| CH | 4315.3 | 2.32×10^{-10} | 30 | -4×10^{-10} |
| NH | 3358.8 | 4.50×10^{-6} | 75 | -3×10^{-6} |
| CO | 2455.5 | 1.08×10^{-7} | 75 | - |
| CHO | 3108.2 | 5.90×10^{-8} | 58 | -6×10^{-7} |
| CN | 3876.3 | 6.80×10^{-7} | 59 | -1×10^{-6} |
| NO | 2362.8 | 1.65×10^{-5} | 52 | $+2 \times 10^{-5}$ |
| OH | 3064.0 | 1.50×10^{-6} | 94 | - |

FIGURE 33

O₂/RP PLUME RADIANT INTENSITY
AT 2811 Å VS. MIXTURE RATIO
(215,000 FT ALTITUDE)

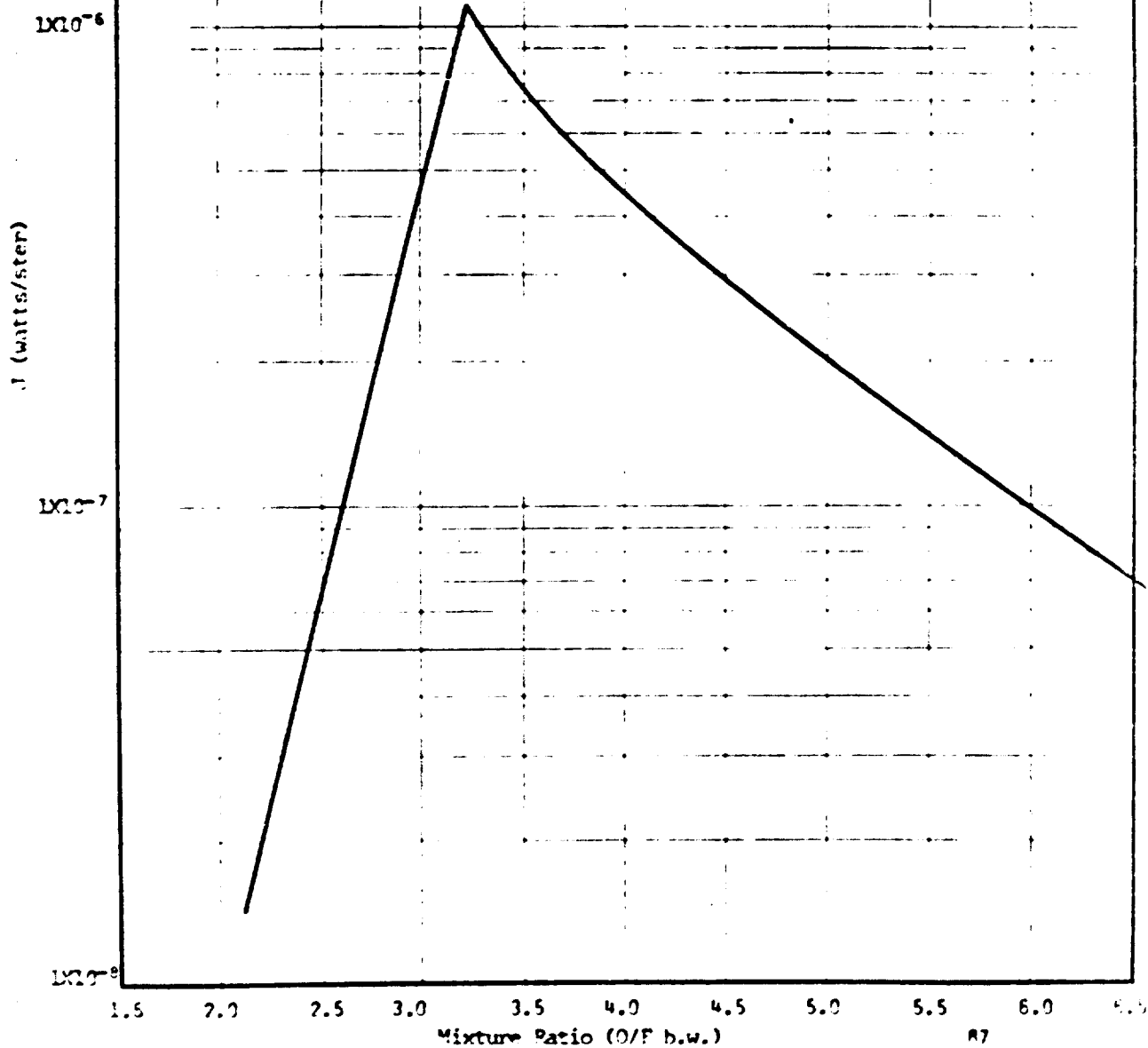


FIGURE 34

O₂/FP PLUME RADIANT INTENSITY
(1000 - 5000 Å) VS. MIXTURE RATIO
(110,000 FT ALTITUDE)

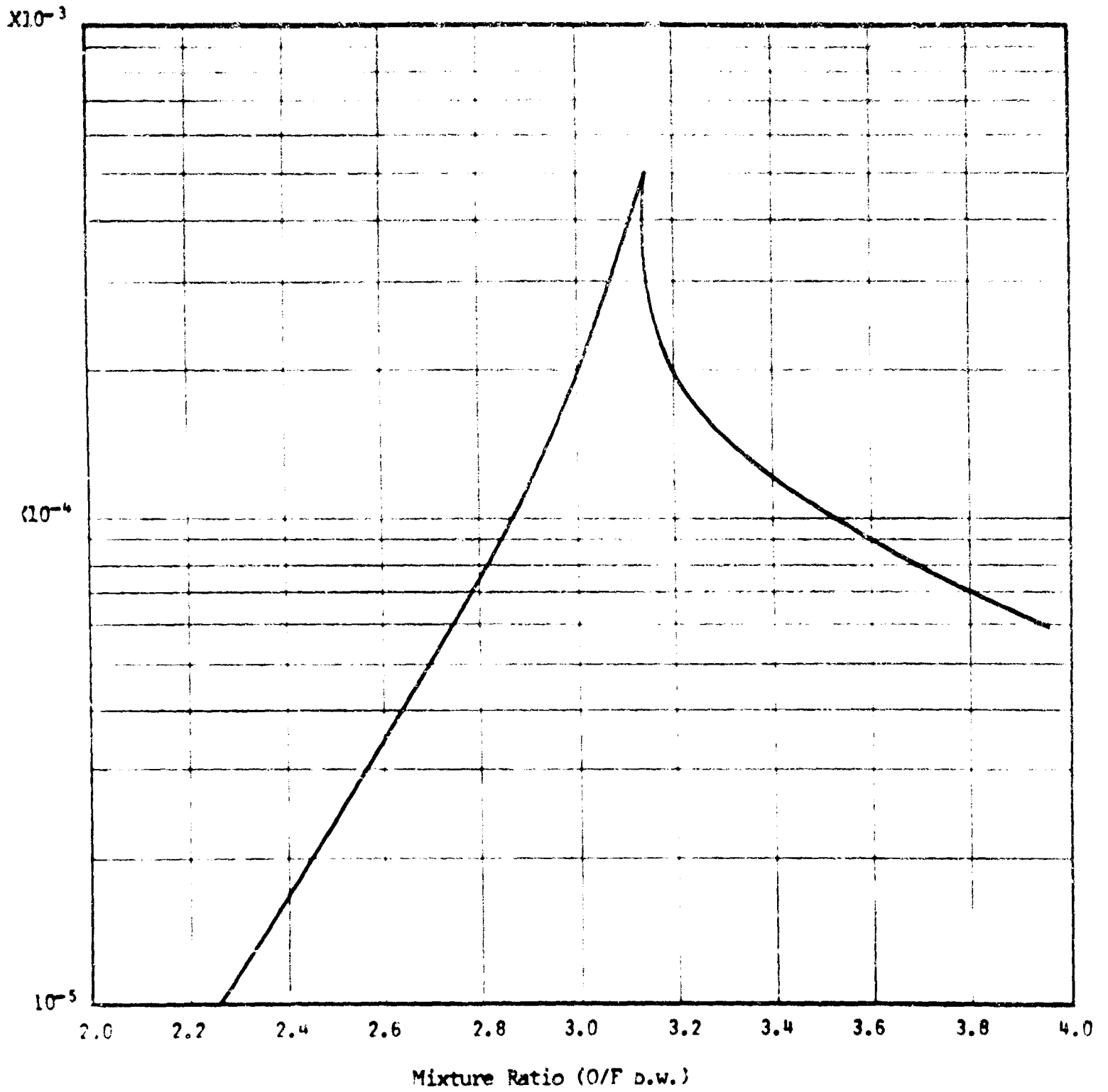


FIGURE 35

O_2/NH_3 PLUME RADIANT INTENSITY COMPILATION
($2^{\circ}11'$ BAND) VS. MIXTURE RATIO AT THREE ALTITUDES

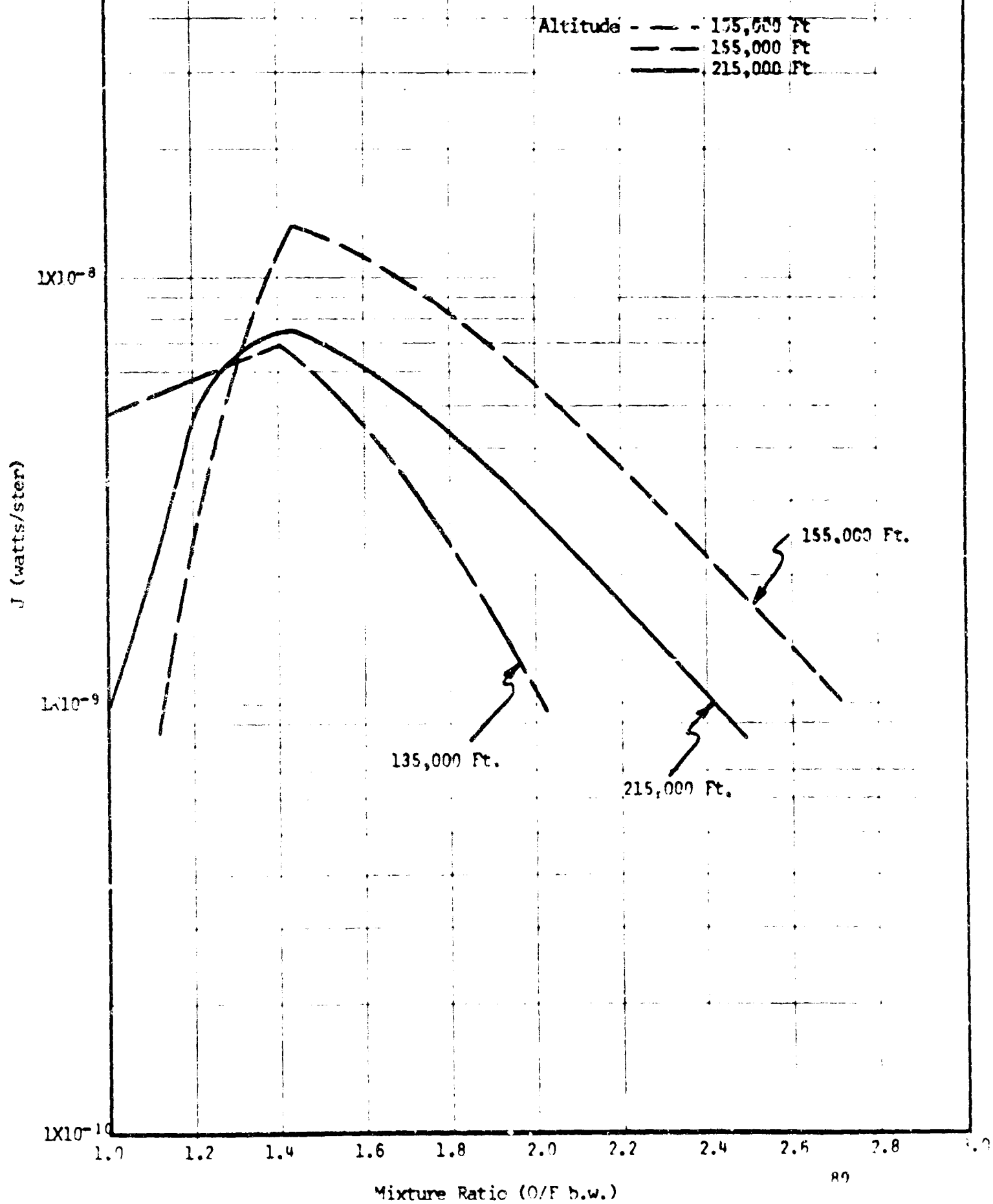
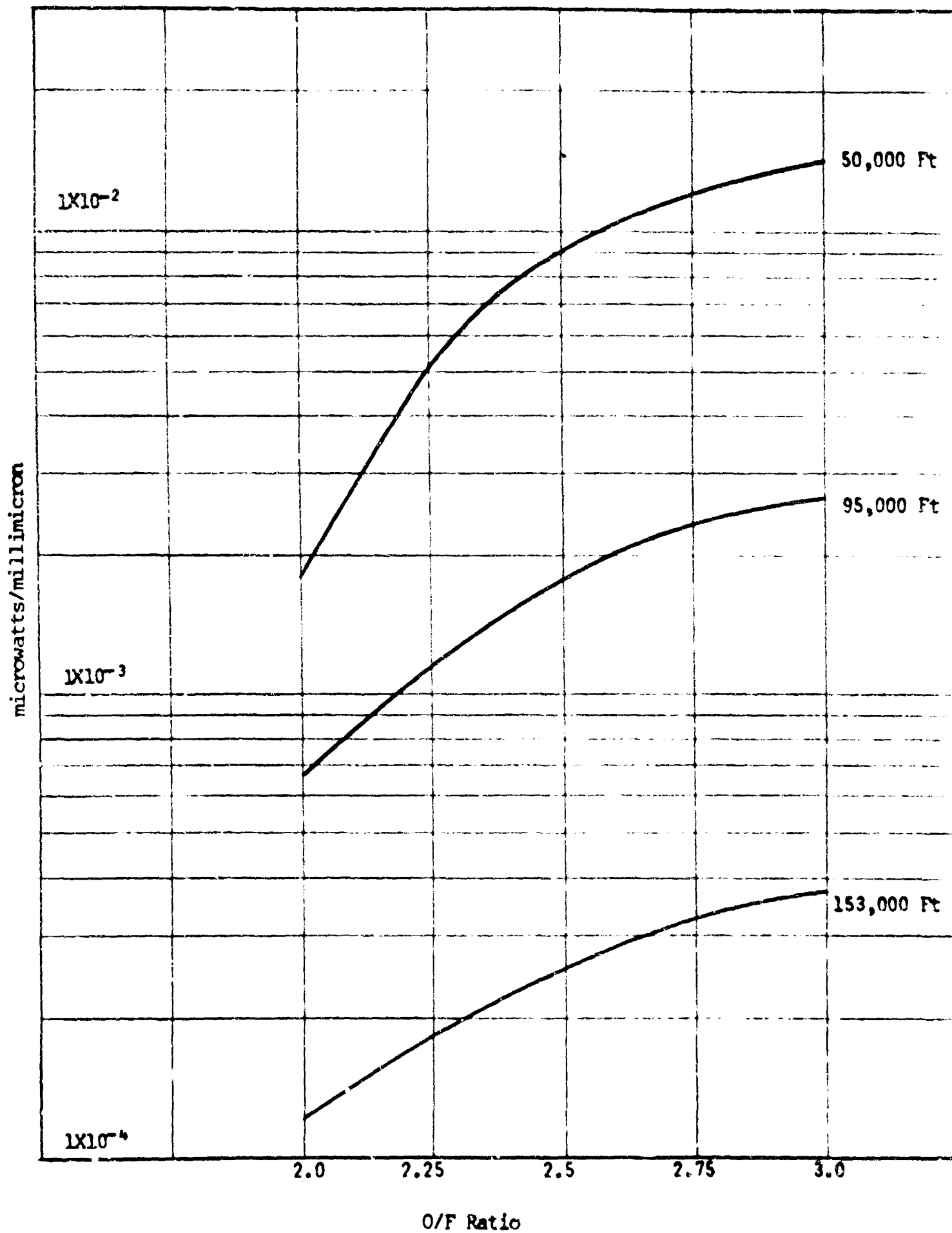


FIGURE 36

ABSOLUTE INTENSITY OF 3100 Å OH
VS. O/F RATIO FOR THREE ALTITUDES



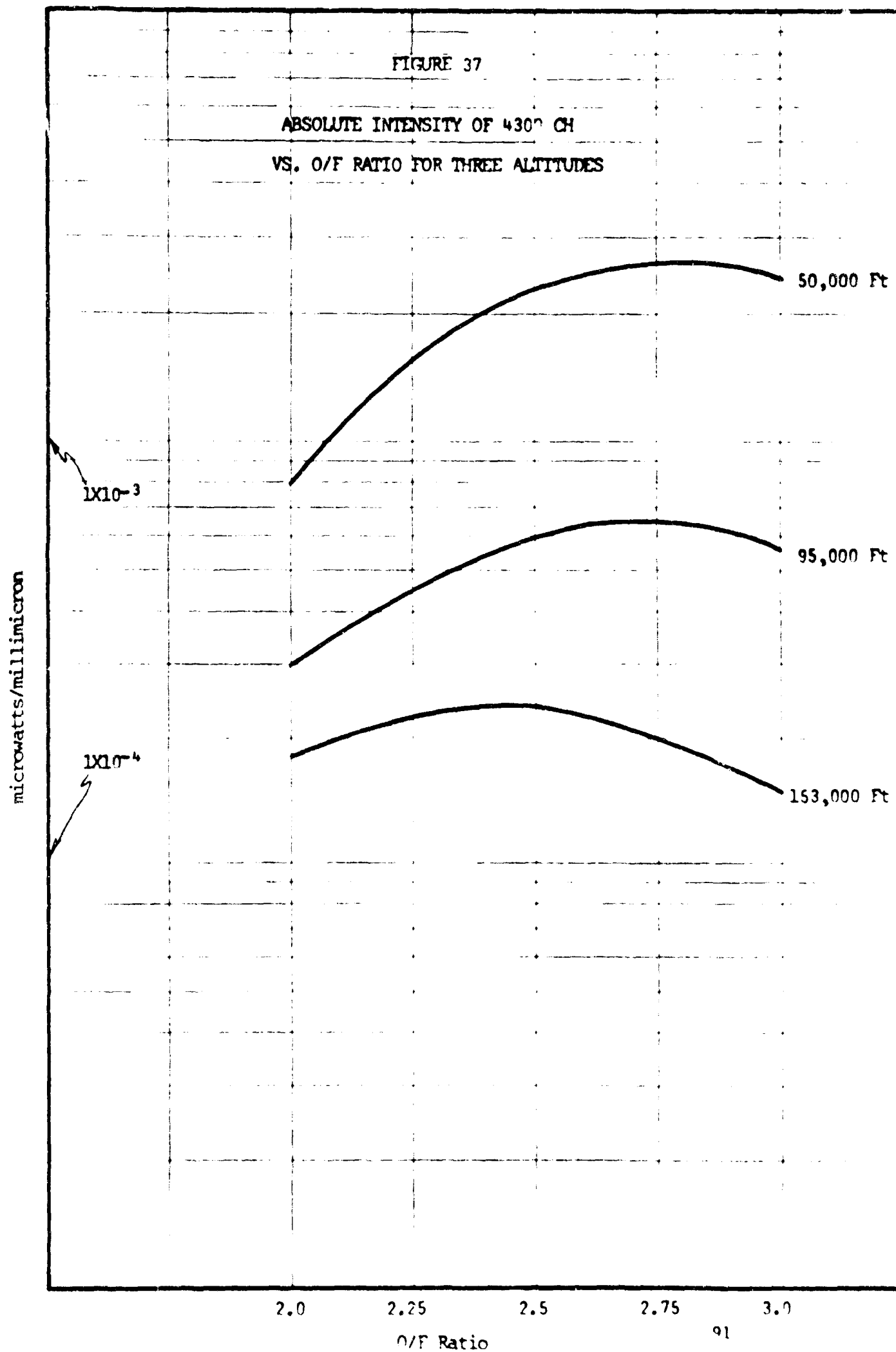


FIGURE 38

ABSOLUTE INTENSITY OF $4700 \text{ \AA } C_2$
VS. O/F RATIO FOR THREE ALTITUDES

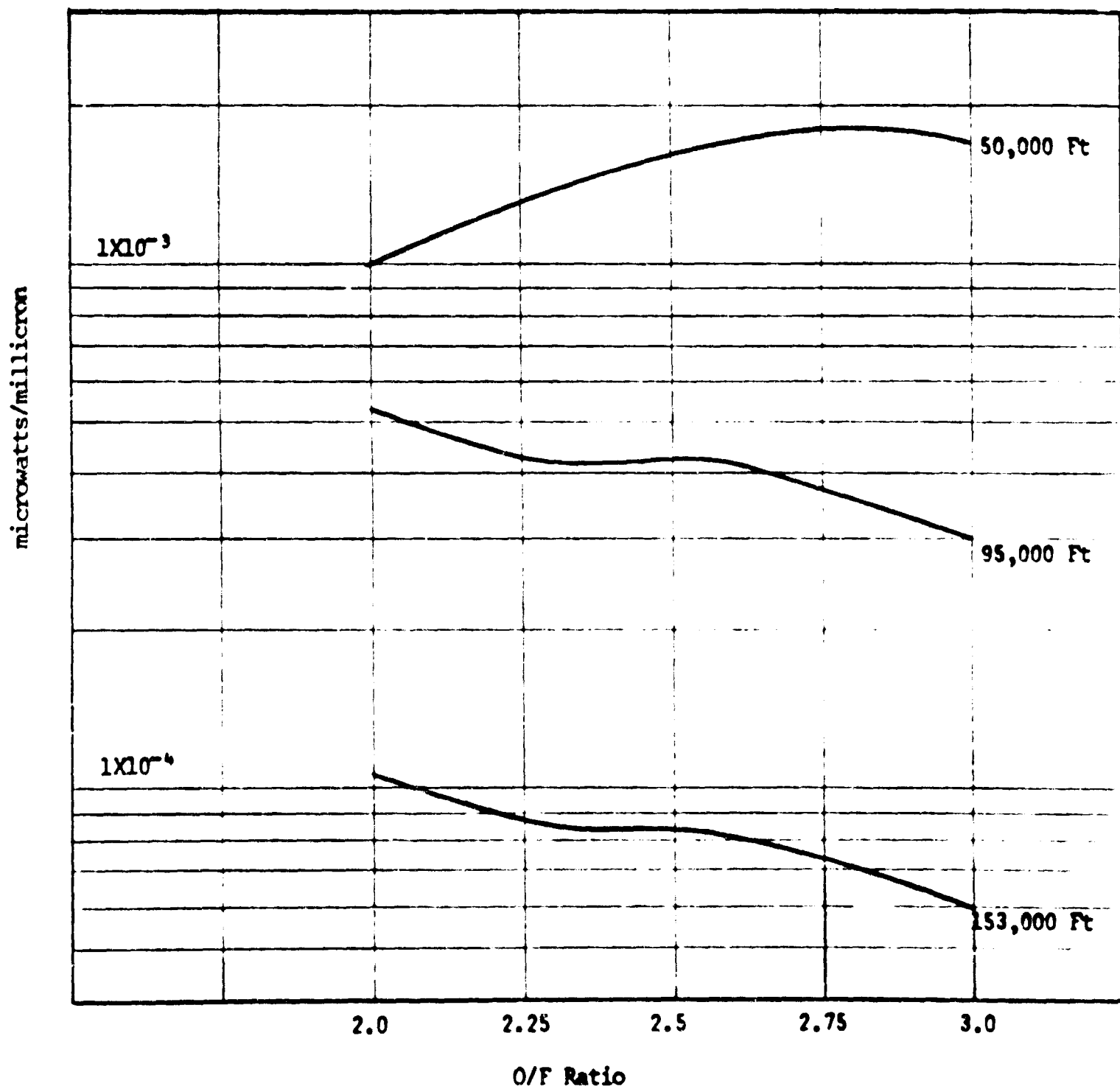
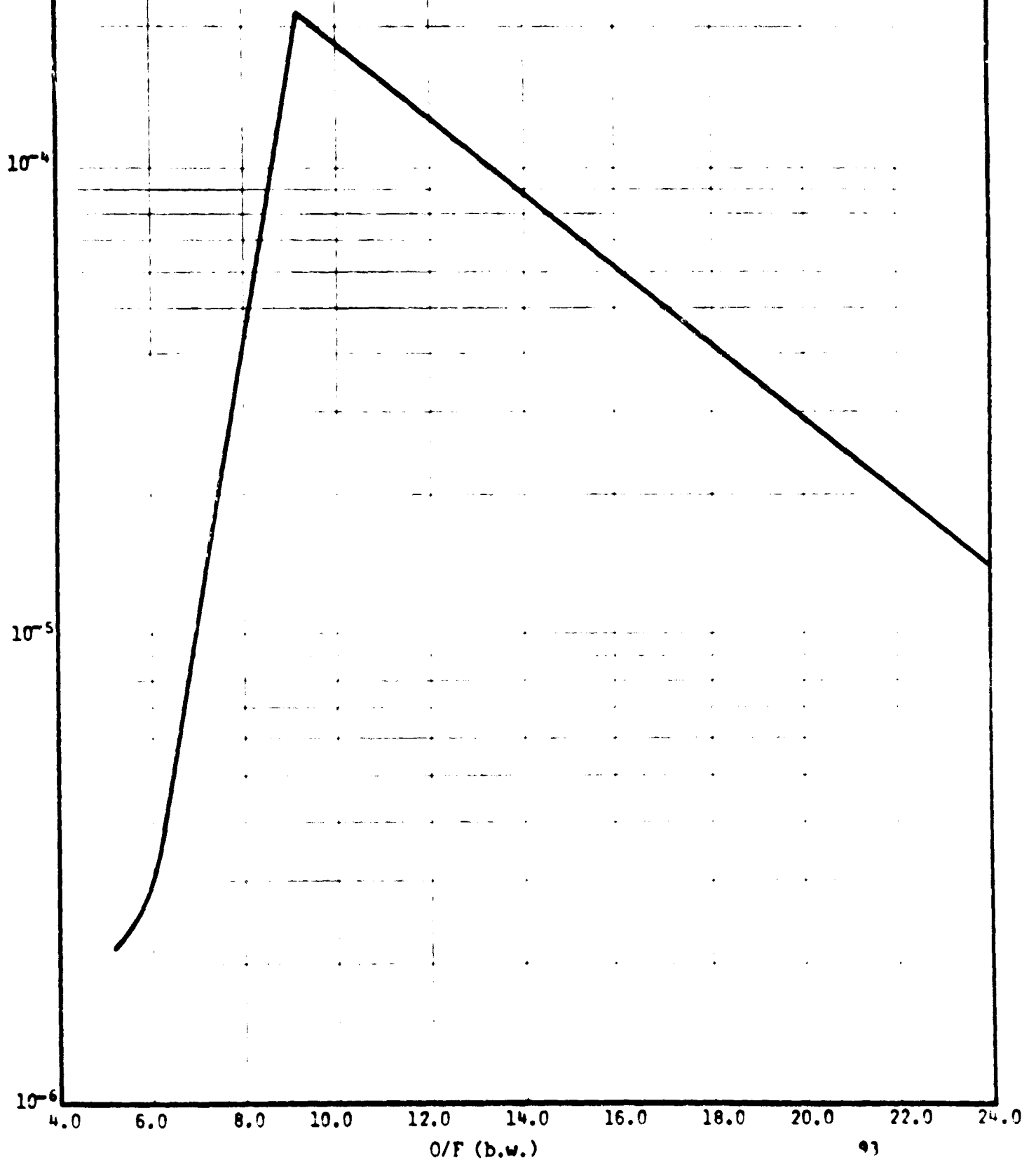


FIGURE 39

O_2/H_2 PLUME RADIANT INTENSITY (3075 Å)
VS. MIXTURE RATIO (ALTITUDE - 80,000 FT)



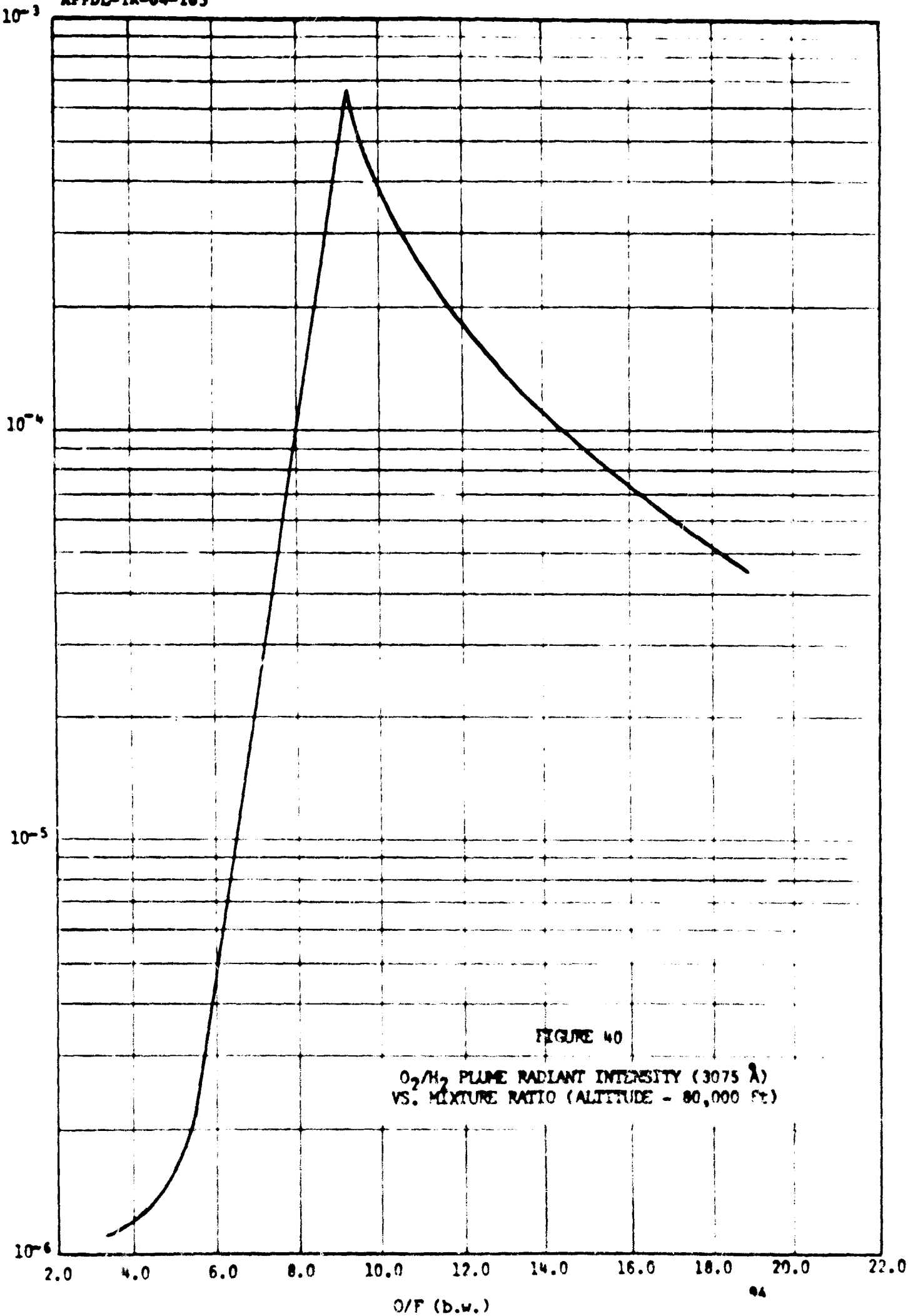
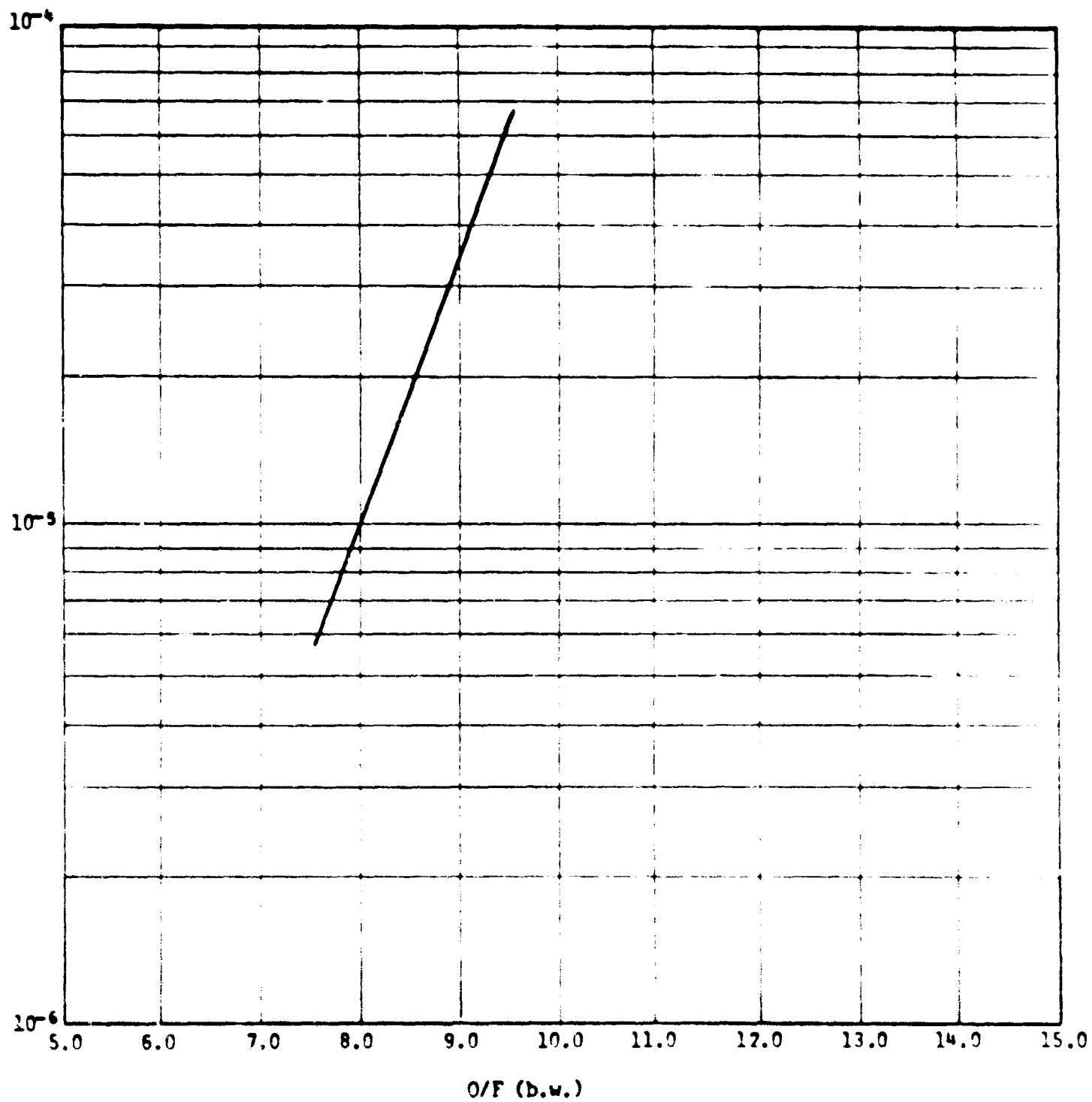


FIGURE 40

O_2/H_2 PLUME RADIANT INTENSITY (3075 \AA)
VS. MIXTURE RATIO (ALTITUDE - 80,000 FT)

FIGURE 41

O_2/H_2 PLUME RADIANT INTENSITY (3075 Å) VS.
MIXTURE RATIO (Altitude 136,000 Ft)



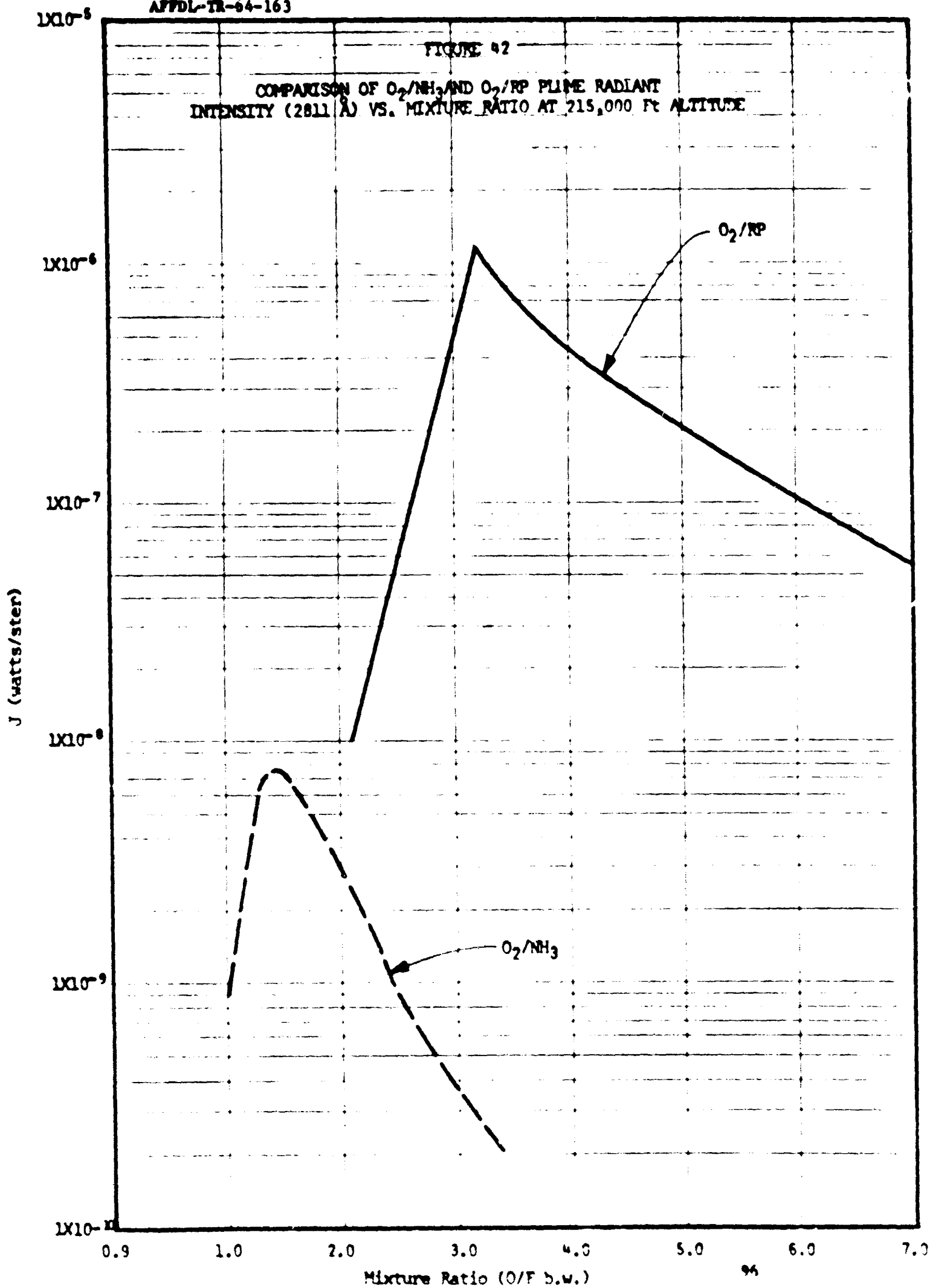


TABLE 17
EFFECT OF MIXTURE RATIO VARIATION ON RADIATION INTENSITY - EXPERIMENTAL RESULTS

| Propellant | Figure No. | O/P Range | O/P at I_{\max} | I_{\max} ($\frac{\text{watts}}{\text{ster}}$) | Altitude (ft) $\times 1000$ | Radical | Band (\AA) |
|-------------------------------|------------|-----------|-------------------|---|--------------------------------|-------------------|------------------------|
| O_2 -RP1 | (12) | 2.1-6.7 | 3.2 | 1×10^{-6} | 215 | OH | 2811 \AA |
| O_2 -RP1 | (13) | 2.25-4.0 | 3.14 | 5×10^{-4} | 110 | OH | 1000-5000 \AA |
| O_2 -RP1 | (15) | 2-3 | 3.0 | 1.4×10^{-2} * | 50 | OH | 3100 \AA |
| O_2 -RP1 | (15) | 2-3 | 3.0 | 2.7×10^{-3} * | 95 | OH | 3100 \AA |
| O_2 -RP1 | (15) | 2-3 | 3.0 | 3.7×10^{-4} * | 153 | OH | 3100 \AA |
| O_2 -RP1 | (16) | 2-3 | 2.75 | 2.6×10^{-3} * | 50 | CH-C ₂ | 4300 \AA |
| O_2 -RP1 | (16) | 2-3 | 2.75 | 6.5×10^{-4} * | 95 | CH-C ₂ | 4300 \AA * |
| O_2 -RP1 | (16) | 2-3 | 2.5 | 2.4×10^{-4} * | 153 | CH-C ₂ | 4300 \AA |
| O_2 -RP1 | (17) | 2-3 | 2.75 | 1.8×10^{-3} * | 50 | C ₂ | 4700 \AA |
| O_2 -RP1 | (17) | 2-3 | 2.0 | 5.2×10^{-4} * | 95 | C ₂ | 4700 \AA |
| O_2 -RP1 | (17) | 2-3 | 2.0 | 1.1×10^{-4} * | 153 | C ₂ | 4700 \AA |
| O_2 -NH ₃ | (14) | 1-2.4 | 1.41 | 8×10^{-9} | 215 | OH | 2800 \AA |
| O_2 -NH ₃ | (14) | 1-1.5 | 1.41 | 1.2×10^{-8} | 155 | OH | 2800 \AA |
| O_2 -NH ₃ | (14) | 1-2.6 | 1.41 | 6.8×10^{-9} | 135 | OH | 2800 \AA |
| O_2 -H ₂ | (18) | 5-23 | 9.2 | 2.1×10^{-4} | 80 | OH | 3075 \AA |
| O_2 -H ₂ | (19) | 3.2-19 | 9.2 | 6.7×10^{-4} | 80 | OH | 3075 \AA |
| O_2 -H ₂ | (20) | 5-24 | 9.5 | 7×10^{-5} | 136 | OH | 3075 \AA |
| O_2 -H ₂ | (21) | 3-19 | 9.4 | 1.6×10^{-7} | 87 | OH | 3100 \AA |
| O_2 -H ₂ | (22) | 7.5-9.3 | 9.3 | 2.4×10^{-7} | 87 | OH | 3100 \AA |

*Units of starred quantities are μ watts/millimicron

radiating molecules included were OH, CH, and C_2 at the selected principal wavelengths of 3100Å, 4300Å and 4700Å, respectively. For the OH molecule it can be seen from Figure 36 that the emission intensity increases with increasing O/F ratio ($2 \leq O/F \leq 3$) in a similar manner at all three altitudes tested, and seems to peak at $O/F = 3.0$. The emission intensity from the CH molecule at 4300Å (shown in Figure 37) indicates a definite peak in intensity at all three altitudes tested. The intensity peaks at lower O/F ratios with increasing altitude. The difference in intensities between the lower and higher altitudes is one order of magnitude. Also, absolute intensities of the C_2 molecule at 4700Å is shown as a function of mixture ratio in Figure 38.

For O_2/H_2 propellant (at 3075Å) the radiation intensity peaked at O/F ratios higher (> 9.0) than the stoichiometric value of 7.94, at altitudes of 80,000 and 136,000 feet (see Figures 39-41). Figure 42 is a comparison of the plume radiant intensities for two propellants (O_2/RP and O_2/NH_3) as a function of propellant mixture ratio at an altitude of 215,000 feet.

C. APPLICABILITY OF SEEDING

In a practical case if seeding of a bipropellant liquid engine were permitted, independent identification of oxidizer and fuel flow rates could be simplified somewhat. Such seeding need not be deleterious to rocket engine performance assuming small amounts ($< 1\%$) were employed and the seeding ingredients were in themselves active oxidizers and fuels.

A good example of active seeding compounds are lithium nitrate and trimethylborate. Trimethylborate (trimethoxyborine) $B(OCH_3)_3$ is a colorless liquid, commercially available, m.p. $-29^\circ C$, b.p. $68.7^\circ C$ and miscible with all propellant fuels. The characteristic green emission bands of boron occur at 4715, 4930, 4950 and 5180Å. Lithium nitrate ($LiNO_3$) is soluble in many organic and inorganic liquids and notably in N_2O_4 . The sensitivity of flame emission of lithium is about 1000 times that of boron, so that a much lower concentration of tracer in the oxidizer will be sufficient. The characteristic red emission bands of lithium occur at 6104 and 6708Å.

The admixture of the tagging compounds can always be kept at a constant fraction of the tagged substance; hence, the intensity of the total flame will be related to the intensities of the characteristic green or red emission by the tracers. Therefore, it seems possible to discriminate between a change in mixture ratio and an accompanying change in flow rate of both propellants.

As a practical matter, the signals developed by the tracers could be handled as follows.

The radiation from the plume before being detected by photo-cells would be filtered (Wratten Filter No. 29, dominant transmitted wavelength at 6316Å and Wratten Filter No. 38A dominant transmitted wave length at 4789Å) to separate fuel contribution and oxidizer contribution to the flame emission. Separation could also be effected by a high efficiency dichroic

coating (Liberty Mirror Division, Libbey-Owens-Ford Glass Co., e.g., No. 90-720) which has a reflection of 12% at 5000Å and 91% at 6700Å and a transmission of 83% at 5000Å and of 8% at 6700Å. This system is much more stable than a gelatine Wratten filter.

The voltage signals from the two photocells with the separated emission responses would then be compared in a balanced circuit and the unbalanced signal would indicate the deviation of the mixture ratio from the normal balance.

SECTION 6

EXIT PLANE GAS TEMPERATURE ANALYSIS

Monitoring of rocket exhausts can be of great value in detecting engine partial failures or malfunctions such as valve inaccuracies, combustion instability, combustion chamber erosion (oxidation), etc. Changes in mixture ratio occasioned by such failures, which are not necessarily, although most probably accompanied by changes in flow rate (\dot{w}), can be detected by spectroscopic means. This technique, however, requires complete knowledge of how O/F ratio effects the combustion chamber temperature, which in turn affects the exhaust temperature. The latter in turn affects the radiation intensity and possibly the type of radiation that will be emitted from the plume. The following paragraphs of this report explore the interdependency of these variables, and present a method for determining exit plane gas temperature.

A. TEMPERATURE VS MIXTURE RATIO

The effects and sensitivity of changes in O/F to changes in nozzle exit exhaust temperature have been analyzed (in order to be able to determine the relationship between O/F and I) for three propellant combinations and a rocket engine nozzle with an expansion ratio of forty to one ($\epsilon=40$). These results are presented in Figures 43-45, from which it can be seen that the exhaust gas temperature increases with O/F ratio until the stoichiometric O/F ratio is reached. Upon further increase in O/F ratio the exhaust gas temperature decreases. From examination of the applicable radiation equations, the effects of changes in O/F ratio upon the radiation intensity emitted from the rocket exhaust can be attributed to the effects of changes in exhaust temperature and number density. These functional relationships between the nozzle exit plane temperature and number density on radiation intensity are given in the following paragraphs of this section.

B. FLOW RATE VS RADIATION INTENSITY

The effect of changes in flow rate on the radiation intensity (which will ultimately be monitored) is in essence a different problem than detecting changes in O/F ratio (which may remain unchanged during either a simultaneous increase or decrease in both w_o and w_f). That is changes in O/F ratio are predominantly radiation temperature effects on intensity, whereas changes in flow rate primarily produce a number density effect. This can be illustrated as follows.

The mass flow of rocket propellant into the rocket engine combustion chamber must equal the mass flow of the exhaust gases out of the rocket nozzle exit station. That is, the law of conservation of mass must apply, and the equation of continuity is applicable for analysis of the desired effects. This equation can be written for the flow at the nozzle exit station as follows:

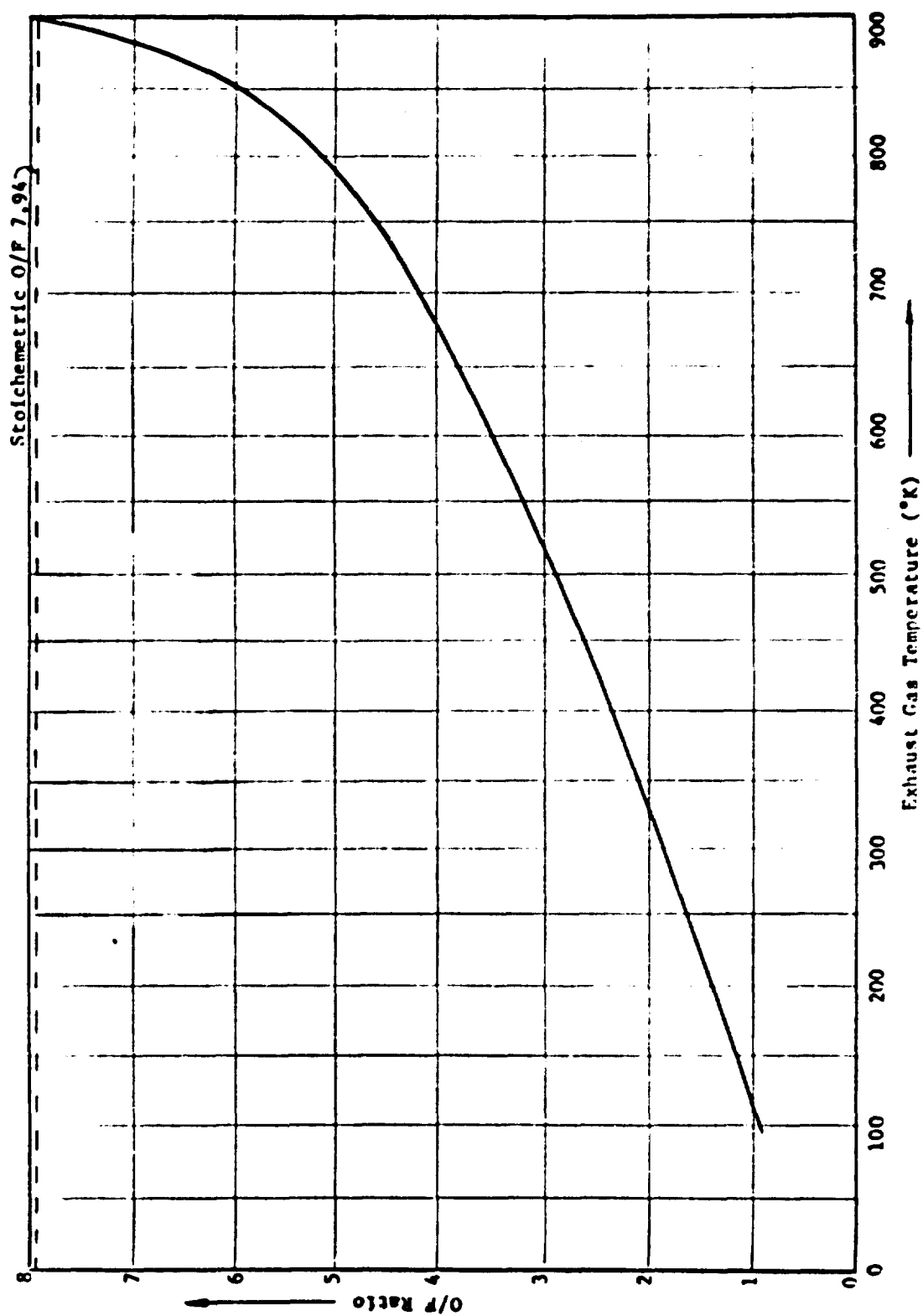


Figure 43. Oxygen-Hydrogen Exhaust Gas Temp. as a Function of Mixture Ratio for an Expansion Ratio of $\epsilon = 40$, $P_c = 60$ psia

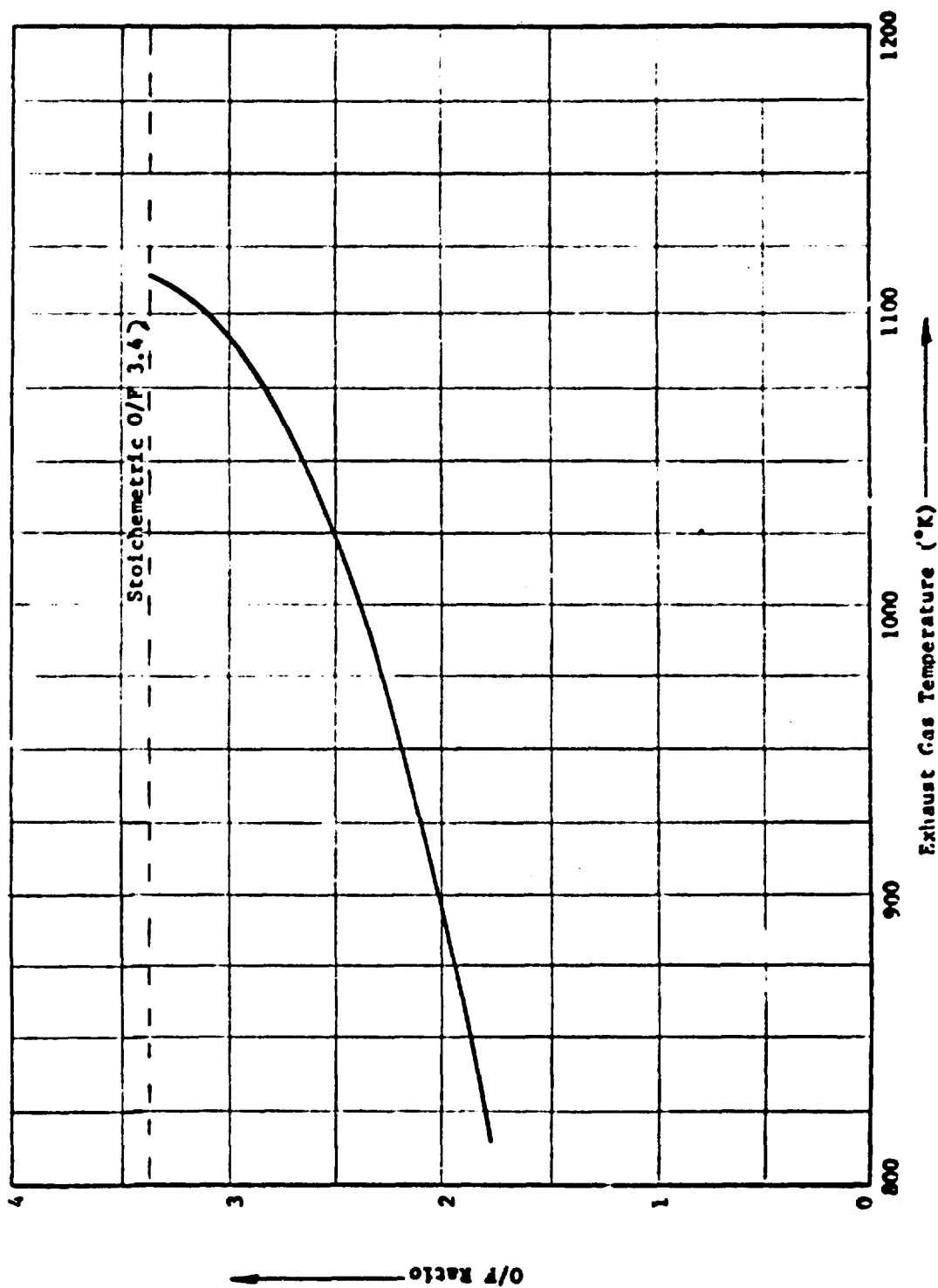


Figure 44. Oxygen - RP-1 Exhaust Gas Temperature as a Function of Mixture Ratio for an Expansion Ratio of $c = 40$, $P_c = 50$ psia

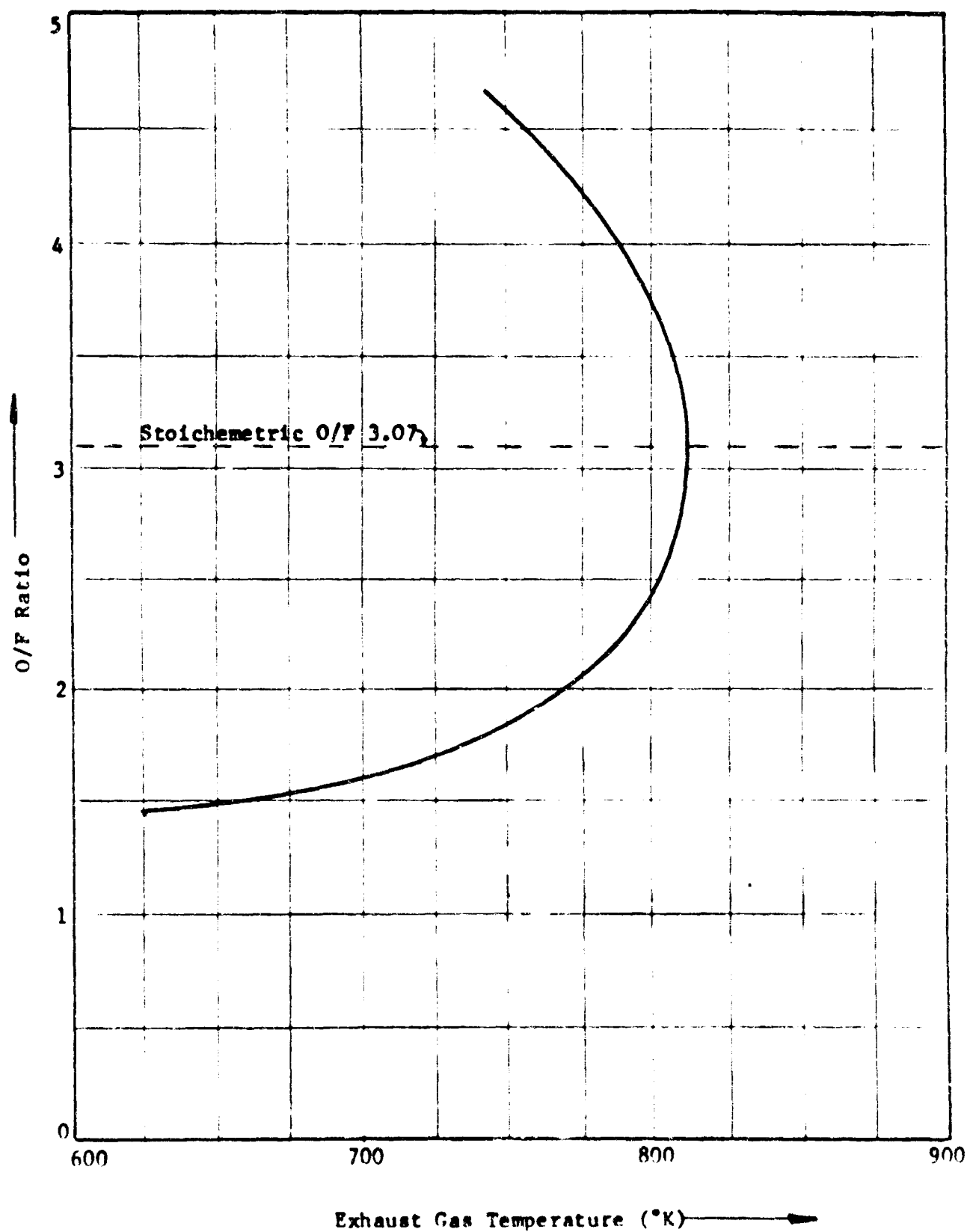


Figure 45. N_2O_4 - UDMH Exhaust Gas Temperature as a Function of Mixture Ratio for an Expansion Ratio of $\epsilon = 40$, $P_0 = 60$ psia

$$\dot{w}_e = \rho_e A_e U_e \quad (6.1)$$

where: ρ_e = exit density
 A_e = exit area
 U_e = exit velocity

and

$$\dot{w}_e = \dot{w}_o + \dot{w}_f = \dot{w}_p \quad (6.2)$$

For a given rocket engine and nozzle geometry A_e is fixed, and, therefore, a change in \dot{w}_p is reflected by corresponding changes in ρ_e and U_e .

Thus, it is certainly obvious that the mass flow rate \dot{w} is directly proportional to the nozzle exit mass density. In turn mass density ρ is proportional to the total number density (N) of the exhaust by a factor of Avogadro's number (N_A) and the average molecular weight of the exhaust gases (\bar{M}), i.e.;

$$N = \rho N_A / \bar{M} \quad (6.3)$$

Since we do not have a blackbody situation (the rocket exhaust is not a blackbody radiator), one must consider the individual specie number densities of all of the exhaust gas constituents, as these constituents all radiate at different wavelengths with different intensities. These specie number densities N_i can be determined as follows:

$$N_i = \rho_i N_A / \bar{M}_i \quad (6.4)$$

where ρ_i can be determined from the equation of state:

$$\rho_i = P_i \bar{M}_i / (\bar{R} T_e) \quad (6.5)$$

In the five equations above, \bar{R} is the universal gas constant, T_e is the equilibrium exhaust gas temperature, \bar{M}_i is the specie molecular weight, and P_i is the partial pressure of specie i . The latter is determined from Dalton's Law of partial pressures from the known species mole fractions. Therefore, it has been shown that changes in the flow rate \dot{w} , are proportional to changes in number density of the emitting exhaust gas constituents, which are in turn proportional to changes in radiant intensity emitted from the exhaust gas.

Having determined the effect of O/F ratio and \dot{w} changes on exhaust gas temperature and constituent number densities, one can then determine the overall effect of O/F and \dot{w} on radiant intensity based upon calculations such as those presented previously. Having done this, one is in a position to determine changes in O/F ratio by measuring or monitoring the radiation intensities of different (the most sensitive) emitting species, perhaps using the insensitive species as a reference.

C. MIXTURE RATIO VS FLOW RATE

The relationship between O/F ratio and flow rate for a rocket engine operating under constant combustion chamber and nozzle exit pressure conditions has been examined. This was done to demonstrate how simultaneous changes in O/F ratio and flow rate might produce constant pressure conditions in the chamber and exit station which might go undetected by pressure transducers and other types of pressure instrumentation. This phenomena could occur when O/F ratio goes off stoichiometric (such as an increase in \dot{w}_{ox}) thereby causing a decrease in combustion chamber temperature. However, since the flow rate has increased, the chamber pressure may remain constant as can be seen from the following equation:

$$P_c = C^*/(gA_t) \dot{w} = \frac{T_c^{1/2}}{\bar{M}} \dot{w} \quad (6.6)$$

for a given engine nozzle with throat area A_t .

The propellant combination chosen to demonstrate this effect was N_2O_4 /UDMH. The nozzle exit pressure P_e for these calculations was 2 psia. The O/F ratios considered were 2.5, 2.8 and 3.1. The chamber pressures considered were 10, 20 and 40 psia. The nozzle exit conditions produced by different O/F ratios (for a constant combustion chamber pressure) were calculated using an existing thermochemical computer program which yields as output data the values of T_e , \bar{M}_e , A_e/A_t and U_e . The flow rate corresponding to these engine operating parameters was calculated as follows:

$$\dot{w}_p = \dot{w}_e = \rho_e A_e U_e \quad (6.7)$$

where:

$$\rho_e = \frac{P_e}{RT_e} = \frac{P_e \bar{M}_e}{\bar{R} T_e} \quad (6.8)$$

or

$$\dot{w}_p = \frac{P_e \bar{M}_e U_e A_e}{\bar{R} T_e} \quad (6.9)$$

For any given throat area A_t :

$$\frac{\dot{w}_p}{A_t} = .76 \frac{P_e \bar{M}_e U_e}{\bar{R} T_e} (A_e/A_t) \quad (6.10)$$

where P_e is an atm \bar{M}_e in lb/lb mole, U_e in ft/sec, $\bar{R} = 1545$ ft lbf/lbm-°K, T_e is in °K and \dot{w}_p/A_t is in lbm/sec-ft².

Since the quantities on the right-hand side of equation (6.10) are all output quantities of the available computer program, the values for \dot{w}_p/A_t were calculated as a function of O/F ratio for constant P_c . (These flow rates could also have been calculated from the combustion chamber conditions

using the equation:

$$\dot{w}/A_c = g P_c (\bar{R}/T_c)^{1/2}. \quad (6.11)$$

The results of this calculation are given in Figures 46-48 for chamber pressures of 10, 20 and 40 psia. It can be seen from these figures that the relationship between O/F ratio and \dot{w} for a given rocket engine nozzle configuration and a given chamber pressure, is a linear one. Also, it is shown that the sensitivity of changes in O/F ratio to changes in flow rate, decreases as the chamber pressure is increased.

Thus it has been shown that it may be necessary to monitor conditions at the exhaust rather than in the combustion to determine changes in O/F ratio.

D. GAS TEMPERATURE MEASUREMENT

One method suggested for the attainment of rocket engine gas temperature is based on the ratio of two emission band intensities in the exhaust gases. This method is, therefore, independent of engine size, chamber pressure, area ratio, etc. Temperature information is obtained by means of the following expression:

$$\frac{I_1}{I_2} = \frac{P_1 v_1^4}{P_2 v_2^4} e^{(E_2 - E_1)/kT} \quad (6.12)$$

where:

I_1 and I_2 are the intensities of transition 1 and 2, respectively.

P_1 and P_2 are the respective transition probabilities (including the statistical weight factors).

v_1 and v_2 are the wave numbers.

E_1 and E_2 are the transition energies.

k is Boltzmann's constant.

T is the absolute temperature.

Relative intensity data for certain lines, e.g.: OH, CH, NH, C_2 , etc emission will be determined by the monitoring optical system; transition probabilities are known from wave mechanics tables of statistical weights, etc and wave numbers and transition energies are known to high accuracy from laboratory experiments over the last 50 years.

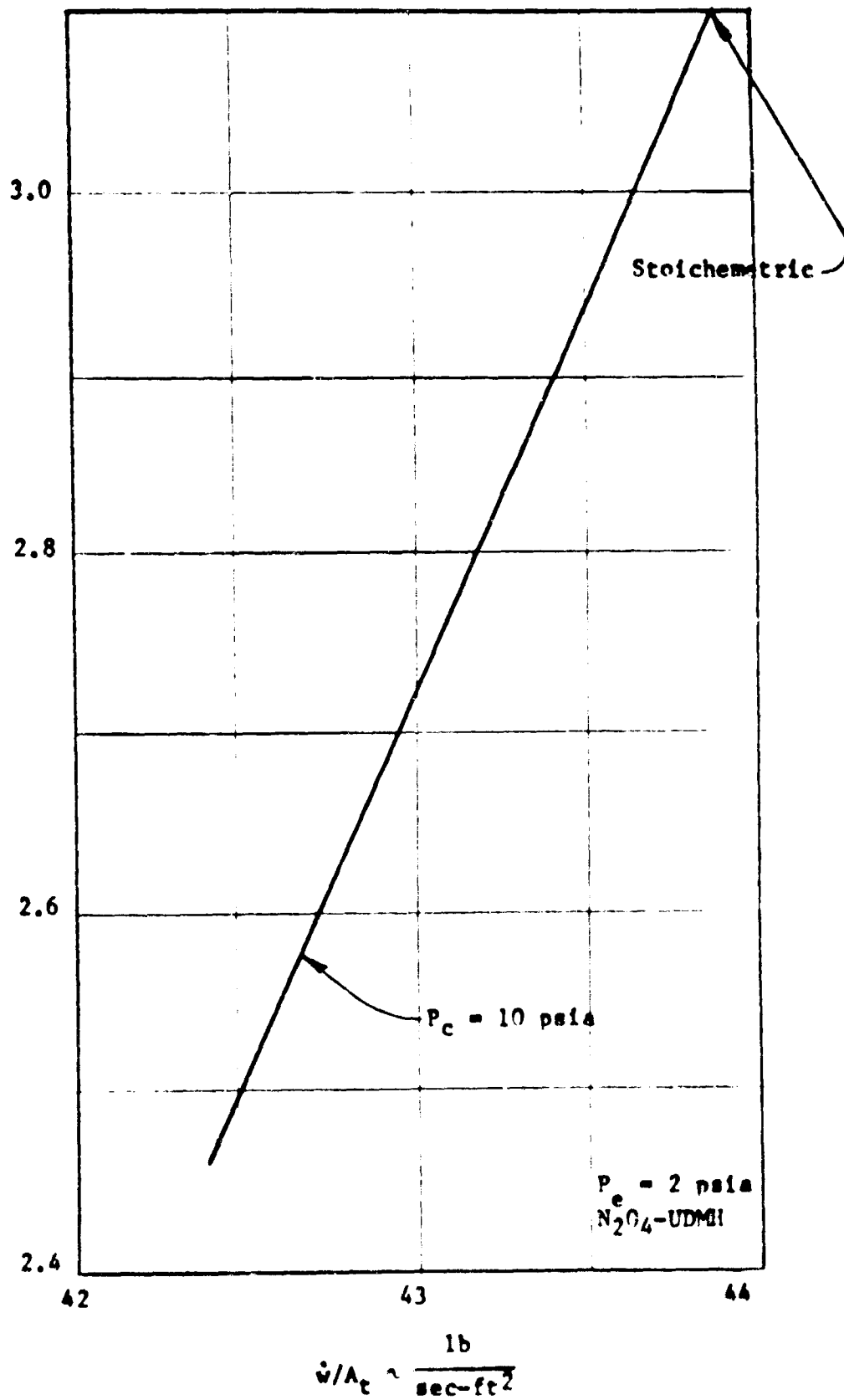


Figure 46. Mixture Ratio vs Flow Rate

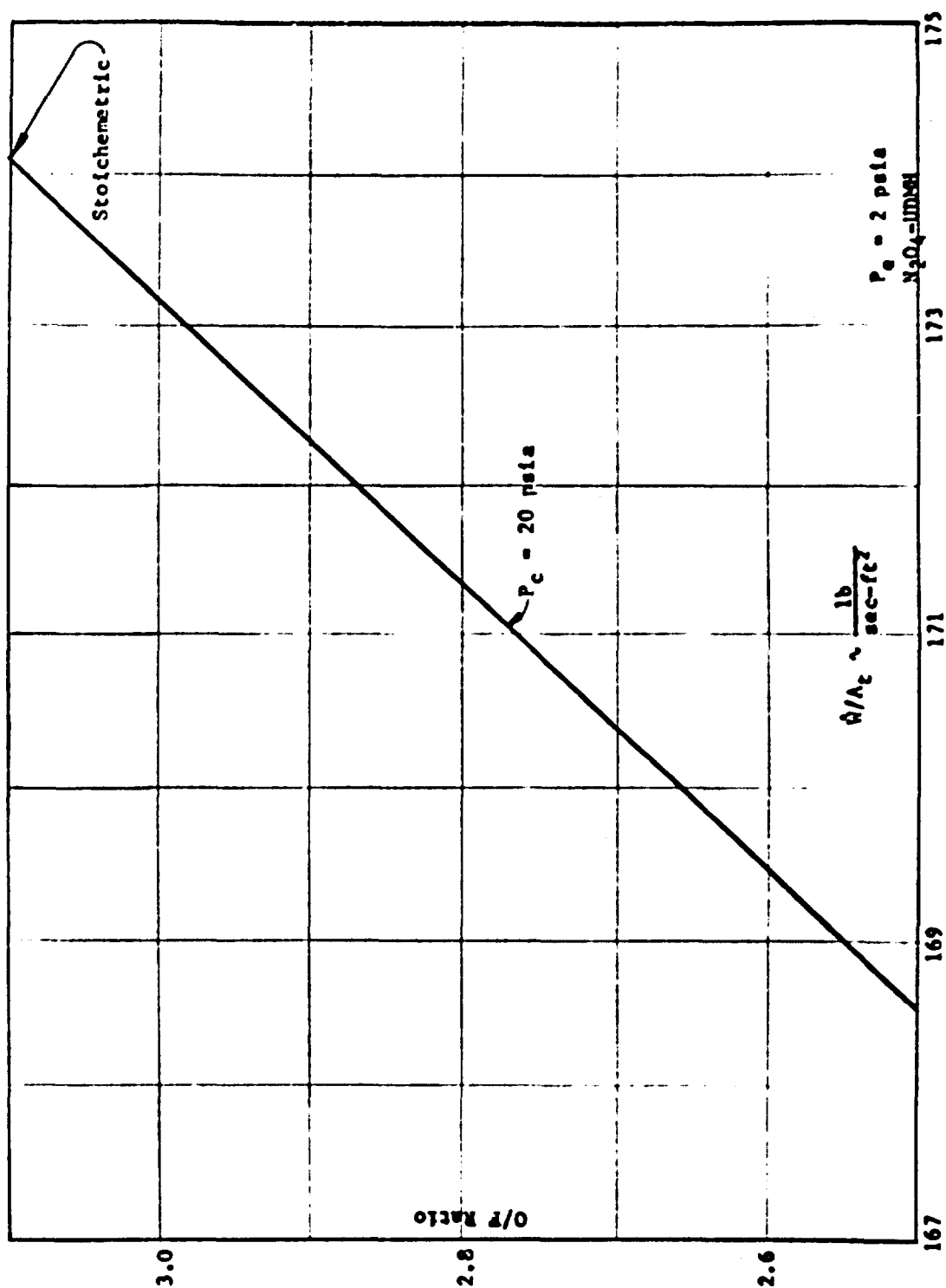


Figure 47. Mixture Ratio vs Flow Rate

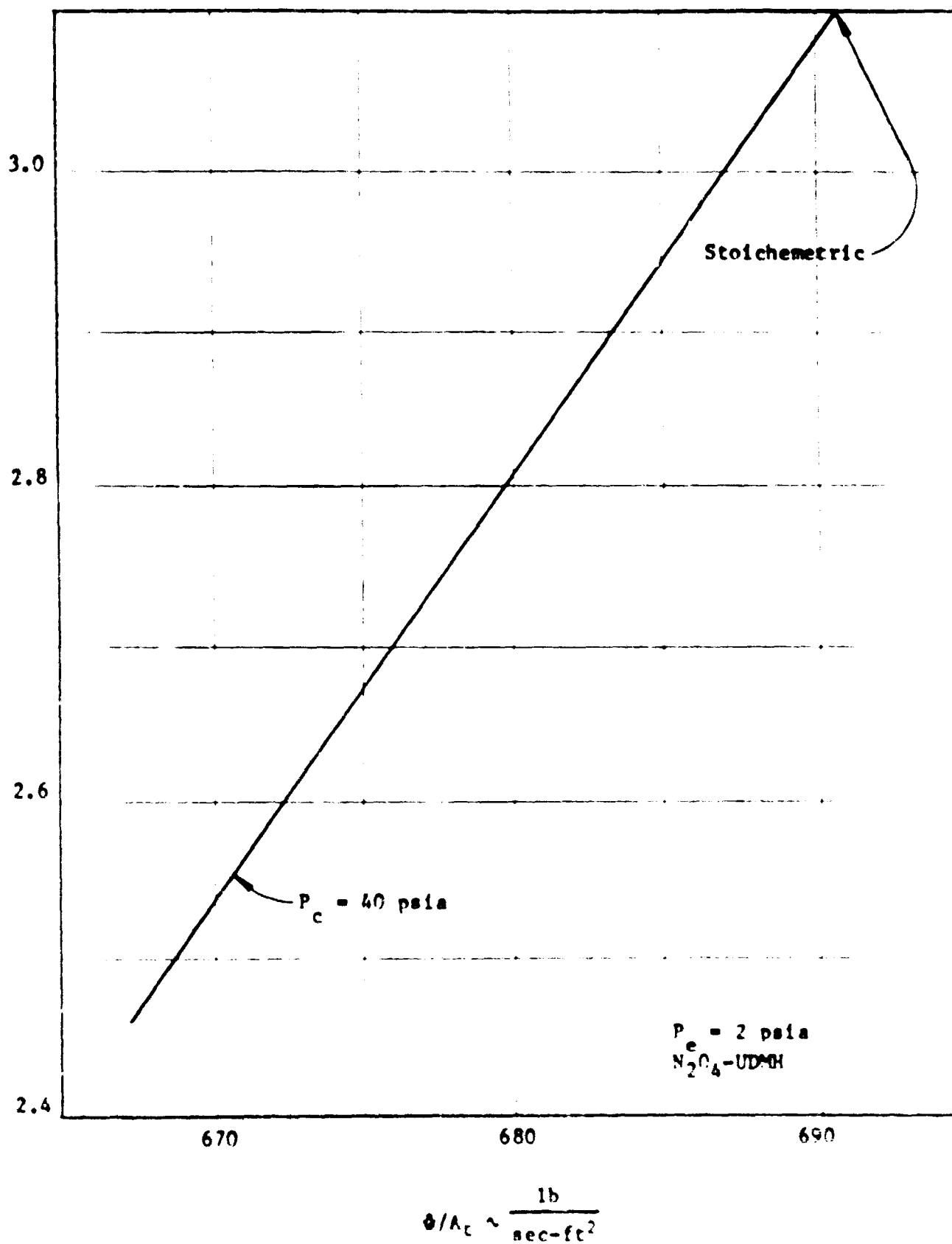


Figure 48. Mixture Ratio vs Flow Rate

SECTION 7

MALFUNCTION MONITORING

The previous sections on mixture ratio monitoring and exhaust gas temperature effects covered the various kinds of radiation changes which will occur due to upstream malfunctions in the propellant supply and feed systems. This section will, therefore, be confined to those malfunctions which can occur in the combustion chamber and exhaust nozzle; namely, combustion instability and chamber burnout.

A. COMBUSTION INSTABILITY

A considerable amount of open literature exists on the subject of rocket engine combustion instability (see for example Reference 12). In general, however, it can be said that instability is influenced by rocket engine chamber pressure, injector pressure drop, engine characteristic length, operating mixture ratio and length of propellant lines. Past studies have shown that two basic types of instability can occur: one at relatively high frequencies (screeching) and one at relatively low frequencies (chugging). The former type is generally associated with large engines¹³ and is primarily a function of engine geometry. It is characterized by the failure of exhaust temperature to follow fluctuations in combustion temperature. The latter type is more general in nature and is largely dependent upon the parameters previously noted. Our concern, therefore, will be with the chugging type of instability.

Assuming that the chemical processes in stable and chugging rocket flames are the same, the intensity of the electromagnetic radiators from such flames must be dependent upon flame pressure and temperature. Hence, any fluctuation in either the combustion or exhaust gas pressure and temperature should influence the corresponding radiation intensity. (Past theoretical and empirical studies support the relationship of temperature fluctuations in the chamber to corresponding fluctuations in the exhaust for chugging instability¹⁴). Fluctuations, however, can be caused by three generalized factors, viz: oscillations in the gas dynamic flow, turbulence in the expanding gases and afterburning of fuel-rich rocket exhaust products with ambient air. Both turbulence and afterburning are difficult phenomena to characterize, and the absence of literature on these subjects, especially with regard to radiation intensity variations, makes their analysis difficult. It is, therefore, preparable to study the influence of chugging oscillations in liquid propellant rockets arising from gas dynamic flow fluctuations only.

In order to eliminate considerations of turbulence and afterburning from model rocket engine studies, two conditions must be met, viz: tests must be conducted in a vacuum environment and nozzle size should be small enough to insure laminar flow. Turbulent flow in a rocket exhaust is characterized by mean particle velocities upon which is imposed a random fluctuating velocity. This latter component can be minimized by the attainment of nozzle design conditions which will insure a Reynolds number consistent with a laminar flow regime ($Re < 2000$)¹⁵. Figure 49 presents the relationship of rocket engine

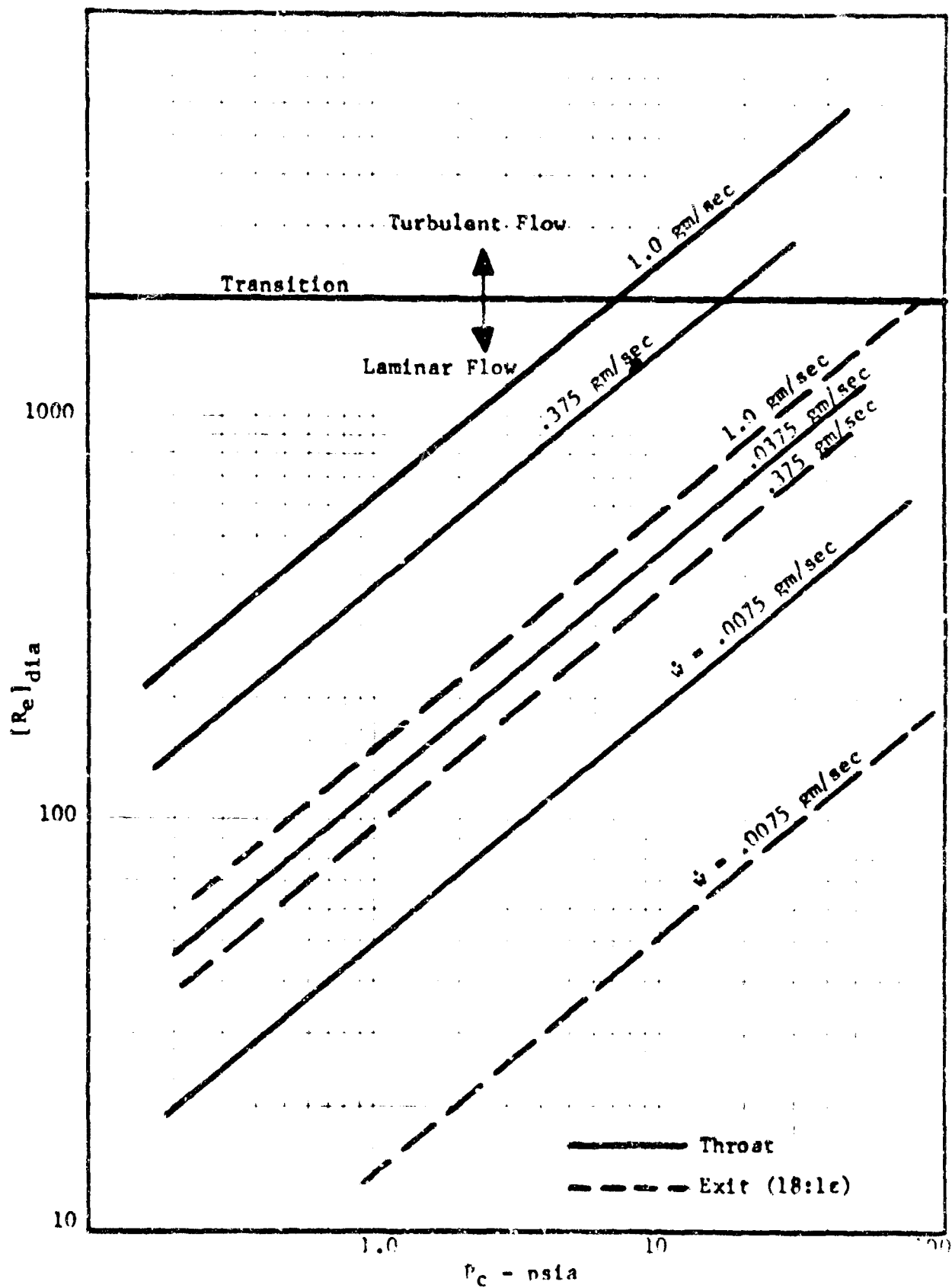


Figure 49. Rocket Engine Flow Rate and Chamber Pressure vs Nozzle Reynolds Number

flow rate and chamber pressure to Reynolds number for small systems. It can be seen that the engines previously recommended for testing ($\dot{m} \approx 0.1$ gm/sec and $P_c < 100$ psia) will provide flows within the laminar region. Testing at simulated high altitudes (vacuum), of course, insures the absence of afterburning, but in addition also serves to preserve the laminar flow pattern setup in the rocket nozzle.

Some experimental studies have been conducted with combustion devices to investigate the general area of radiation fluctuations as a function of chamber pressure variation. Of the more pertinent empirical work in this area, the most extensive is that reported by R. A. Goundry et al¹⁶. During the course of this program, experimental studies were conducted with a "tunnel" burner, spherical combustion vessel and small scale rocket motor. The former device is essentially a pulsed combustor which acts acoustically very much like an organ pipe. It was selected for test because of its simple construction, adaptability to alteration of fundamental vibration frequencies, inherently high combustion rates and high attainable acoustic noise levels. The combustion vessel which consists of an easily vented gas reaction sphere was selected to eliminate the variables of rocket engine design that could influence the instability mode.

The tunnel burner employed for these tests was 25 mm ID by 1.9 mm wall thickness, and the length relative to the gas entrance point was variable to permit alteration of resonance frequency. Combustion was attained by the ignition of air with ethylene or acetylene. Ultraviolet and visible radiation emissions were monitored by unfiltered photomultipliers of RCA Tynes 1P21 and 1P28 through slits which limited the detector field of view. The PM tube signal was fed to an AC voltmeter which indicated average power of the radiation modulation and to a Tektronix scope which provided signal level, percent modulation and wave form. Infrared radiation was monitored by a PbS detector in a similar manner. All tests were conducted under sea level standard temperature-pressure conditions (SLSTP).

Results showed that the UV, visible and IR signals were essentially the same indicating a DC component with as much as 50 percent AC modulation. The wave form picture presented a regular series of pulses equivalent to the resonant operating frequency of the tube. Scans taken downstream of the nozzle in the UV showed maximum intensity at a point approximately 2-1/2 inches from the tube exit plane with some afterburning emission starting 10 inches downstream. The latter emission was, as expected, strongly dependent on mixture ratio. The intensity measured in the UV for afterburning was about one order of magnitude less than that obtained near the exit which result is in line with the lower energy state of this reaction. Comparable infrared measurements may have shown a higher relative intensity level.

The pressure vessel consisted of a heavy walled four liter sphere with a fast acting valve. A combustible mixture of oxygen and ethylene was introduced into the vessel, isolated, sparked and expanded through a nozzle. All tests were again conducted at SLSTP conditions. Supersonic flow was attained in the jet as evidenced by a shock zone 1 to 2 cm downstream of the nozzle exit plane. Afterburning on the average was visible commencing 15 cm downstream and for a total distance of 10 cm although the incidence of

afterburning was dependent on the jet temperature. A pressure transducer was used to measure vessel pressure and emission of the flame in the UV. Visible and IR was observed by a 1P28 PM tube and a PbS detector both of which were permitted to view the entire flame over their full range of sensitivity. Acoustic measurements were made with a condenser microphone. A dual beam scope equipped with a 35 mm camera was employed to record radiation and acoustic signals.

Results indicated marked dependency of radiation intensity on afterburning and no correlation between vessel pressure and radiation signal modulation. The modulation frequency of the UV radiation with afterburning was found to be about 700 cps; without afterburning a higher frequency component (about 2000 cps) was noted. No conclusions were drawn from this work.

The rocket motor tests were conducted with an air/ethylene system of approximately 3 lbs thrust exhausting into air at SLSTP conditions. Measurements were again made in the UV, visible and IR spectral regions in conjunction with chamber pressure and acoustic pressure fluctuation measurements. The data was stored on magnetic tape, transferred to oscillographic recordings and also fed to a power spectrum analyzer.

The results of these tests were generally inconsistent especially concerning plume radiation. IR detectors viewing the interior of the combustion chamber through an optical window were able to follow P_c , T_c fluctuations without difficulty. However, in the exit plane the IR and UV results were not comparable and only the IR showed intermittent correlation with the chamber pressure fluctuations. In general the IR fluctuations were more rapid at the exit plane than for the plume in its entirety. Regarding the UV however, it should be noted that different PM tubes viewing the same event did provide signals of similar characteristics thereby increasing the reliability of that portion of the spectral data.

In retrospect it can be said that given the well tested premise that T_c follows T_c in chugging combustion, the radiation pattern in the exhaust jet must reflect this modulation unless acted upon by other forces which tend to dampen or diminish this correspondence. Such factors were of course present in the previously discussed tests, and seem, without exception, to be chargeable with the failure of these tests to produce the desired correspondence. This is not to say, however, that afterburning and turbulence were unequivocally that cause, but nothing in the results can dispute this premise. It therefore follows that tests under space conditions should provide more meaningful results.

The best type of rocket engine one could employ to study the phenomena of chugging combustion is a gas/gas system which operates within a fairly narrow combustible zone. It is known from past work on engines of this type at this corporation, that operation on the fringe of the combustible zone will give rise to chugging instability, and that this type of chugging is controllable to some degree as regards frequency by vernier adjustment of the mixture ratio. The optimum propellant system has been found to be an air/hydrocarbon gas (for example: propane). By injecting the air longi-

radially into the chamber and the fuel tangentially, good mixing is assured; and in addition, the fuel serves to provide a cooling thermal layer between the combustion core and the chamber inner wall as shown in Figure 50. Hence, the combustion chamber can be constructed of a relatively soft metal such as 6061 aluminum. Ignition would be effected by a spark plug.

B. CHAMBER BURNOUT

The erosive burning of metal parts of the combustion chamber or nozzle will introduce new molecular species into the exhaust plume. These species will consist primarily of the oxides of various metals all of which generally radiate strongly in the visible region of the spectrum when acting as discrete emitters rather than at those regions of interest for mixture ratio monitoring. Typical band spectra wavelengths for discretely emitting metallic oxides of chamber and nozzle structural materials are shown in Table 18. Band emission spectra can be expected to arise in combustion flames when the concentration of such impurities is very low, and should, therefore, serve to indicate the initial incidence of failure. As the burnout progresses however, the flame will tend to take on an incandescent character causing it to act like a black-body.

In the latter case the radiation that can be expected from a luminous flame depends upon several factors regarding the nature of the incandescent particles suspended therein, including: their concentration, unit size, radiative properties and absorptive properties. The emission characteristics of the luminous flames can be closely determined from the procedure outlined in Reference 17, but it is anticipated that malfunction based on blackbody considerations will not be useful in preventing extensive upstream damage. If the flame has already taken on a luminous character, it can be assumed that burnout has progressed to destructive proportions. Hence, detection should be based upon the ability to identify the discretely emitting oxide bands.

The oxide bands of interest in this study could exist at relatively low levels even during normal engine operation since a certain amount of erosive burning may always occur in particular rocket engine configurations. This is probably more noticeable in a radiation cooled engine than in a regeneratively cooled engine, and, of course, is certainly true in an ablative engine. In fact the ablative type may have to be monitored by total emission considerations rather than the discrete banded emission characteristics.

In either of the above cases a minimum level of emission indicative of allowable erosion can be established empirically and applied practically through the use of minimum band-pass-minimum intensity filters. Such selective filters can be chosen to isolate particular high intensity bands characteristic of certain metallic oxides depending upon the construction material used. Where the nozzle and chamber are of different materials, sequential filtering will distinguish nozzle erosion from chamber erosion. The radiation changes during the initiation of a destructive erosion of the chamber or nozzle should be sufficiently large compared to normal operation that gross quantitative measurement will be more than adequate to distinguish

TABLE 18

TYPICAL BAND SPECTRA OF REACTED ROCKET COMBUSTION
CHAMBER STRUCTURAL CONSTITUENTS

| Element | Oxidation Product | Emission Wavelengths (\AA) |
|--|-------------------|--|
| Base Metals | | |
| Copper | CuO | 4453-4917, 5228-5350, 5828-6547 |
| Iron | FeO | 5290-6651, 4386-4929, 6700-9408 |
| Nickel | NiO | 5174, 6133, 7330, 7900 |
| | NiH | 4207, 5713, 6257, 6442 |
| Titanium | TiO | 4462-6215, 5598-5694, 62.5-7949 |
| Tungsten | WO | 4110-5396 |
| Alloys | | |
| Chromium | CrO | 5168-6892 |
| | CrH | 3675 |
| Molybdenum | MoO | 7000-9000 |
| Niobium | NbO | 4511, 4689, 4915, 5470-6270 |
| Vanadium | VO | 5469-6533 |
| Refractories | | |
| Beryllium Oxide | BeO | 4180-5476, 6118-11235 |
| Silicon Oxide (SiO ₂) | SiO | 2177-2925 |
| Zirconium Oxide (ZrO ₂) | ZrO | 2940-3052, 3390-3981, 4470-4850, 5456-6070, 5439-6996 |

the abnormal condition. The cumulative, normal, unlocalized erosion over an extended time could also conceivably be measured by integrating the intensity-time relationship. Sophisticated electronic systems for this purpose have been developed for inertial guidance of missiles and submarines in which the integration of acceleration-time is monitored with extreme accuracy.

There would appear to be no advantage in the use of signal coatings. However, where coatings are applied to the chamber for thermal protection, the appearance of base metal oxides in the exhaust flame would be an indication of a more severe condition than metal erosion in the uncoated situation. These effects would be very dependent on the kinds of coatings, their thickness, the amount of normal microcracking, etc, and would have to be evaluated for each specific case. A spectroradiometer system designed by Block Associates appears to be very suitable for the purpose of monitoring malfunctions. In this unit four filters and a calibration source are sequentially inserted in front of the detector with a 0.9 second cycle. The design, intended for space operation in the original concept, is lightweight and compact, shock and vibration resistant.

The same system that monitors chamber and nozzle erosion could also identify propellant contamination due to storage corrosion. If the tankage is of a sufficiently different material from that of the chamber and nozzle, one of the four filters could be used to isolate the characteristic radiation of this item. If the materials are essentially the same, propellant contamination should still be distinguishable since it will be a gradual cumulative phenomena compared to the more sudden occurrence of chamber and nozzle erosion. Again these effects must of course be considered relative to the normal operating conditions since there may always be some contribution to the radiation from propellant impurities.

SECTION 8

FLIGHT SYSTEM ANALYSIS

To achieve minimum weight and size as well as high reliability, a flight version performance monitoring system should not require a scanning spectrophotometer. Instead a simple light collimating system viewing a preselected region of the rocket plume would transmit the collected radiation by means of suitable lenses and mirrors to photodetectors whose wavelengths sensitivities (as determined by the nature of the photosensitive surface and interposed filters) would be restricted to the specific spectral regions of interest.

As discussed elsewhere in this report, the emission of various bands and/or the ratio of the intensities of various emission bands are smooth single valued functions of mixture ratio, the particular bands of interest being determined by the propellant system. The use of intensity ratios has two distinct advantages: first, the sensitivity can be magnified since one of the two selected wavelengths may increase while the other decreases with changing mixture ratio; secondly, overall changes in absolute intensity or instrumental sensitivity which may effect all wavelengths will be substantially cancelled.

Another method having somewhat similar advantages is the measurement of the energy difference between two selected radiation bands. This method is particularly attractive since direct measuring differential phototubes such as the No. 5652 have been developed¹⁰. This type of phototube differs from conventional types in that it has two photosensitive plates within a single envelope as illustrated in Figure 51. Both plates emit electrons when irradiated but either plate may act as anode or cathode depending on the relative energy incident on the plates.

When an illumination differential exists between the plates of a differential phototube, the emitted electrons create differing space charge densities which cause DC current to flow between the two plates when they are connected by a bias resistor. The polarity and magnitude of this current is a function of the radiant energy differential. A phototube of this type can, therefore, serve the purpose of two conventional phototubes with the added advantage of requiring only a single load resistor. This will increase the reliability of the system by reducing the number of components, particularly the high-value load resistors which may be subject to changing characteristics on aging.

The use of selective filtering with a differential phototube is illustrated in Figure 52. The choice of the two filters gives a combined spectral response characteristic in two separate wavelength regions. In using such characteristics for mixture ratio monitoring, the output voltage across the load resistance would be nulled out in the recording instrument so that a zero voltage is seen for the design operating conditions, and readings of plus or minus voltage would measure the off-design excursion. This type of readout would be particularly suited to automatic control of the mixture

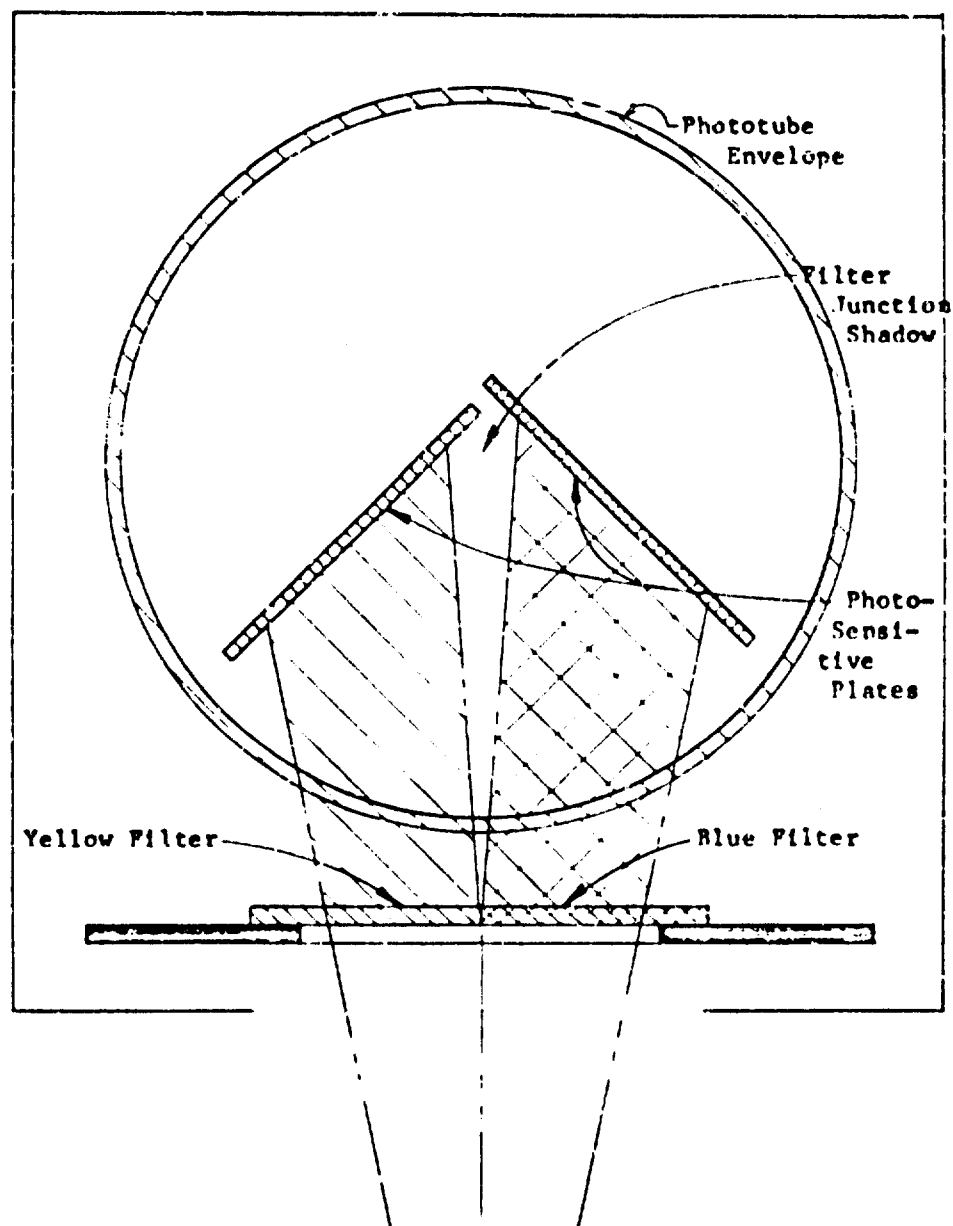


Figure 51. Schematic Arrangement of a No. 5652 Phototube and Selective Filters

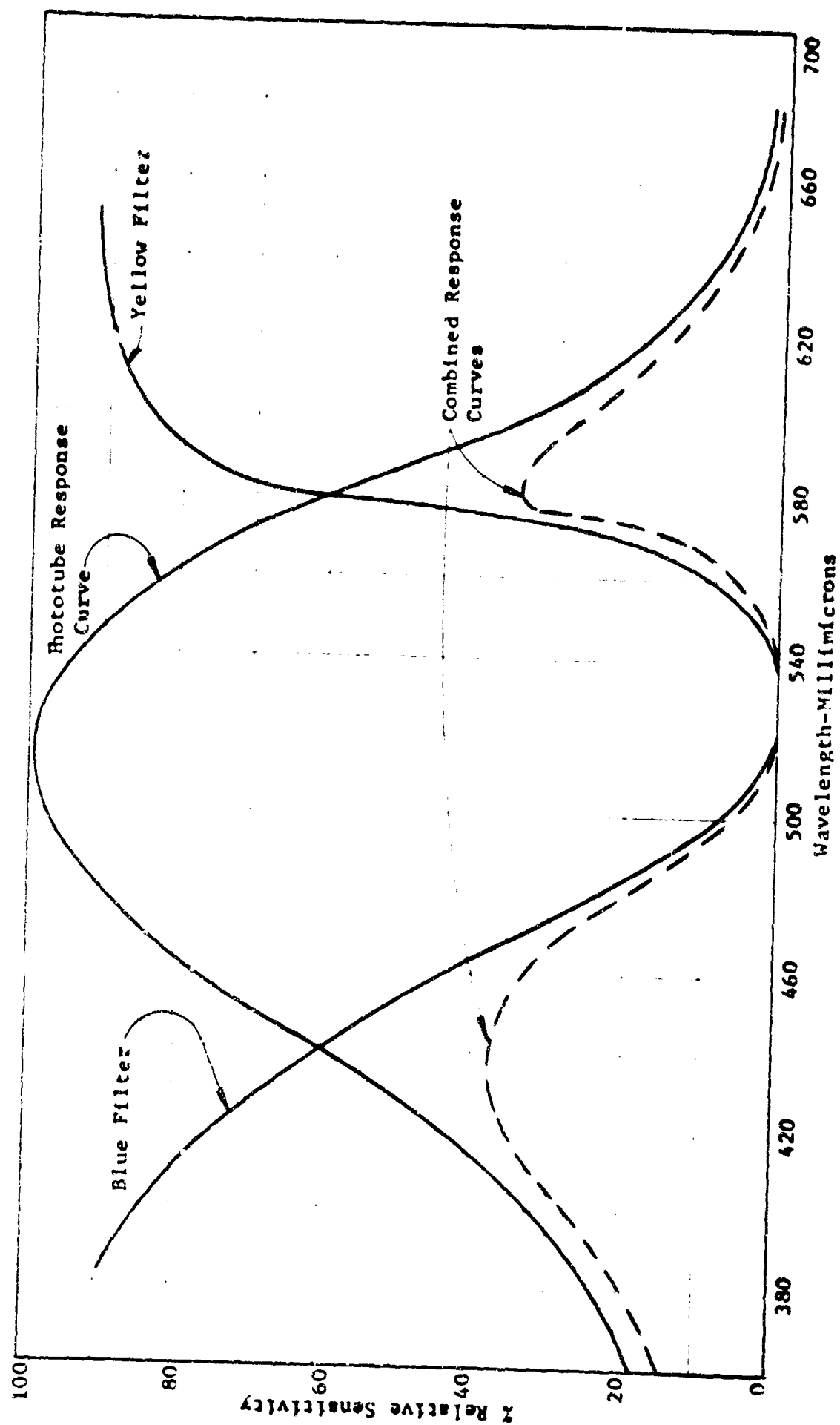


Figure 52. Typical Response of Phototube Cathodes and Selective Filters

ratio with servo-driven flow controllers.

Many varieties of readout instruments have been developed for missile and space applications. A particularly attractive electrometer has been developed recently by the Applied Physics Laboratory under a NASA contract¹⁹. This instrument was redesigned from a laboratory type unit as an off-the-shelf low current measuring device for general purpose use in satellite experiments. The instrument weighs 2.4 pounds, has a volume of 36 cubic inches and requires one watt of power. Its detection sensitivity of 10^{-17} amperes with an accuracy of $\pm 1\%$ is adequate for measuring the anticipated output of phototubes measuring rocket plume emissions. A particular design feature is temperature compensation and stability over long duration satellite missions.

The present extensive interest in solid state materials, lasers, masers, photoconductance and radiation measurements has provided an almost unlimited variety of photosensitive materials, phototubes, crystalline optics and filters covering a wide electromagnetic spectrum. All these devices are relatively small and lightweight. Even the more complex detectors requiring cooling for increased signal-to-noise efficiency might be considered in those situations where cryogenic propellants are on board the vehicle or the detector could be emersed in space-cold temperatures.

SECTION 9

CONCLUSIONS AND RECOMMENDATIONS

As a result of this study conducted to determine the feasibility of detecting emission spectra in the exhaust stream of a rocket engine as a measure of various propulsion system characteristics, the following conclusions can be stated:

- A. It appears feasible to detect small changes in mixture ratio and propellants flow rate by changes in plume emission and to detect the onset of combustion chamber malfunction (burnout or instability).
- B. The propellants selected for theoretical analysis were LO_2/LH_2 , $\text{LO}_2/\text{RP-1}$ and $\text{N}_2\text{O}_4/\text{UDMH}$ as being most representative of current and near-future liquid propellant flight systems.
- C. Representative plume intensity calculations showed that the species of interest could be readily detected by available laboratory instruments (UV, visible and IR).
- D. A rocket engine of flow rate 0.1 gm/sec and chamber pressure 50-100 psia was found to be compatible with both the available vacuum test facility, and current instrumentation capabilities.
- E. The species showing the greatest variation intensity as a function of mixture ratio were CH, CHO and CN; NO and OH were also of interest because of their positive slope characteristics as opposed to the preceding.
- F. In examining the problem of total flow rate changes, it was determined that intensity is a direct linear function of flow rate (for constant O/F) while mixture ratio is generally nonlinear. These effects can, therefore, be separated. Hence, mixture ratio and flow rate can be measured by this technique.
- G. Combustion instability may be detected by frequency monitoring of fluctuations in exhaust gas radiation intensity when observed under conditions of simulated high altitude.
- H. It appears to be feasible to monitor incipient burnout by detecting the intensity of characteristic metal oxides in the exhaust stream and to detect contamination by monitoring the emission of certain impurities if known to exist to some degree in the propellants.
- I. Flight systems can probably be developed from currently available components which will assure lightweight and small size. Complex dual-signal phototubes are now available for direct signal comparison if this approach is found to be advisable.

Based on the above conclusions, it is recommended that:

1. An experimental program be conducted with an engine of the size noted above using N_2O_4 /UDMH propellants. These propellants are recommended since they are most representative of space engines and produce all of the significant species occurring in the three propellant systems studied.
2. The species of major interest in the recommended test program should be: OH, CH, CHO and CN (UV); C_2 (visible) and H_2O , CO_2 (IR). One or more of the above occur in each of the three propellant combinations studied and their mole fractions vary with mixture ratio in a similar manner in all cases.
3. It is recommended that tests be conducted to determine experimentally the variation of each of the above species with mixture ratio (at constant flow) and with total flow rate (at constant mixture ratio).
4. Since a number of bands are recommended for study (seven), laboratory instrumentation (spectrometers capable of scanning a large segment of the optical spectrum) should be employed rather than discrete measuring devices, e.g.: filter phototubes.
5. It is recommended that tests designed to study combustion instability, incipient burnout and propellant impurities be conducted with a gas/gas engine of simple construction to simplify the conduct of such tests.
6. Based on the above test results, it is recommended that a "breadboard" detector of discrete capability be designed for prototype future tests.

REFERENCES

1. "Research Study to Determine Propulsion Requirements and Systems for Space Missions" Rpt. No. 2150, Aerojet General Corp., December 1961.
2. "Study of High Effective Area Ratio Nozzles for Spacecraft Engines" Rpt. No. NAS 7-136-01F, Aerojet General Corp., 16 September 1963.
3. "Surveyor Vernier Propulsion System" Design Review No. 4, Thiokol Chemical Corp., Reaction Motors Division, May 1963.
4. "Maneuvering Satellite Propulsion System Demonstration" SSD-TDR-62-206, December 1962.
5. Bray, K. N. C. and Appleton, J. P., "Atomic Recombination in Nozzles: Methods of Analysis for Flows with Complicated Chemistry", C. P. No. 636, Ministry of Aviation, Aeronautical Research Council 1963.
6. Bray, K. N. C., "A Simplified Sudden-Freezing Analysis for Non-Equilibrium Nozzle Flows", A.A.S.U. Report No. 161, 1960, A.R.C. 22 825.
7. Vick, A. R., "Results of Theoretical Studies Made at the Internal Aerodynamics Branch in Connection with Surveyor Exhaust Effects Program", NASA Langley Internal Document dated 7 November 1962.
8. Thomson, A. J., "Radiation Model for the Solid Carbon Emission from Missile Plume at Altitudes Below 50KM" (U), GD/Ascro Paper E-7, Eleventh National IRIS Symposium, June 1964.
9. Parkass, I., "Ultrahigh Vacuum Design for Large Simulation Systems", IES Publication.
10. Honig, R. E. and Hook, H. O., "Vapor Pressure Data for Some Common Gases", RCA Review, XXI, No. 3, 1960, pp 360-368.
11. Honig, R. E., "Vapor Pressure Data for the Solid and Liquid Elements", RCA Review, XXIII, No. 4, 1962, pp 567-586.
12. Ducarne, J., Gerstein M. and Lef-bvre, A., "Progress in Combustion Science and Technology, Volume I", Pergamon Press, 1960.

REFERENCES (continued)

13. Barrere, M. et al, "Rocket Propulsion", Elsevier Publishing Co., Amsterdam, 1960.
14. Crocco, L. and Cheng, S. I., "Theory of Combustion Instability in Liquid Propellant Rocket Motors", Agardograph No. 8 Butterworth Scientific Publications, London, 1956.
15. Lehrer, S. and Thatcher, A., "The Rocket Engine as a Research Tool", Proceedings of the LPIA Meeting, Astrosystems, November, 1962.
16. Goundry, R. A. et al, "Investigation of Radiation Emitted from Flames", Final Report, Contract AF 19(604)-7337, Thiokol Chemical Corp.
17. Yagi, S. and Iino, H, "Radiation from Soot Particles in Luminous Flames", Eighth Symposium on Combustion, August 28-September 3, 1960.
18. Haehner, C. B., "Electro-Optical Color Selection", Western Electric Engineer, Vol. VIII, No. 2.
19. Missiles & Rockets Magazine, "Versatile Vibrating-Reed Electrometer Delivered to NASA", September 14, 1964.

BIBLIOGRAPHY

1. G. Herzberg, "Spectra of Diatomic Molecules", 2nd Ed., VanNostrand, New York, 1950.
2. G. Herzberg, "Infrared and Raman Spectra", VanNostrand, New York, 1945.
3. S. S. Penner, "Quantitative Molecular Spectroscopy and Gas Emissivities", Addison-Wesley Pub. Co., Massachusetts, 1959.
4. W. S. Benedict and E. K. Plyler, "Energy Transfer in Hot Gases", N.B.S. Circular 523, 1954.
5. B. J. McBride et al, "Thermodynamic Properties to 6000°K for 210 Substances Involving the First 18 Elements", NASA SP-3001, 1963.
6. A. G. Gaydon and H. G. Wolfhard, "Flames", 2nd Ed., Chapman and Hall Ltd., London, 1960.
7. A. G. Gaydon, "Dissociation Energies and Spectra of Diatomic Molecules", 2nd Ed., Chapman and Hall Ltd., London, 1953.
8. Pearse, R. and Gaydon, A., "The Identification of Molecular Spectra", Chapman and Hall Ltd., 2nd Ed., 1950.
9. Rosen, B., "Données Spectroscopiques Concernant les Molecules Diatomiques", Hermann and Co., 1951.
10. Bates, D. R., Ed., "Atomic and Molecular Spectra", Academic Press, New York, 1962.
11. White, H. E., "Introduction to Atomic Spectra", McGraw Hill Book Pub. Co., New York, 1934.
12. Chandrasekhar, S., "Radiation Transfer", Dover, 1960.
13. Chandrasekhar, S., "Stellar Structure", Dover, 1960.

BIBLIOGRAPHY (continued)

14. Gaydon, A. G., "The Spectroscopy of Flames", Chapman and Hall, London, 1957.
15. R. W. Nicholls, P. A. Fraser and W. R. Jarman, Combustion and Flame, 3, 13, 1959.
16. W. M. Vaidya, Proceedings of the Royal Society of London, 147, 513, 1934.
17. S. S. Penner, Journal of the Optical Society of America, 50, 627, 1960.
18. D. M. Dennison, Reviews of Modern Physics, 12, 175, 1940.
19. C. W. Allen, "Astrophysical Quantities", 2nd Ed., University of London, The Athlone Press, 1963.
20. W. R. Jarman, P. A. Fraser and R. W. Nicholls, Astrophysics Journal, 118, 228, 1953, 131, 399, 1960, 122, 55, 1955.
21. Gaydon, A. G., Proceedings of the Royal Society of London, 179, 439 (1942).
22. Vaidya, W. M., Proceedings of the Physical Society, A64, 428 (1951).
23. Murphy and Schoen, Journal of Chemical Physics, 19, 1214, (1951).
24. Fraser, P. A., Canadian Journal of Physics, 32, 575, 1954.
25. Marr, G. V., Canadian Journal of Physics, 35, 1265, 1957.
26. Turner, R. G. and Nicholls, R. W., Canadian Journal of Physics, 32, 460, 1954.
27. Carrington, T., Journal of Chemical Physics, 31, 1243, 1959.

BIBLIOGRAPHY (continued)

28. Kelley, K. K., U. S. Bureau of Mines Bulletin #383 (1935).
29. Woolley, H. W., Scott, R. B., Brickwedde, R. G., J. Research NBS 41, 277 (1948) RP 1932.
30. D. W. Eastman and L. P. Radtke, A.I.A.A. Journal, Vol. 1, No. 4, April 1963.
31. E. S. Love et al, NASA, TR R-6, 1959.
32. T. C. Adamson, Jr. and J. A. Nicholls, J. of the Aero/Space Sciences, Vol. 26, No. 1, January 1959.
33. L. J. Wang and J. B. Peterson, Jet Propulsion, May 1958.
34. D. W. Eastman and L. P. Radtke, Boeing Rpt. D2 10599, December 1962.
35. T. C. Adamson, Jr., University of Michigan, Rpt. 4613-45-T, June 1963.

APPENDIX A
SAMPLE CALCULATION FROM THERMOCHEMICAL PROGRAM

PROPELLANT PERFORMANCE REPORT

DATE: 8-4-67

THIokol CHEMICAL CORPORATION

PAGE 1 OF 2

FILE: HMM

REACTION MOTORS DIVISION

SAS NO.

INGREDIENTS INFORMATION

PROJ. NO. 82005

| NAME OR SYMBOL | EMPIRICAL FORMULA | FEED T DEG. K | DENS. G/CC | MOL. WT. G/MOLE | DELTA H/F KCAL/MOLE |
|----------------|-------------------|---------------|------------|-----------------|---------------------|
| HMM | C2.H8.N2. | (L) 298.15 | 0.784 | 60.102 | 12.700 |
| N2O4 | N2.O4. | (L) 294.30 | 1.448 | 92.016 | -6.800 |

COMPOSITION WEIGHTS GRAMS

| | | | |
|------|--------|--------|--------|
| H/F | 1.500 | 1.500 | 1.500 |
| HMM | 40.000 | 40.000 | 40.000 |
| N2O4 | 60.000 | 60.000 | 60.000 |

ELEMENTS IN PROPELLANT, GRAM ATOM PROPELLANT, GRAM A PROPELLANT, GRAM A

| | | | |
|---|---------|---------|---------|
| C | 1.33107 | 1.33107 | 1.33107 |
| H | 5.32428 | 5.32428 | 5.32428 |
| N | 2.63519 | 2.63519 | 2.63519 |
| O | 2.60824 | 2.60824 | 2.60824 |

THERMAL DATA AND PERFORMANCE PAR AND PERFORMANCE R AND PERFORMANCE I

| | | | | | | |
|----------------|---------|-------------------|---------|-------------------|---------|-------------------|
| (UP) C EQUIL. | 13.37 | 13.37 | 13.37 | | | |
| GAMMA PAR | 1.305 | 1.300 | 1.302 | | | |
| ENTROPY | 3.209 | 3.209 | 3.209 | | | |
| CP, PAR | 1.704 | 1.775 | 1.784 | | | |
| AR/AT | 37.10 | 25.08 | 30.42 | | | |
| CP, IDEAL | 1.741 | 1.710 | 1.724 | | | |
| PHI/DIL K | 1.082 | 1.082 | 1.082 | | | |
| CO, TH | 5405.0 | 5405.0 | 5405.0 | | | |
| ISP, IDEAL | 292.42 | 287.21 | 289.54 | | | |
| ISP, PHO/R | 316.28 | 310.65 | 313.16 | | | |
| ISP, SPACE | 311.79 | 298.13 | 299.76 | | | |
| EQUIL. TEMPER. | | | | | | |
| | CHAMBER | FROZEN EXHAUST | CHAMBER | FROZEN EXHAUST | CHAMBER | FROZEN EXHAUST |
| PRES., PSIA | 40.00 | 0.00 | 40.00 | 0.15 | 40.00 | 0.12 |
| PRES., ATM | 4.083 | 0.006 | 4.083 | 1.010 | 4.083 | 0.008 |
| TEMP., K | 2457.2 | 591.0 | 2457.2 | 677.0 | 2457.2 | 630.2 |
| TEMP., F | 4323.3 | 609.7 | 4323.3 | 758.9 | 4323.3 | 691.0 |
| MOLE WT | 18.683 | 18.683 | 18.683 | 18.683 | 18.683 | 18.683 |

PROPELLANT PERFORMANCE REPORT

DATE: 11-4-67
FILE: 0044

THIOMIL CHEMICAL CORPORATION
REACTION MOTORS DIVISION

PAGE 2 OF 2
SAS NO.

PRODUCT COMPOSITIONS

PROJ. NO. 82005

| | CHAMBER | EXHAUST |
|------|---------|---------|
| C O | 0.22206 | 0.22296 |
| C O2 | 0.02572 | 0.02572 |
| H | 0.01277 | 0.01277 |
| C H | 0.00240 | 0.00240 |
| H2 | 0.27057 | 0.27057 |
| N O | 0.00018 | 0.00018 |
| N2 | 0.24618 | 0.24618 |
| O | 0.00017 | 0.00017 |
| H2O | 0.21020 | 0.21020 |

APPENDIX B
COMPUTER PROGRAMS FOR UV AND IR RADIANCE CALCULATIONS

OPERATION.001 0A-OCT-1964 17142147 ROU1.001 GATE 999 999

ASTROSYSTEMS PLUME SPECIES RADIANCE INFERRED M

10 IS HIGHEST STATEMENT NUMBER

200 ABCONS

DIMENSION C(4)D(560)X(20)I(3)J(100)K(20)G(4)H(160)

1 READ

X1 = 2.60.19 * C2 * 273.15 / C1

G4 = G2 / C1

2,11,1,1,4,

H11 = C3

3,11,1,1,6,

H(11+4) = G4

4,11,5,1,7,

H(11+2 * 1) = C11

H(11+2 * 2) = C11

5,11,1,1,16,

GO TO 5 IF H11 = 0

H(11+20) = X1 * H11

H(11+40) = EXP.(-D(11+40) * G4)

H(11+60) = EXP.(-D(11+60) * G4)

H(11+80) = -4 IF D(11+80) = 0

H(11+80) = EXP.(-D(11+80) * G4)

H(11+80) = -4 IF D(11+80) = 0

X2 = 1/(1-H(11+40))*(J(11+20))/(1-H(11+60))*(J(11+40)

)/(1-H(11+80))*(J(11+60))

1X2

X3 = C1 / G2 / J(11+80) / D(11+120) IF D(11+100)=0

X3=SQRT.(G1/G4/D(11+100)/D(11+120)/D(11+140))/G4/N

J(11+80) IF D(11+100) > 0

TX3

H(11+120) = 1/H(11+60) - 1

H(11+140) = 1/H(11+80) - 1

H(11+100) = 1/H(11+40) - 1

X4=J(11+20)*(11+40)*G4*D(11+220)/H(11+100)/H(11+120)

X5=J(11+40)*(11+60)*G4*D(11+240)/H(11+120)/H(11+140)

X5 = X5 + X4 + J(11+20)*J(11+60)*G4*D(11+260) /N

H(11+100) / H(11+140)

6,12,1,1,3,

X5 = X5 + J(11+12*20)*(J(11+12*20)+1)*G4*(D(11+140+1N

2*20)-D(11+260+12*20)/3) /H(11+80+12*20)*2

TX5

X12= 0

7,12,1,1,3,

GO TO 8 IF D(11+100) > 0

X(12+5)=D(11+380+12*20)/D(11+120)

X(12+5)*X(12+5) + X(12+5) * 2

GO TO 7

8 X6 = D(11+280+12*60)/D(11+80+12*20)

X7 = D(11+300+12*60)/D(11+80+12*20)

X8 = D(11+320+12*60)/D(11+80+12*20)

X(12+8)=.5*(X6+X7+X8)+.25*(X6*2+X7*2+X8*2)+N

.125*(X6+X7+X8)*2

7 X12= X12 + J(11+12*20)*X(12+8)/H(11+80+12*20)

TX12

D(11+520)/2*D(11+540)/G2/D(11+120)*2 IF D(11+520)=0

X13 = EXP.(C1*D(11+520)+X12+X5)

X14 = X13 * X2 * X3

X17 = EXP.(-G4 * D(11+20))

TX17

X15 = H(11+20) * J11 * X17 / X14

TD(11+40) TD(11+60)

ATS INSTENSITY,STWATT/CM3/STRTS
TX24
ATSMOLESTSFRACTSIONS
TC11
2 TX3 TX3...X5 TX7 IX9 TX11 TX13 TX15 TX17 TX18
TX23 TX19
GO TO 1
HALT
PROGRAM END

00100119

APPENDIX C

PAST AND CURRENT RADIATION SIMULATION PROGRAMS AT ASTROSYSTEMS

| <u>Contract No.</u> | <u>Description</u> | <u>Customer</u> |
|-------------------------|---|---|
| AF08(635)-4303 | Laboratory Analysis of Simulated Rocket Booster Plumes | Air Proving Ground Eglin AFB |
| NOmr 3561(00) | Ultraviolet Properties at High Altitudes of an Oxygen - RP Rocket Exhaust Plume | Advanced Research Project Agency - Office of Naval Research |
| AF04(695)-33 | High Altitude Plume Simulation (Infrared Study) | Air Force Space Systems Division |
| AF33(657)-8680 | Investigation of UV Spectral Characteristics of Rocket Exhaust Under Simulated Space Conditions | Air Force Aero- nautical Systems Div. - Wright- Patterson AFB |
| N123-(60530)- 26857A | Infrared Characteristics of Chlorine Trifluoride/Hydrocarbon Rocket Flames at Simulated Altitude | U.S. Naval Ordnance Test Station - China Lake, California |
| AF33(615)-1197 | Analytical Investigation of an Electromagnetic Technique for the Independent Measurement of Chemical Rocket Exhaust Velocity Vector | Air Force Aero- nautical Systems Division - Wright Patterson AFB |
| AF04(611)-8157 | Design, Develop, Fabricate, Test and Deliver a Prototype Rocket Engine Exhaust Gas Measurement Device | Rocket Propulsion Group - Air Force Flight Test Center Edwards AFB |
| AF03(635)-3442 | Feasibility of Liquid Fuels as Signature Sources | Air Force Air Proving Ground Center - Eglin AFB |
| AF04(635)-3632 | Evaluate Emission Spectra and Selected Fuel Oxidizer Combinations | Subcontract under Denver Research Institute Prime from Air Proving Ground Center - Eglin AFB |

PRIMARY DISTRIBUTION LIST

AFFDL-TR-64-163

A. ACTIVITIES AT W-PAFB, OHIO

- 1 SEFI
- 7 AFFDL (FDCL) Attn: D. Shumway
- 1 AFFDL (FDP) Attn: STINFO
- 1 AFFD: (FDE) Attn: Library
- 1 SEPIR
- 1 SEPIE
- 1 EWABE Attn: Library

B. OTHER

- 3 Astrosystems International, Inc.
1275 Bloomfield Avenue
Fairfield, New Jersey 07007
- 13 Office of Technical Services
U. S. Department of Commerce
Washington 25, D. C.
- 20 Defense Documentation Center
Cameron Station
Alexandria, Virginia 22314
- 1 Rocketdyne Division
North American Aviation, Inc.
Attn: A. G. DeBell, Physics Research
6633 Canoga Avenue
Canoga Park, California

